FYS-3921
Master's Thesis in Electrical Engineering

Improved Hardware Stability and Signal Amplification in a Medical Microwave Radiometer

Alexander Tobiassen

October 27, 2010

Faculty of Science and Technology,
Department of Physics and Technology,
University of Tromsø
N-9037 Norway, Tromsø

FYS-3921

Master's Thesis in Electrical Engineering

Improved Hardware Stability and Signal Amplification in a Medical Microwave Radiometer

Alexander Tobiassen

October 27, 2010

Abstract

Breast cancer is one of the most frequent types of cancer in the female population today. Modern diagnostic modalities, while proven to be helpful within large scale screening programs, are inherently limited with regards to specificity and sensitivity, and use active methods for acquisition of information. A passive and non-invasive method for detection and diagnostic purposes could therefore be a valuable asset to the existing technology.

One such method is microwave radiometry. A microwave radiometer is an instrument for non-invasive thermography of subcutaneous temperatures. Recent advances within the field has demonstrated that this technology could be helpful in conjunction with existing methods.

This thesis presents the design, implementation and experimental verification of a miniaturized medical microwave radiometer. The design is based on the Switch-Circulator Dicke-configuration to minimize effects of gain variations and mismatch at the antenna input.

The performance of the radiometric system is verified through phantom experiments with a hot object embedded at various depths in a homogeneous, lossy medium. Results display a good coherence with regards to linearity, temperature sensitivity and repeatability. For an integration time constant of 2s, the accuracy ΔT is found to be $< 0.07^oC$, which is comparable with corresponding instruments as reported in literature.

Preface

First and foremost, I would like to thank my supervisor during this project, Professor Svein Jacobsen. You have been very supportive and a source of motivation when at times the task has seemed unsurmountable. Not least, I have benefited greatly from your expertise within the field and been encouraged by your enthusiasm. I would also like express my gratitude towards Engineer Karl Magnus Fossan for his invaluable contributions towards the realization of a functioning system. You have truly been one of the most supportive and helpful persons through this project.

Thanks also goes to Amund Kronen Johansen and research-fellow Øystein Klemetsen for their contribution with experience and ideas related both to the realization and experimental verification of the system, and to Sveinung Olsen for help with experience and equipment during PCB assembly.

Alexander Tobiassen,
Tromsø, October 2010

Contents

Chapter 1

Introduction

1.1 Breast Cancer

Breast cancer is the most common type of cancer in the female population today. Worldwide it represents 16% of all diagnosed cancers [26] and is thus one of the leading causes of death. In Norway, breast cancer is the most frequent cancer in women between 29 to 69 years. It is also the leading cause of reduced life time expectancy [49]. According to the latest report form the Norwegian Cancer Registry, 2753 new cases were diagnosed in 2008 and one in twelve women will develop some form of the disease within the age of 75 [49].

Stage	Survival Rate (%)
0	100
I	100
II	86
III	57
IV	20

Table 1.1: 5-year relative survival rate [7].

The standard treatment today ensures that most women who are diagnosed with breast cancer have a good chance of recovering to full health. However, the main indicator of survival chances is the pathological stage of the tumor at the time of treatment. This is represented by the 5-year relative survival[1]

[1]Percentage of patients alive after 5 years, adjusted for death by non-related causes

statistics as seen in table 1.1 (Figures from US NCI[2]). The stage of breast cancer depends on a combination of several tumor characteristics such as size, amount of invasiveness in surrounding tissue, spread to lymph nodes or distant parts of the body (metastasis). Table 1.2 presents a condensed description of each stage as defined by the UICC[3] TNM classification [7].

Stage	Tumor Characteristics
0	DCIS[4], the earliest form of breast cancer, cancer cells are found within a milk duct and have not invaded surrounding tissue.
I	Tumor less than 20 mm with no spread, or not found, with possibility of micro-metastases (less than 2 mm) to 1-3 axillary lymph nodes.
II	Tumor size 10-20 mm with spread to one of: axillary lymph nodes, arm pit lymph nodes, internal mammary lymph nodes. Tumor size between 20-50 mm, no spread or minimal spread to axillary- and/or internal mammary lymph nodes.
III	Tumor is around 50 mm, has spread to 1 to 9 lymph nodes (axillary and/or mammary). Also categorized by any sized tumor found or not found which has significant spread to a specific lymph node type, or alternatively a lesser spread to several types of lymph nodes.
IV	The cancer can be of any size and has spread to distant organs or lymph nodes.

Table 1.2: Tumor stage definition

Early research by Gullino [23] indicated that the likelihood of metastasis and tumor invasiveness increase over time, as the tumor grows and number of cells increase exponentially. This clearly indicates that early detection is a key factor to lower fatalities related to breast cancer. His research is further substantiated by statistics as seen in table 1.1. Early detection is also advantageous as it increases the possibilities and effectiveness of cancer treatment and breast-preserving measures [45].

[2]U.S National Cancer Institute [43]
[3]International Union Against Cancer

1.2 Breast Cancer Control: Detection Principles and Limitations

Early detection is currently assumed to be the most effective way to reduce mortality caused by breast cancer [45]. Because of this, mass screening of the female population, in which the disease is most frequent, is now commonplace. Screening for breast cancer refers to periodic examination of a large, asymptomatic, population. The age at which to begin such screening varies between countries, however it seems that most benefit is received for women aged between 50 to 69 years; which is the standard in Norway [47, 49] and which current research seems to agree is the age group where screening is most effective [47, 45].

The primary methods used in screening today are *Breast Self Examination* (BSE), *Clinical Breast Examination* (CBE) and *Mammography* - an X-ray imaging method [51].

BSE and CBE are simple ways for women to have their breasts examined, and are based on a technique for palpation of the breast. Regular palpation may allow women to get familiar with their breasts to early discover any abnormalities such as dense lumps. CBE is carried out by a clinician who is trained to inspect breasts both visually and by palpation. Any abnormal findings through these methods require further examination by diagnostic imaging. The use of both BSE and CBE as screening methods have however been called into question for the efficiency after a recent reevaluation [47], citing the inherently low ability to differentiate between benign lumps and possible tumors as a reason for its apparent limitation. Thus, imaging of the breast is currently the best method to discover tumors that are not felt by palpation.

Of the current imaging systems, mammography is the primary technique for screening and diagnosis of breast cancer. Images, so called mammograms, are produced using low-dose ionizing radiation of a compressed breast and presented as gray-scale maps of tissue density. Contrast is based on the relative difference in radiation absorption of tissues [48]. A trained radiologist investigates the mammogram for abnormal tissue characteristics that may indicate cancer. This involves the presence of micro-calcifications[5] and areas of increased density. The size of tumors that mammography is able to detect

[5]Small clusters of mineral deposits, often and indication of cancerous tissue. Minerals such as calcium have high contrast (absorbs more radiation) relative to the soft tissue in the breast and thus are often cause of suspicion.

varies around a median value of approximately 13.5 mm in diameter [51]. Other imaging techniques exist for imaging the breast, such as Ultrasound, MRI and PET. They are however invariably limited as screening methods and function mostly as complementary tools for diagnosis in cases where mammography itself is inconclusive [51].

Ultrasound Imaging creates images by measuring the reflection of sound waves that are passed into the breast through a transducer. The strength of this method lies in its ability to differentiate between cysts[6] and solid masses, which are often difficult to distinguish in X-ray images. As it allows real-time imaging, it is also used to guide needles during biopsy. Limitations such as low spatial resolution, time-consuming and operator dependent scans, as well as a poor ability to detect micro-calcifications, currently render ultrasound imaging ineffective as a primary screening tool [51, 47].

Microwave Resonance Imaging (MRI) produces detailed images using strong magnetic fields and measuring RF emission from nuclear spin [51]. Although it has many possibilities for imaging in great detail, it has not yet been found to be more effective than conventional mammography [47]. It provides similar false positive results, is unable to detect micro-calcifications and is a much more expensive imaging method. It could be beneficial however for imaging breasts with implants and for imaging of women at high risk that should begin screening earlier than recommended with mammography [47, 52].

Positron Emission Tomography (PET) measures positron emissions after injection of a radio-pharmaceutical, usually a form of glucose molecule traced with a positron emitting isotope, to create 3-D images of functional processes in the body. Some possible areas of application include staging of tumors and detection of metastasis, as cancerous tissue is characterized by increased glycolysis[7], which will cause a local concentration of positron emission in its vicinity [5].

The most conclusive test for breast cancer is biopsy. Its diagnostic sensitivity varies between 91 – 100% (96.6% average) [51]. This is an invasive procedure where a part of, or all of, the suspicious tissue is removed from the breast. The tissue sample is then studied by microscope to determine a diagnosis - mainly identifying if it is benign or malign. Biopsy is also used in staging of malignant tumors, and is usually performed in the event that diagnostics through mammography and adjunct methods are inconclusive.

[6] Usually benign, fluid filled pockets.

[7] Increased metabolism involving glucose conversion for energy production.

1.2.1 Limitations

As previously stated, mammography is the only imaging method which has a defined role as a primary screening modality. Other imaging methods such as Ultrasound, MRI and PET are not considered effective as such [47], but are primarily used as adjunct tools in diagnostics for more specific tissue characterization [51] or in more specific cases where they may be advantageous.

However, despite being considered the gold standard of modern breast cancer control, mammography has well known limitations both in detection and diagnostics. Perhaps most significant is the low sensitivity, especially when imaging dense breasts [28]. Dense breasts contain a high glandular-to-fat tissue ratio, which is common predominantly in young, pre-menopausal, women ($\leq$ 50 years). Cancers that are small of size ($\leq$ 10 mm) and lack presence of micro-calcification or are positioned near the circumference of the breast are also difficult to detect with mammography [28]. It is estimated that mammography misses as much as 15% of all cancers [45], so called false negative results. In the event of a false-negative result, a woman may go as long as two years until her next screening (with biennial screening[8]) is scheduled, in which the tumor has time to grow and spread.

Another limitation is a relatively low specificity, which is due to several reasons [17, 45]. This causes a high rate of false positive results [17] that necessarily leads to additional examination and usually biopsy to determine if the tissue is benign or malign. Highlighting the consequence of false positive results, and limitation of mammography as a diagnostic tool, is the fact that approximately 80% of all biopsy tests are diagnosed as benign [24]. This is a cause for concern with regards both to the woman in question – who may suffer phsycologicaly and receive uneeded treatment with potential complications [45] – and with regards to significantly increased costs related to "unnecessary" examination and surgical operations [51]. In addition, excessive exposure to ionizing radiation may in some (special) cases cause cancer to evolve [25].

The advent of digital mammography was long thought to increase the performance of mammography in screening. Digital detectors, as opposed to conventional analogue film-screen, allows images to be directly available on computer. Advanced CAD[9] software can then be applied to help radiologists improve detection of abnormal tissue characteristics [42]. Today digital mammography is relatively common [45], however, recent assessment concludes

[8] Standard in Norway[49]

[9] Computer Aided Diagnostics

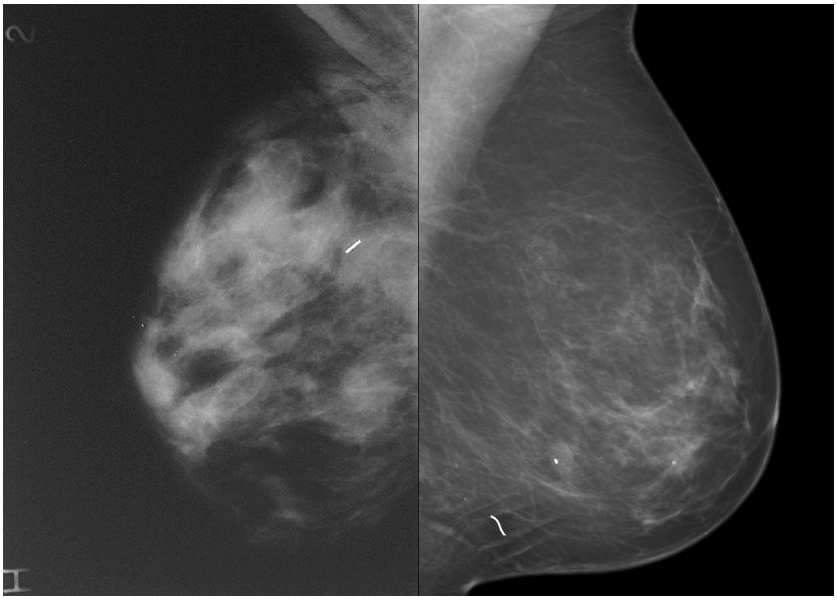

(a) Dense Tissue (b) Fatty Tissue

Figure 1.1: X-ray Mammograms comparing fatty and dense breasts. A) dense breast, causing decrease of mammography sensitivity. B) primarily fatty breast, where mammography sensitivity is high. *Courtesy of Radiumhospitalet Oslo, Norway.*

that currently it does not contribute significant difference in performance as compared to conventional mammography [47]. As a conclusion, the limitations of supporting modalities for mammography, as well as limitations in mammography itself, is an incentive to continue the research and development of alternative methods for supplementary diagnostics or as a primary screening tool. A general wish is to develop a system that offers good sensitivity to malignancies, is cost-effective and comfortable to the patient (i.e no compression of the breast) and produces no harmful radiation. One such system could be a microwave radiometer which is a passive method for non-invasive thermometry.

1.3 Microwave Radiometry and its Clinical Applications

Microwave radiometry is a remote sensing technique for resolving thermal energy in matter by measuring electromagnetic radiation in the microwave spectrum. The physical principle is described by Planck's law of black body radiation. It states that all matter above absolute zero emit an amount of electromagnetic radiation proportional to its temperature and emissivity. Originally, microwave radiometers have been used for a variety of applications within radioastronomy and earth observation by satellite. More modern uses include through-wall sensing [56], detection of fires [33] and temperature control in food industry [57, 14] as well as other industrial processes.

In clinical medicine, a microwave radiometer is used for non-invasive, passive thermometry. The method – also referred to as *microwave thermography* – is based on resolving tissue temperature by measuring the natural black body radiation emitted from the tissue volume under examination. Information about tissue temperature has possible applications within detection and diagnosis of pathological conditions in which temperature differentials are present, as well as temperature measurement and control in therapeutic processes and treatment [36]. Examples of such applications in literature includes monitoring of deep brain temperatures in infants during mild hypothermia [40], temperature control during hyperthermia treatments [13, 22] and assessment of disease activity in inflammatory joints of rheumatic patients [37].

Since the mid 1970's, the use of microwave radiometry for early detection of breast cancer has been investigated [18]. As a method of thermography, it relies on a visible contrast in temperature between cancerous and normal tissue. Clinical research and experiments have shown that increased metabolism occurs in cancerous tissue due to rapid and uncontrolled cell proliferation. This causes a significant (detectable) increase in heat production [27]. It has further been shown that the amount of metabolic heat production is exponentially related to the doubling time of tumor volume (see figure 1.2) [8], meaning that the more aggressive a tumor is, the more heat it will produce. A tumor is also likely to maintain a higher temperature than surrounding tissue as cancerous cells lack a normal capability of thermoregulation, as well as an increased activity of local angiogenesis[10] [9].

One of the reasons microwave thermography is seen to have such a potential

[10]Production of new blood vessels

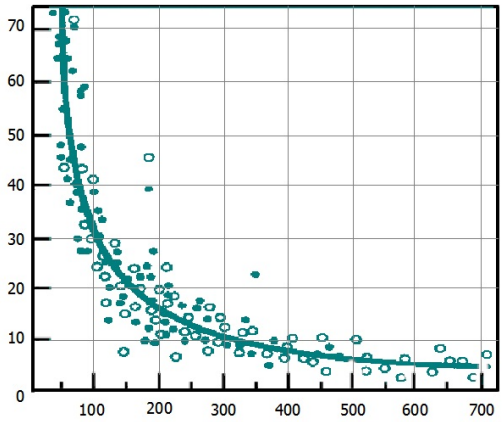

Figure 1.2: Growth rate and specific heat production of breast carcinomas. Y-axis is metabolic heat prodution of cancer tissue (10^3 W/cm^3). X-axis is the doubling time of respective tumor volume in days. Hollow circles are tumors with lymph node metastasis, solid circles are tumors with lymph node metastasis. [58, 8]

for detection of breast cancer is its ability to measure temperatures directly from subcutaneous tissue. This is possible because at microwave frequencies, radiation is less attenuated by tissue of low water content (fat,bone), allowing measurements to be taken from depths of up to several centimeters [35]. In contrast to infrared thermography which is limited to measure skin surface temperatures [35], there is a linear relationship between the temperature and radiation that is measured from subcutaneous tissue [3] whereas the temperature of the skin is a more complex (non-linear) relationship between several heat transfer functions governing the thermal regulations of the human body [35]. The simpler relationship results in more readily attainable measurements. It has also been shown that a microwave radiometer is not as dependent on environmental factors, with regards to temperature and humidity, as infrared thermography for which a controlled clinical environment is needed [35]. On the other hand, a common issue in radiometry is electromagnetic interference from external sources.

The areas which the method is seen to be most advantageous is especially in detecting cancer in breasts of younger women, where mammography has limited detection capabilities [36]. Another potential is application in diagnosis to differentiate between malign and benign tumors because of the different heat production [4]. Recent experiments have confirmed this potential [10], which could greatly decrease the number of biopsies that in retrospect were unnecessary, if used in conjunction with mammography. Another potential

is to indicate increased risk of cancer as physiological signs, such as increased heat production, precedes anatomical changes detectable by X-ray. The results in Figure 1.2 also indicates a bias towards detecting more aggressive tumors [8].

Other promising results have been reported where a microwave radiometer in conjunction with temperature measurements of the skin (IR[11]) has been used for screening. Results have been compared with mammography and ultrasound which show that the method has comparable performance in some instances. Sensitivity in this case varies from 85.1% to 94.2%, while specificity is in the range of 76%–81.8% [58].

1.3.1 Challenges

Despite its clear potentials as a non-invasive and harmless method for detection of breast cancer, there are some challenges when designing a microwave thermographic system with adequate characteristics. One of the major difficulties is the fact that we are measuring a very weak signal at a relatively long wavelength. The strength of the signal is as low as -174 dBm/Hz at human tissue temperatures which poses a challenge with regards to detection [29]; especially with regards to achieve a temperature sensitivity which is adequate for resolving temperature differentials small enough to be clinically useful. It is generally stated that a sensitivity of 0.1K or lower should be reached [36]. Spatial resolution is dependent on wavelength, and thus microwave radiometers is limited to a spatial resolution of about 1 cm [3]. Comparably, a spatial resolution of 1 mm is typical for infrared thermography [3], but with a penetration depth of less than a millimeter.

Another problem relates to the nature of the measured signal. In contrast to receivers in communications or other imaging devices, a microwave radiometer measures natural electromagnetic radiation which is incoherent (noise-like) [29]. This means that it has no statistical properties that can be used to increase the quality of a signal through more advanced signal processing techniques. With incoherent signals, the most apparent method of signal condition is low pass filtering, which is achieved by integration. Another option is to increase system bandwidth to reduce the need of gain in the system. Thus, there are no means of obtaining a higher signal-to-noise ratio other than making sure the equipment used is of adequate quality.

[11] Infrared

Another challenge related to the signal measurement is that as it is incoherent, it is indistinguishable from radiation of competing sources. Such sources are for example cell phones, satellite communication or wireless networks, which all operate in the microwave frequency range. Thus an important part of the design is to make sure the equipment is as possible as resilient to interference from such sources. Another solution would be to place the operating frequency of the system in bands which are less crowded. This effectively limits the choice to where the system could be operated, but must be considered as such interference could possibly decrease the reliability of measurements.

1.4 Project Motivation and Goals

The motivation for this project is to further the development of a miniaturized microwave radiometer primarily intended for detection of breast cancer. The object for this study is first and foremost to provide a solution to an issue of instability in the hardware of a previously designed front-end. Complementary hardware is also developed to implement a Dicke-configuration such that errors due to drift are minimized. The final goal is to experimentally verify the performance of the radiometric system as an instrument for detection of subcutaneous temperatures. In summary, the thesis involves the following: *i)* To learn and understand the principles of radiometry in both theory and practice. *ii)* Investigate theory about stability in amplifiers and practical solutions to stability problems. *iii)* PCB design. *iv)* Implementation of an actual system. *v)* Experimental verification of a real system by the use of measurement equipment. *vi)* To carry out radiometric measurements on a model based on a hot object embedded in a lossy medium.

1.5 Paper Structure

The following paper is structured as follows. Chapter 2 reviews relevant microwave theory, this includes design of microwave amplifiers and considerations for stability as well as theory of noise measurement. Chapter 3 introduces fundamental theory related to microwave radiometry, as well as presenting relevant radiometer designs. Chapter 4 presents the design and implementation of the radiometric system developed through this study. Chapter 5 presents simulations and numerical estimates which are used as

guidelines for the design. Chapter 6 introduces the various experimental setups and approaches for characterization of the system. Chapter 7 presents the results obtained, and finally chapter 8 contains a discussion of the various results, their implications and ideas for future work to further develop the radiometric system.

Chapter 2

Microwave Theory

This chapter represents general microwave theory, theory of noise and of amplifier stability.

2.1 Basic Theory

2.1.1 Transmission Lines

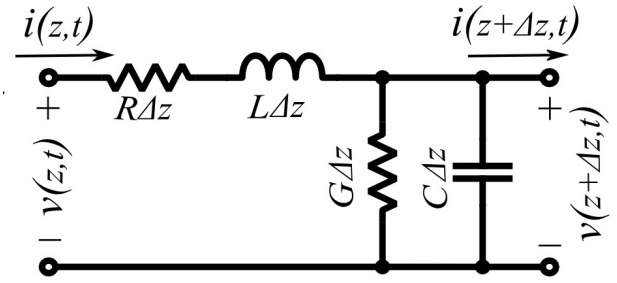

Figure 2.1: Lumped-element equivalent circuit for a transmission line of incremental length Δz.

Transmission line is a general term used for the medium in which electrical signals or electric power is transfered in a circuit. In regular circuit theory the physical size of circuit networks are usually insignificant compared to the electrical wavelength of signals. The picture changes for RF frequencies. The transmission line and devices may appear to be of significant electrical length

such that the magnitude and phase of incident voltage and current vary with position along the line. This calls for extended theory to explain behavior of propagating waves at high frequencies. For high enough frequencies the transmission line is seen to have both capacitive and inductive characteristics as well as presenting a certain ohmic resistance. Thus, at microwave frequencies, a transmission line is defined as a distributed parameter network and modeled as a lumped-element circuit, this is schematically presented in figure 2.1, with the following definitions [46]:

- R – Series resistance per unit length (Ω/m).
- L – Series inductance per unite length (H/m).
- G – Shunt conductance per unit length (S/m).
- C – Shunt capacitance per unit length (F/m).

Thus, any line of a specific length can be seen as a cascade of such incremental equivalent circuits. Kirchoff's law is applied to derive what is known as the *Telegraphers Equations*, from which the following expressions of the complex voltage and current is found as [46]

$$V(z) = V_0^+ e^{-\gamma z} + V_0^- e^{\gamma z}, \tag{2.1}$$
$$I(z) = I_0^+ e^{-\gamma z} + I_0^- e^{\gamma z}. \tag{2.2}$$

Here, $\gamma = \sqrt{(R + jL\omega)(G + jC\omega)} = \alpha + j\beta$ is the complex propagation constant which accounts for attenuation (α) and frequency dependency (β). The ratio of voltage to current is dependent on the (complex) characteristic impedance Z_0 of the line as follows [46];

$$I(z) = \frac{V_0^+}{Z_0} e^{-\gamma z} + \frac{V_0^-}{Z_0} e^{\gamma z} \tag{2.3}$$

Equation 2.2 displays how the total voltage and current is a composite of two waves traveling in opposite direction (V_0^+ and V_0^-). This is an important concept in transmission line theory called wave reflection. To explain this property it is convenient to use the notion of a lossless transmission line,

which for short distances is often a good approximation. In this case, the α term is 0 and characteristic impedance, Z_0, is reduced to a real value. Considering such a transmission line where a source at position z < 0 generates an incident wave $V_o^+ e^{-j\beta z}$ and terminates in an arbitrary load Z_L. As the wave propagates along the line, the current-voltage ratio is dependent on Z_0, but at the load (z $= 0$) the ratio changes. Thus, a reflected wave is produced to balance the equation. The amount of reflection depends on the difference between Z_L and Z_0, and is defined by the *voltage reflection coefficient*, Γ [46],

$$\Gamma = \frac{V_o^-}{V_0^+} = \frac{Z_L - Z_0}{Z_L + Z_0} \in [-1, 1]. \tag{2.4}$$

Reflection of power and loss of transmitted power due to mismatch between devices or transmission lines is usually inevitable in most circuits. Thus, Γ is a frequently used parameter and is used to define the following quantities. *Return loss*, *VSWR*[1] and *Insertion loss*.

Return Loss is defined as the amount of power reflected due to mismatch between the transmission line and a load, and is usually expressed as

$$RL = -20log\,|\Gamma| \quad \text{dB}. \tag{2.5}$$

A matched load such that $\Gamma = 0$ would result in -∞ loss, meaning that the larger the absolute value the better the match is. VSWR is defined as the ratio of maximum voltage to minimum voltage of the standing wave resulting from a reflection and is expressed as

$$VSWR = \frac{V_{max}}{V_{min}} = \frac{1 + |\Gamma|}{1 - |\Gamma|}. \tag{2.6}$$

The minimum value of VSWR is 1, indicating that $V_{max} = V_{min}$, such that large values indicate a larger mismatch. Insertion loss is the transmission coefficient (T $= 1 + \Gamma$) expressed in dB. It is a measure of how much power is reduced during transmission from one transmission line or network to another and is expressed as;

$$IL = -20\log\,|T| \quad \text{dB}, \tag{2.7}$$

[1]Voltage Standing Wave Ratio

2.1.2 Microstrip

Microstrip is one of the most common types of transmission lines, especially in microwave circuits. It consists of a thin, plane conductor of copper on the top side of a dielectric substrate with a continuous ground plane on the bottom side. Designing transmission lines with the correct characteristic impedance is an important part of microwave circuit design as mismatch at transmission line/component interfaces will cause reflection and consequently loss of critical power. In this sense a microstrip presents some difficulties as the electrical field lines are divided by a discontinuous dielectric (air and ϵ_r). The combination results in an inhomogeneous dielectric where phase velocity is not constant, hence pure TEM-waves are not supported. Instead we get a situation of a hybrid TM-TE wave which is complicated to analyze. Luckily, under certain conditions an approximate model (presented by Pozar) can be applied [46].

For the following numerical approximation, it is assumed the electric thickness 'd' of the dielectric substrate is negligible compared to wavelength. Phase velocity v_p and propagation constant β can then be found by defining an effective dielectric constant ϵ_e as the homogeneous equivalent to the combined effect of air and dielectric substrate.

$$v_p = \frac{c}{\sqrt{\epsilon_e}} \tag{2.8}$$

$$\beta = k_0\sqrt{\epsilon_e} \tag{2.9}$$

$$\epsilon_e = \frac{\epsilon_r + 1}{2} + \frac{\epsilon_r - 1}{2}\left(\frac{1}{\sqrt{1 + 12d/W}}\right). \tag{2.10}$$

If the dimensions of the line are known, the characteristic impedance can be estimated using one of the following equations [46],

$$Z_0 = \begin{cases} \frac{60}{\sqrt{\epsilon_r}} \ln\left(\frac{8d}{W} + \frac{W}{4d}\right) & \text{for } W/d \leq 1, \\ \frac{120\pi}{\sqrt{\epsilon_r}[W/d + 1.393 + 0.667\ln(W/d + 1.444)]} & \text{for } W/d \geq 1, \end{cases} \tag{2.11}$$

where W denotes the with of the line. If designing for a specific impedance, substrate thickness d is usually known and thus it is often the width that must be adjusted accordingly to obtain a certain characteristic impedance. This

is done by computing the ratio W/d through one of the following equations [46];

$$\frac{W}{d} = \begin{cases} \frac{8e^A}{e^{2A}-2} & \text{for } W/d < 2. \\ \frac{2}{\pi}\left[B - 1 - \ln(2B-1) + \frac{\epsilon_r - 1}{2\epsilon_r}\left(\ln(B-1) + 0.39 - \frac{0.61}{\epsilon_r}\right)\right] & \text{for } W/d > 2. \end{cases} \tag{2.12}$$

where A and B are expressed as,

$$\begin{aligned} A &= \frac{Z_0}{60}\sqrt{\frac{\epsilon_r + 1}{2} + \frac{\epsilon_r - 1}{\epsilon_r + 1}\left(0.23 + \frac{0.11}{\epsilon_r}\right)}, \\ B &= \frac{377\pi}{2Z_0\sqrt{\epsilon_r}}. \end{aligned} \tag{2.13}$$

2.1.3 S-parameters

S-parameters, or scattering parameters, are extensively used in microwave design. Relating the incident to the reflected voltage waves at each port, they give a complete description of any N-port network as seen at its N ports. Key areas of use is to describe component performance, matching and as parameters in design of amplifiers. S-parameters are usually displayed in the form of a N×N matrix referred to as the *scattering matrix*, [S], where N is the number of ports of the device (or network). [46],

Figure 2.2 displays a general representation of a two-port network, which can be characterized at any frequency by the matrix

$$S = \begin{bmatrix} S_{11} & S_{12} \\ S_{21} & S_{22} \end{bmatrix}$$

The values of each specific element (each parameter) of the matrix can be determined from the formula,

$$S_{ij} = \frac{V_i^-}{V_j^+}, \text{ where } V_K^+ = 0 \text{ for } k \neq j. \tag{2.14}$$

Equation (2.14) can be understood as the following; drive port j with an incident voltage (V_j^+) while all other ports are terminated with matched loads.

S_{ij} is then the ratio of the reflected voltage at port i to the incident voltage from port j under these conditions. The definition of each S parameter in a two-port network will then be [46]:

- $S_{11} = \frac{V_1^-}{V_1^+}_{V_2^+=0}$ = Input reflection coefficient.
- $S_{21} = \frac{V_2^-}{V_1^+}_{V_2^+=0}$ = Forward transmission coefficient (gain).
- $S_{12} = \frac{V_1^-}{V_2^+}_{V_1^+=0}$ = Reverse transmission coefficient
- $S_{22} = \frac{V_2^-}{V_2^+}_{V_1^+=0}$ = Output reflection coefficient.

It is worth noting that for components or networks with ports that are matched to the characteristic impedance of the system transmission line, S_{11} and S_{22} is equal to the voltage reflection coefficient as defined in equation (2.4) depending on which port is considered, while S_{21} equals the transmission coefficient, T. Hence, *return loss* and *insertion loss* can be calculated from the S-parameters.

2.2 Amplifier Design

One of the key components of a microwave radiometer is the front-end receiver, of which an important aspect is amplification of a weak signal. Some key parameters of amplifier design and stability theory is therefore presented.

2.2.1 Two-Port Networks and Power Gain

For an arbitrary two-port network (illustrated by figure 2.2) exited by a source with impedance Z_S and connected to a load Z_L, three types of gain can be defined [46]:

- Power Gain (G) = P_L/P_{in}, is the ratio of power dissipated in the load to the power delivered to the input of the network.

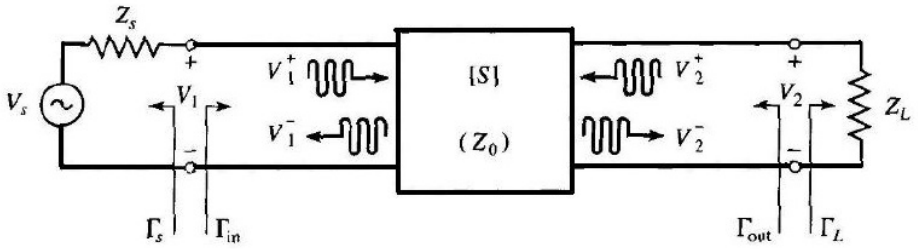

Figure 2.2: Arbitrary Two-Port Network [46].

- Available Gain (G_A) = P_{avn}/P_{avs}, is the ratio of power available from the network to the power available from the source.
- Transducer Power Gain (G_T) = P_L/P_{avs}, is the ratio of power delivered to the load to the power available from the source.

Expressions for the different gain definitions can be derived in terms of the S-parameters used to describe the two port network. The network source and load impedance are defined as [46],

$$\Gamma_L = \frac{Z_L - Z_0}{Z_L + Z_0}, \tag{2.15}$$

$$\Gamma_S = \frac{Z_S - Z_0}{Z_S + Z_0}. \tag{2.16}$$

Accounting for mismatch at the input and output, the reflection coefficients Γ_{in} and Γ_{out} are defined as [46],

$$\Gamma_{in} = \frac{V_1^-}{V_1^+} = S_{11} + \frac{S_{12}S_{21}\Gamma_L}{1 - S_{22}\Gamma_L} = \frac{Z_{in} - Z_0}{Z_{in} + Z_0}, \tag{2.17}$$

$$\Gamma_{out} = \frac{V_2^-}{V_2^+} = S_{22} + \frac{S_{12}S_{21}\Gamma_S}{1 - S_{11}\Gamma_S} = \frac{Z_{out} - Z_0}{Z_{out} + Z_0}. \tag{2.18}$$

Using the following expressions for voltage in terms of S-parameters

$$
\begin{aligned}
V_2^+ &= V_2^-\Gamma_L && (2.19)\\
V_1^- &= S_{11}V_1^+ + S_{12}V_2^+ = S_{11}V_1^+ + S_{12}V_2^-\Gamma_L && (2.20)\\
V_2^- &= S_{21}V_1^+ + S_{22}V_2^+ = S_{21}V_1^+ + S_{22}V_2^-\Gamma_L, && (2.21)
\end{aligned}
$$

V_1 (incident voltage) is found through voltage division:

$$V_1 = V_S\frac{Z_{in}}{Z_S + Z_{in}} = V_1^+(1+\Gamma_{in}). \tag{2.22}$$

The one voltage that is always known is source voltage (V_S). Thus, all expressions for power should be derived solving (2.18) for Z_{in}, (2.22) becomes

$$V_1^+ = \frac{V_S}{2}\frac{(1+\Gamma_S)}{(1-\Gamma_S\Gamma_{in})}. \tag{2.23}$$

Now, using (2.23) the average power delivered to the network can be defined as [46]

$$P_{in} = \frac{1}{2Z_0}\left|V_1^+\right|\left(1-|\Gamma_{in}|^2\right) = \frac{|V_S|^2}{8Z_0}\frac{|1-\Gamma_S|^2}{|1-\Gamma_S\Gamma_{in}|}(1-|\Gamma_{in}|^2). \tag{2.24}$$

Expressing V_2^- in terms of V_S through equations (2.21) and (2.23), we then find the power delivered to the load as [46]

$$P_L = \frac{|V_2^-|^2}{2Z_0}(1-|\Gamma_L|^2) = \frac{|V_S|^2}{8Z_0}\frac{|S_{21}|^2(1-|\Gamma_L|^2)|1-\Gamma_S|^2}{|1-S_{22}\Gamma_L|^2|1-\Gamma_S\Gamma_L|^2}. \tag{2.25}$$

The maximum power available to the network is the power delivered by the source, P_{avs}. P_{avs} is delivered without reflection when $\Gamma_{in} = \Gamma_S^*$ in which case we have [46]

$$P_{avs} = P_{in} = \frac{|V_S|^2}{8Z_0}\frac{|1-\Gamma_S|^2}{(1-|\Gamma_S|^2)}. \tag{2.26}$$

In the same way, the maximum power delivered to the source is P_{avn} when $\Gamma_L = \Gamma_{out}^*$, so

$$P_{avn} = P_L = \frac{|V_S|^2}{8Z_0} \frac{|S_{21}|^2 |1 - \Gamma_S|^2}{|1 - S_{11}\Gamma_S|^2 (1 - |\Gamma_{out}|^2)}. \tag{2.27}$$

Having derived expression for the different powers, the various gain can be expressed in terms of S-parameters and reflection coefficients [46].

Power Gain:

$$G = \frac{P_L}{P_{in}} = \frac{|S_{21}|^2 (1 - |\Gamma_L|^2)}{(1 - |\Gamma_{in}|^2) |1 - S_{22}\Gamma_L|^2}. \tag{2.28}$$

Available Gain:

$$G_A = \frac{P_{avn}}{P_{avs}} = \frac{|S_{21}|^2 (1 - |\Gamma_S|^2)}{|1 - S_{11}\Gamma_S|^2 (1 - |\Gamma_{out}|^2)}. \tag{2.29}$$

Transducer Gain:

$$G_T = \frac{P_L}{P_a vs} = \frac{|S_{21}|^2 (1 - |\Gamma_S|^2)(1 - |\Gamma_L|^2)}{|1 - \Gamma_S \Gamma_{in}|^2 |1 - S_{22}\Gamma_L|^2} \tag{2.30}$$

In the event that both source and load are conjugately matched to the two-port network, gain is maximized (no loss through reflection) so that the three expressions are equal. Two other special cases are worth noting. One is when input and output impedance is equal to the characteristic impedance of the two-port, no reflection occurs and transducer gain is reduced to [46],

$$G_T = |S_{21}|^2. \tag{2.31}$$

The other is a case of a unilateral amplifier, where $S_{12} \approx 0$. In this event $\Gamma_{in} = S_{11}$. Inserting this into (2.30) unilateral transducer gain is defined as,

$$G_{TU} = \frac{|S_{21}|^2 (1 - |\Gamma_S|^2 (1 - |\Gamma_L|^2))}{|1 - S_{11}\Gamma_S|^2 |1 - S_{22}\Gamma_L|^2}. \tag{2.32}$$

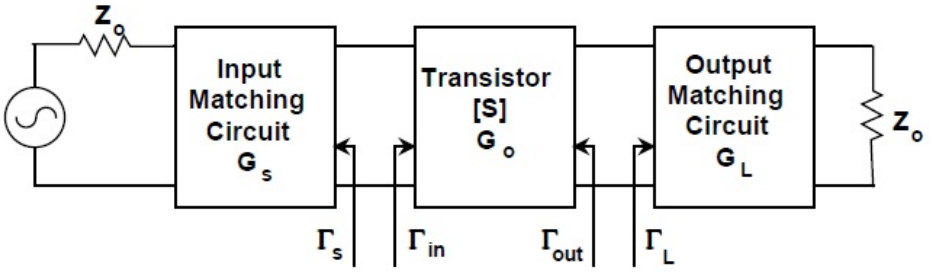

Figure 2.3: Transistor Matching Circuit [46].

2.2.2 Transistor Matching Network

Amplifiers consist of one or more active elements (transistors) to achieve amplification. An isolated transistor is usually not matched to 50Ω, thus an important aspect of amplifier design is to match this transistor to input and output impedances. Matching is also important with regards to stability. Figure 2.3 illustrates a model where a single stage amplifier has been split into three parts. An input matching network, the transistor itself, and an output matching network.

As transducer gain (2.30) accounts for mismatch to both source and load, it is the most convenient gain definition in this regard and is expressed as $G_T = G_S G_0 G_L$. Here, the gain of each respective two-port is defined as [46]:

$$G_S = \frac{1 - |\Gamma_S|^2}{|1 - \Gamma_{in}\Gamma_S|^2}, \tag{2.33}$$

$$G_0 = |S_{21}|^2, \tag{2.34}$$

$$G_L = \frac{1 - |\Gamma_L|^2}{|1 - S_{22}\Gamma_L|^2}. \tag{2.35}$$

If $S_{12} \approx 0$, we have a case of unilateral gain and $\Gamma_{in} = S_{11}$.

2.2.3 Stability

When designing an amplifier, evaluation of stability is critical. A stable amplifier is one which have a decaying time response to input for all frequencies. If it is not stable the response does not decay, instead it increases in strength

over time. This is called oscillation, or self-amplification and could in some cases destroy the amplifier. Stable amplification is also critical in receiver design such as the front-end of a radiometer. A radiometer is dependent on measuring average power in a given time frame. Thus, if oscillation occurs within the passband it will result in fluctuating peaks disturbing its flatness and consequently lead to erroneous results.

Stability is here discussed in light of the model presented in figure 2.3, meaning for amplifiers with one active transistor. Here, stability is dependent on the matching networks as represented by the values of Γ_{in} and Γ_{out}, which again depends on Γ_L and Γ_S. Two definition of stability is defined [46]:

- *Unconditional Stability*: If $|\Gamma_{in}| < 1$ and $|\Gamma_{out}| < 1$ for all passive source and load impedances ($|\Gamma_S|$ and $|\Gamma_L| < 1$), the network will be unconditionally stable.
- *Conditional Stability*: Also referred to as *Potentially Unstable*. The network will be conditionally stable if $|\Gamma_{in}| < 1$ and $|\Gamma_{out}| < 1$ for only a certain range of passive source and load impedances.

The input and output matching networks are in general dependent on frequency. Consequently, an amplifier that is stable at the design frequency may be unstable at other frequencies, thus it is important to evaluate an amplifiers stability for a large range of frequencies [46]. Applying the stated requirements for unconditional stability to the equations in (2.18) results in a set of conditions that must be satisfied for the amplifier to be unconditionally stable [46],

$$|\Gamma_{in}| = \left| S_{11} + \frac{S_1 2 S_2 1 \Gamma_L}{1 - S22\Gamma_L} \right| < 1, \tag{2.36}$$

$$|\Gamma_{out}| = \left| S_{22} + \frac{S_1 2 S_2 1 \Gamma_S}{1 - S11\Gamma_S} \right| < 1. \tag{2.37}$$

For the unilateral case when $S_{12} \approx 0$, (2.37) is simplified to

$$|S_{11}| < 1, \tag{2.38}$$

$$|S_{22}| < 1. \tag{2.39}$$

To determine if the amplifier can be approximated as unilateral, one can compute the error of making such an approximation by using the ratio G_T/G_{TU}, which is transducer gain and unilateral transducer gain, respectively. The ratio is defined within the limits [46],

$$\frac{1}{(1+U)^2} < \frac{G_T}{G_{TU}} < \frac{1}{(1-U)^2}, \tag{2.40}$$

where U is the unilateral figure of merit given as [46],

$$U = \frac{|S_{12}|\,|S_{21}|\,|S_{11}|\,|S_{22}|}{\left(1-|S_{11}|^2\right)\left(1-|S_{22}|^2\right)}. \tag{2.41}$$

If the error is on the order of a few tenths of a dB, a unilateral assumption can be used as it simplifies computations.

Stability Circles

If a device is potentially unstable, one can find the range of values of Γ_L and Γ_S for which stability can be achieved. This range can then be plotted as a circle called *stability circle* on a Smith chart. The stability circles define boundaries between stable and potentially unstable regions for the load and source impedance. Using stability circles, the matching networks can be designed and the values of Γ_{in} and Γ_{out} can be plotted on the Smith chart to verify if they are within the stable regions for all frequencies.

The stability circles can be defined by the following equations [46]:

$$C_L = \frac{(S_{22}-\Delta S_{11}^*)^*}{|S_{22}|^2-|\Delta|^2}, \tag{2.42}$$

$$R_L = \left|\frac{S_{12}S_{21}}{|S_{22}|^2-|\Delta|^2}\right|, \tag{2.43}$$

$$C_S = \frac{(S_{11}-\Delta S_{22}^*)^*}{|S_{11}|^2-|\Delta|^2}, \tag{2.44}$$

$$R_L = \left|\frac{S_{12}S_{21}}{|S_{11}|^2-|\Delta|^2}\right|, \tag{2.45}$$

where C_L, C_S represent the center of the output and input circle, respectively, and R_L,R_S represents the radius of the output and input circle, respectively. The asterisk stands for the complex conjugate.

The boundary of each circle will be where $|\Gamma_{in}| = 1$ and $|\Gamma_{out}| = 1$. For an unconditionally stable device the stability circles will not intersect the Smith chart, they will either be outside of it or totally enclose it. If the device is potentially unstable there will be some intersection, or the circle will lie entirely inside the Smith chart, and one must determine which area is the stable area where the absolute value input and output reflection coefficients will be less than unity [46].

Stability Tests

The last section described the use of stability circles and how they can be used to determine the regions of Γ_L and Γ_S where the amplifier circuit will be conditionally stable. Stability circles are often enlightening when designing amplifiers and matching special circuits. But there are simpler tests available to determine the stability of an amplifier if its parameters are known from measurement.

The first test is called the "K - Δ test" and guarantees unconditional stability if the following conditions are satisfied [46],

$$K = \frac{1 - |S_{11}|^2 - |S_{22}|^2 + |\Delta|^2}{2|S_{12}S_{21}|} \quad > 1, \tag{2.46}$$

where Δ is the S-matrix determinant,

$$\Delta = S_{11}S_{22} - S_{12}S_{21} \quad < 1. \tag{2.47}$$

K is called Rollet's condition, and the test is often referred to by the same name. It is also required that $|S_{11}|$ and $|S_{22}| < 1$ [46]. If either of the S-parameters has a magnitude larger than 1, the amplifier cannot be unconditionally stable.

A problem with Rollet's condition of stability is that since it involves constraints on two separate parameters, it cannot be used to compare the relative stability of two or more devices. In addition, it does not provide any direct physical insight to the degree of instability or stability of a two-port network [15]. With this in mind, a more recent criterion has been developed that

consists of only a single parameter to determine unconditional stability. The parameter, μ, is derived from a geometrical perspective involving the Smith chart and stability circles, and is defined as [15],

$$\mu = \frac{1 - |S_{11}|^2}{|S_{22} - \Delta S_{11}^*| + |S_{12}S_{21}|}. \tag{2.48}$$

The test guarantees unconditional stability of a linear two-port system if $\mu > 1$. The value of the μ parameter is more closely tied to the physical aspects of stability. It is defined as the minimum distance in the Γ_L plane between the origin of the Smith chart and the region of instability. This means that there is a direct relation between the value of μ and the degree of stability, a greater value implies greater stability [15]. If the amplifier is, or can be approximated as, unilateral, (2.48) is reduced to,

$$\mu_u = \frac{1 - |S_{11}|^2}{|S_{22}||1 - |S_{11}|^2|}, \tag{2.49}$$

from which it is clearly seen that unconditional stability ($\mu > 1$) can only be achieved if $|S_{11}| < 1$ and $|S_{22}| < 1$, which were earlier defined as necessary conditions for unconditional stability of a unilateral device or circuit. Another observation is that the degree of stability can be increased by improving input and output matching of the amplifier.

Cascading Amplifiers

Sometimes the gain of a single amplifier might not be adequate in systems where the signal level is extremely low. To increase the gain to the necessary level, it may be necessary to place several amplifiers in a cascade. For instance, take a clinical radiometer measuring temperatures in the human body where the effects of microwave radiation are approximately -174 dBm/Hz at room temperature. With an integration bandwidth of 500 MHz this amounts to -87 dB effect at the input and one would need at least a gain of 40-50 dB to achieve a reliable detection. The need for low noise figures leads to the use of LNAs with lower gain. If a typical LNA has around 15 to 20 dB gain, a solution could be to implement two or three LNAs to achieve the desired amplification [31].

The act of cascading two or more amplifiers increases the importance of stability, as well as creating new difficulties. Since each amplifier will be the

input load of the next, well matched (low decibel magnitude) input or output values (S_{11} and S_{22}) are necessary to avoid too much mismatch at either port between them. The error caused by reflection interaction between amplifiers is termed mismatch error [21], and may become large if the difference between S_{11} and S_{22} is high. There are no exactly specified values for which S_{11} and S_{22} will have a low mismatch error between them, but as a rule of thumb they are good if they are below -10 dB in the passband [21]. If the mismatch error exceeds $\pm$ 1 dB, one should be concerned about the stability of the cascade. Mismatch errors can be accounted for by decoupling the amplifiers with isolators if matching networks is out of the question[21].

In theory, cascading two or more unconditionally stable and identical devices will result in an overall unconditionally stable amplifier [54]. If the amplifiers are perfectly matched for all frequencies as well, the logarithmic gain of each stage can simply be added [21] and the resulting passband will be relatively flat. Perfect matching is of course seldom achieved in practice, but by using matching network techniques, such as direct impedance matching [21] or feedback inductor methods [59] in the transistor topology design, it is possible to make the output and input reflection values low enough to have a good matching, leading to cascadable amplifiers. However, even if the single-stage amplifier is unconditionally stable with good matching parameters, it is not given that a cascade will be stable. Problems can arise that are not directly related to the amplifiers design parameters, but to how they are placed in the circuit. These problems come from what is referred to as parasitic effects. Such effects include feedback through the electrical fields of the transistors, which may become large in miniaturized designs. Another effect is leakage or crosstalk through shared DC supply lines, this is a recurring phenomenon in microwave circuits.

Another factor to be aware of is the fact that the remainder of the system might have high reflections, this is true with for example reactive filters which could cause high reflections back to the amplifiers. If this happens, steps must be taken to take this into account. To verify that an amplifier is unconditionally stable one can use one of the two methods presented in the previous section.

2.3 Noise in Microwave Systems

The random nature of sub-atomic particles such as electrons and other charge carriers causes electrical components to produce an output power, even in the absence of any input. This output may be a result of several different random processes, and is collectively termed electrical *noise* as it is not part of the original signal.

The amount and nature of the noise present in a microwave or RF receiving system is important to characterize, as it will blend with the wanted signal. When this happens, the receiver system is unable to differentiate between the original signal and noise. It follows that noise will degrade the sensitivity of the receiver [46].

Noise can also be introduced from external sources and be picked up by the received signal or receiving antenna. In addition, for some transmission line geometries, such as microstrip, signals can be disturbed by interference from other systems working within the same bandwidth. Noise of this type is usually not included in the noise characterization of components or systems. Instead one rather tries to design the system to be as immune to such effects as possible [55].

In this section we will look at different types of noise as well as how to characterize and limit the intrinsic noise of a microwave receiver. The two most significant types of noise are thermal and shot noise, which are inherent in all electrical devices. There are, however, several other phenomena that display the same characteristics as thermal and shot noise. Usually, components are characterized by the combined effect of all such noise types and one refers to this effect as if it were caused only by a thermal noise source [55].

2.3.1 Noise Types

Thermal Noise

Thermal noise is also known as Johnson [32] or Nyquist [44] noise. It is the most fundamental source of noise in electrical circuits and occurs in both passive and active components. Its physical origin is the vibration of charged carriers within conductive materials at thermal equilibrium. In most cases, thermal noise sources are adequately described as independent Gaussian distributed random variables and thermal noise as white. Consequently, noise

power is additive and the noise produced by several sources is merely a sum of each individual power [46].

If we consider a resistor at a temperature T *(K)*, the charge carriers in the conductive resistor medium are in random motion and their kinetic energy is proportional to the material temperature T. This random motion of charge gives rise to current, and thus a random fluctuation of voltage at the resistor terminals. Since the voltage vary randomly in time, it is best described by its root mean square V_n. An expression for V_n can be derived from Planck's law of black body radiation and expressed as [46],

$$V_n = \sqrt{\frac{4hfBR}{e^{hf/kT} - 1}}, \tag{2.50}$$

where h is Planck's constant, k is Boltzmann's constant, T is absolute temperature in Kelvin, B is the system bandwidth, f is the center frequency and R is the resistance. This is a general result derived from quantum mechanics and is valid for all frequencies. For systems operating withing the microwave range of frequencies, the *Rayleigh-Jeans approximation* [46],

$$V_n = \sqrt{4kTBR}, \tag{2.51}$$

is more commonly used. Further, the maximum available noise power from the resistor is given by [46],

$$P = \left(\frac{V_n}{2R}\right)^2 R = kTB, \tag{2.52}$$

From (2.52) it is seen that the power delivered by the noisy resistor is independent of frequency. In addition there are two important characteristics for microwave systems to be observed. One is that available noise power is proportional to bandwidth, meaning that decreasing the bandwidth will result in less noise power. The other is that cooler components produce less noise [46].

Since thermal noise sources are described with such ease, it is common to extend the same theory to other types of noise that display the same characteristics. This is done by modeling any such source as an equivalent thermal noise source which is characterized by an equivalent noise temperature, T_e. Equivalent noise temperature is expressed as

$$T_e = \frac{N_0}{kB}, \tag{2.53}$$

where N_0 is the power delivered by the arbitrary noise source. T_e is best understood as the temperature a matched resistor must hold to produce an equal amount of noise power as the arbitrary source [46].

Shot Noise

Shot Noise is another type of noise that is inherent to most electrical devices. Its physical origin is in the quantized nature of charge carriers of which current flow is composed. Current flow i through a conductor is defined as the amount n of charged particles passing a cross section of a conductor in a given space of time t [38]. That is,

$$i = \frac{qn}{t}, \tag{2.54}$$

where q = 1.6E-19 C is the charge of a single electron. Because the current flow is composed of a number of quantized charges, it is only continuous in the sense that there is a constant mean flow i_0. If one were to count the number of charges at successive instants in time, one would discover that the number of particles will vary randomly between each measure. This is because the motion of each individual charge carrier is random and uncorrelated. The consequence of this is that there will be a fluctuating current superimposed on i_0. We can find the mean as follows;

$$i_0 = \frac{\overline{n}q}{t}, \tag{2.55}$$

$$\overline{n} = \sum_{j=1}^{m} \frac{n_j}{m}. \tag{2.56}$$

Where $\overline{n}$ is the averaged sum of m successive counts [38]. Statistical analysis shows that the root mean square of current variation i_n, is distributed uniformly with respect to frequency and the amplitude of the noise exhibits a Gaussian probability density function [55]. Thus, shot noise sources produces power in a load resistor directly proportional to bandwidth similar to thermal noise sources. RMS current is given as [55],

$$i_n^2(f) = 2qI_0A^2(1/Hz). \tag{2.57}$$

Equation (2.57) is valid for frequencies with periods of shorter duration than the transit time of charge carriers across the device in question.

Other Noise Types

Other types of noise are also common in electrical components and systems. These are, however, generally not of the same magnitude as thermal and shot noise, and will not be explained in detail. Two such types of noise, that both arises from quantized random processes similar to shot noise, are *G–R noise* and *partition* noise. The former is caused by generation and recombination of hole/electron pairs in semiconductors, while the latter is caused by division of emitter current in transistors. They both display the same statistical characteristics as thermal noise and are therefore usually included in the total combined noise effect in noise characterization of the relevant component [55].

Another noise type is referred to as *flicker noise*. Flicker noise is a general term for noise exhibiting a 1/f dependency. Such noise is seldom a concern in microwave circuits as the noise power will be negligible for large frequencies [11].

2.3.2 Noise Figure

Noise figure was standardized by Harold Friis [20] in 1944. Since then it has become a widely used parameter to indicate noise contribution from components and systems. The noise figure is defined as the ratio between signal-to-noise at the input of a component or system, to signal-to-noise ratio at the output. The idea is simple, an ideal lossless component would treat signal and noise propagating through it in the same way. Real components however, will add more noise. Thus, the noise figure is a measure of how much a component or system degrades the signal-to-noise ratio. The basic definition of noise figure is [20] ,

$$F = \frac{S_i/N_i}{S_o/N_o} \geq 1, \tag{2.58}$$

where S_i, N_i are signal and noise powers at the input and S_o, N_o are signal and noise powers at the output. Further, it can be shown that F is dependent on the level of input noise. This is shown through the following equations [55]:

$$S_o = GS_i, \tag{2.59}$$
$$N_o = GN_i + N_a, \tag{2.60}$$

where G is the gain of an arbitrary network and N_a is the noise power added by the network. Combining equations (2.60) and (2.58) results in the following equation,

$$F = \frac{N_a + GN_i}{GN_i}. \tag{2.61}$$

Because most of the noise can be considered to be of thermal nature (section 2.3), N_i has been defined as the maximum available output power from a matched resistor at a reference temperature $T_0 = 290$K, so $N_i = kT_0B$. This is the standard input noise level used to determine noise figure, and results in the standard definition for F as adopted by IEEE[2] [55],

$$F = \frac{N_a + kT_0BG}{kT_0BG}. \tag{2.62}$$

Noise figure as defined in equation (2.62) is a linear value, and is today more often referred to as *noise factor*. It is often useful to describe the amount of degrading of SNR in logarithmic decibels, this is given as

$$NF = 10 \log_{10} F \tag{2.63}$$

and modern use of the term *noise figure* often refers to NF.

2.3.3 Noise Figure and Equivalent Noise Temperature

Equivalent noise temperature T_e, was introduced in section (2.3.1) as a way to characterize noise performance. It can be shown that T_e can be related to

[2]Institute of Electrical and Electronics Engineers

noise factor. Considering a noisy two-port network with gain, G, bandwidth, B and equivalent temperature T_e. If input noise is kT_0B, as previously defined (2.3.2), and output signal is $S_o = GS_i$, the output power will be,

$$\begin{aligned} N_o &= GN_i + kGBT_e, && (2.64)\\ &= kGB(T_0 + T_e). && (2.65) \end{aligned}$$

Substituting the new term of output noise power in equation (2.62), the relation between T_e and F is found as,

$$\begin{aligned} F &= 1 + \frac{T_e}{T_0}, && (2.66)\\ T_e &= (F-1)T_0. && (2.67) \end{aligned}$$

2.3.4 Noise Characterization of Passive Two-Ports

Passive two-port networks are such components as lossy transmission lines, attenuators, capacitors and isolators. For lossy networks a loss factor is defined as L = 1/G. Considering a system at thermal equilibrium consisting of a lossy two-port connected to a matched source resistance, the output power is defined as [46],

$$N_o = kTB = GkTB + GN_{added}. \quad (2.68)$$

Here N_{added} is the noise power delivered by the two-port itself, while kTB is the total noise of the system. Thus, the added noise power can be expressed as [46],

$$N_{added} = \frac{1-G}{G} kTB. \quad (2.69)$$

Inserting the previously defined loss factor this can be expressed as

$$N_{added} = (L-1)kTB. \quad (2.70)$$

Replacing N_o in equation (2.53) with the expression in equation (2.70), the equivalent noise temperature of the lossy two-port can be expressed as,

$$T_e = (L-1)T. \tag{2.71}$$

The noise figure of a passive component is found by combining (2.71) and (2.67) to get,

$$F = 1 + (L-1)\frac{T}{T_0}. \tag{2.72}$$

Thus, under the assumption that a system is at room temperature (T = 290K), the noise figure of a passive two-port network equals its loss factor [46]. Noise figure and likewise, equivalent noise temperature, is therefore easily found from S-parameters of passive devices since gain G = $|S_{21}|^2$.

2.3.5 Noise Characterization of Cascaded Systems

Typical microwave systems, such as a radiometer receiver, consists of several components of various gain and noise properties in a cascade. The noise figure and equivalent noise temperature can be used to characterize a cascade as if it were a single device.

For a simple cascade of only two components, each with their respective gain G_1 and G_2, noise figures F_1 and F_2, and equivalent noise temperature T_{e1} and T_{e2}. The power at the output of stage 1 is expressed as [46]:

$$N_1 = G_1 k T_0 B + G_1 k T_{e1} B, \tag{2.73}$$

where kT_0B is the input noise for the system as defined in section 2.3.2, and kT_{e1}B is the noise contribution of the component. N_1 will the input to the next stage, thus the output is expressed as

$$N_O = G_2 N_1 + G_2 k T_{e2} B = G_1 G_2 k B \left(T_0 + T_{e1} + \frac{1}{G_1} T_{e2} \right). \tag{2.74}$$

The equivalent noise temperature of the cascade is thus found as,

$$T_{cas} = T_{e1} + \frac{1}{G_1} T_{e2}, \tag{2.75}$$

or from the relation in (2.67) as,

$$F_{cas} = F_1 + \frac{1}{G_1}(F_2 - 1). \tag{2.76}$$

The expression can further be generalized for a system of any number of components [46]:

$$T_{cas} = T_{e1} + \frac{T_{e2}}{G_1} + \frac{T_{e3}}{G_1 G_2} + \cdots, \tag{2.77}$$

$$F_{cas} = F_1 + \frac{(F_2 - 1)}{G_1} + \frac{(F_3 - 1)}{G_1 G_2} + \cdots. \tag{2.78}$$

These results reveal an important property of cascaded systems. As each successive step is normalized by the gain of the former, the first few steps are critical to limiting the total noise figure of a system. Thus, to control the total noise figure of microwave receivers it is common practice to place a LNA[3] as early as possible.

2.3.6 Passive and Active Noise Sources

Noise is not always unwanted. In some cases there is need of a controlled noise source for applications such as testing or calibration of microwave receivers. The can either be passive or active sources.

Passive noise sources are usually matched terminations (resistive loads). We have seen how temperature affects output noise from resistors, and this is usually how they are applied, using ie. Peltier elements, or other solutions to adjust temperature for a desired output.

Active sources are driven by an external power source and can be constructed using for example special diodes to obtain a set output. The power delivered by an active noise source could be expressed by equivalent temperature, but since they are often very strong this is inconvenient and *Excess Noise Ratio* (ENR) is used instead. ENR is defined as [55]

$$\text{ENR(dB)} = 10\log\frac{N_g - N_0}{N_0} = 10\log\frac{T_e - T_0}{T_0}, \tag{2.79}$$

[3]Low-noise amplifier

where N_g or T_g is the noise power or temperature of the source. T_0 is the 290K reference temperature and N_0 is the noise power defined by kT_0B. Active noise sources are typically able to deliver substantially higher levels of power than passive noise sources, typical equivalent noise temperatures range from 40 000K to 150 000K.

2.3.7 Y-factor Method

In the ideal case, the noise figure of a device can be measured if the input is connected to a source kept at 0K. The measured output noise would then be that which is generated by the device under test. In practice however, this is virtually impossible [55].

The Y-factor method is an approximation of the ideal case in which two sources of known temperature are used. If the first is kept at a temperature T_1 and the second at a temperature T_2 ,the output of the system for the two cases would be [46]

$$P_1 = kGB(T_1 + T_{sys}), \tag{2.80}$$
$$P_2 = kGB(T_2 + T_{sys}). \tag{2.81}$$

Here T_{sys} is the equivalent noise temperature of the DUT. The Y-factor method requires that $T_1 > T_2$, and Y is computed as the power ratio of the hot and cold source:

$$Y = \frac{P_1}{P_2}. \tag{2.82}$$

By rearranging the terms in (2.82), the equivalent noise temperature can be found as

$$T_{sys} = \frac{T_1 - YT_2}{Y - 1}. \tag{2.83}$$

Accurate measurements of noise figure is usually a very complicated task. All measurement equipment will have internal noise figures which will contribute to an error. To minimize error in noise measurements a few steps can be taken. First, if the DUT has a low gain, the contribution of the measurement device may become large. If, however the DUT has a large gain, its

contribution will be weighted by a larger factor. Usually, if the gain of the DUT is larger than 30dB, pre-calibration can be avoided as the contribution from the measurement equipment is negligible. It is also important to use noise sources which are in the range of the expected noise figure to be measured. For instance, if the expect measured noise figure is between 0 - 10 dB, the hot source should not be larger than 5 ENR [50]. The temperature of the cold source should be chosen such that the Y-factor becomes large. If the Y-factor is too close to 1, the accuracy of equation (2.83) could be at risk if the denominator approximates 0 [55].

Chapter 3

Radiometry

Radiometry in general is the science encompassing all aspects of the measuring and description of natural electromagnetic radiation, mainly which is of thermal nature. Such radiation is naturally emitted by the particles that are the basis of all matter, atoms and molecules. A radiometer is an instrument with which such measurements are made. The radiometer is a passive or remote sensing device, meaning that contrary to radar sensing devices, it is constructed to simply measure incident radiation which translates to an average power in a receiver. In this thesis the main focus is on the use of radiometers in the microwave range of frequencies where remote sensing has found extensive application ($\sim 3.5 GHz$). Because of a relatively long wavelength, microwaves are able to penetrate several types of media. A main area for remote sensing is within environmental research, such as ground mapping, oceanography and atmospheric evaluations, through which for example a better understanding of the spectral properties of the atmosphere has been gained [53, 46].

Microwaves have also shown favorable transmission characteristics in living tissue. Thus, another area where microwave radiometry is currently being investigated is its applicability to biomedicine. In section 1.3 the possibility of using microwave radiometry for the detection of breast cancer was discussed. In the following sections, fundamental theory and results in the context of microwave radiometers are presented. The latter sections are devoted to describe some of the basic microwave radiometer configurations and their performance characteristics.

3.1 Thermal Radiation

Heat, or thermal energy, is defined as the energy that is transferred from one system to another due to a temperature contrast. It can be shown that there is a linear relationship between the temperature of a body and the average kinetic energy of the molecules and atoms of which it is composed. This is expressed as [39]

$$\frac{3}{2}kT = \frac{1}{2}m\hat{v}^2, \tag{3.1}$$

where k is Boltzmanns constant, T is absolute temperature, m is the mass of a single atom and $\hat{v}^2$ denotes its squared average velocity. This relation holds true regardless of the form of motion, be it vibration, rotation or translational velocity. Thus, temperature is a measure of the thermal energy in a body. Conduction, convection and radiation are the three mechanisms by which thermal energy is transferred. The radiation by which heat is transferred is referred to as thermal radiation and though its origin can be explained by a classical approach, it takes quantum physics to fully describe its spectral characteristics [39].

In solid materials, the kinetic energy of atoms and molecules is physically manifested as random vibration, or oscillation, around each atoms respective equilibrium position. The resulting emission of radiation is caused by acceleration of the charged particles constituting the atom, as predicted by Maxwellian electrodynamics. Thus, all real bodies at a temperature above absolute zero will emit thermal energy in the form of radiation. The opposite is also true, all bodies have various capabilities to absorb thermal radiation which translates to heat. Thermal radiation is emitted as a continuous spectrum in a broad range of frequencies [53, 39].

3.1.1 Blackbody and Planck's Law

A fundamental concept in thermodynamics, and to the characterization of thermal radiation, is that of a blackbody. A blackbody is defined as an object consisting of an idealized material which absorbs all incident radiation without reflection and maintains thermal equilibrium, at all times, by emitting an equal amount of energy as it absorbs. As well as having perfect reflective and absorptive abilities, a blackbody is defined as having a uniform emittance of radiance for all angles and frequencies [41].

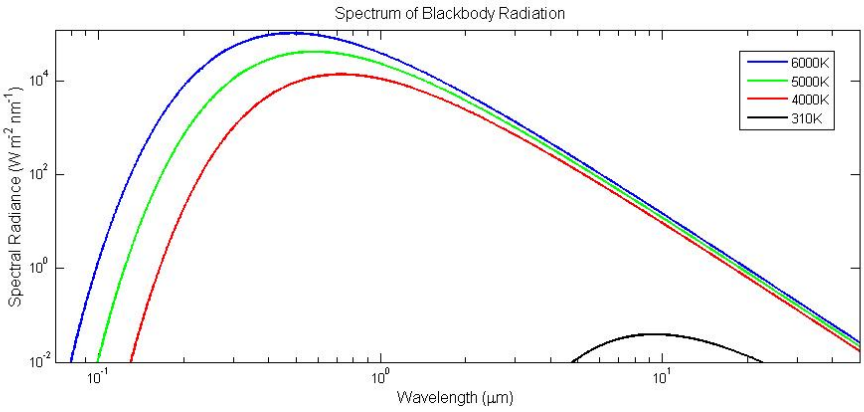

Figure 3.1: Spectral radiance for a blackbody at various temperatures.

The ability to describe the spectral distribution of a blackbody is credited to Max Planck, who in 1901 derived a result based on quantum mechanical consideration. The result is called Planck's blackbody spectral radiation law, often referred to as Planck's law, and is defined as [41]

$$L_{bb\lambda} = \frac{2hc^2}{\lambda^5 \left(e^{hc/\lambda kT} - 1\right)}, \tag{3.2}$$

or, through the relation $\mathrm{L}_{bbf} = \frac{\delta L_{bb\lambda}}{\delta f}$, as a function of frequency by

$$L_{bbf} = \frac{2hf^3}{c^2 \left(e^{hf/kT} - 1\right)}. \tag{3.3}$$

where

h	Planck's constant	$6.63 \cdot 10^{-34}$ Js.
k	Boltzmanns's constant	$1.38 \cdot 10^{-23}$ J/K.
c	Speed of light	$2.998 \cdot 10^{8}$ m/s.
T	Absolute temperature	K
λ	Wavelength	m
f	Frequency	Hz
$\mathrm{L}_{bb\lambda}$		$\mathrm{Wm^{-2}nm^{-1}sr^{-}1}$
L_{bbf}		$\mathrm{Wm^{-2}Hz^{-1}sr^{-}1}$

The quantity L of (3.3) and (3.2), is defined as spectral radiance, where radiance is a measure of the area and solid angle density of emitted energy per unit time. In other words, spectral radiance is the distribution of power

radiated at each wavelength or frequency from a specific position and in a specific direction relative to the surface of a blackbody [41].

Figure 3.1 displays the spectral distribution of radiation from a blackbody as a function of wavelength and temperature. Some characteristic properties of blackbody radiation are observed. One is the apparent shift to lower peak power with increasing wavelength, which results in the fact that at human body temperatures (37^oC) most of the emitted energy lies within the infrared region. The other is that a body at any given temperature has a unique spectral distribution, at no point do the spectral lines intersect.

3.1.2 The Wien and Rayleigh-Jeans Approximation

Two other results that describe the spectral distribution of blackbody radiation is credited to Wien, Rayleigh and Jeans. Both are derived through a classical assumption leading to inaccurate results. They are, nonetheless, applicable within certain areas as convenient approximations.

Wien's law can be derived from (3.3) by assuming that hf >> kT and is expressed as [53],

$$L_{bbf} = \frac{2hf^3}{c^2} e^{-hf/kT}. \tag{3.4}$$

This result can be shown to be an approximation of (3.3) for high frequencies and deviates less that 1% for values of λT $< 3000\mu$m. At room temperature ($\sim$ 300K) this gives the result that $\lambda < 10\mu$m or equivalently, f $> 3\cdot 10^{15}$ Hz.

The Rayleigh-Jeans approximation can also be derived from Planck's law by Taylor series expansion of the exponential term and under the assumption that hf << kT. This results in the expression [53],

$$L_{bb\lambda} = \frac{2c}{\lambda^4} kT, \tag{3.5}$$

or equally

$$L_{bbf} = \frac{2f^2}{c^2} kT, \tag{3.6}$$

which deviates less than 1% from Planck's law for values of λT $> 0.77\mu$m. For an object at room temperature, the approximation is valid for the values

$\lambda > 2.56$ mm or f < 117 GHz. Thus, for microwave radiometric purposes the Rayleigh-Jeans approximation is extensively used.

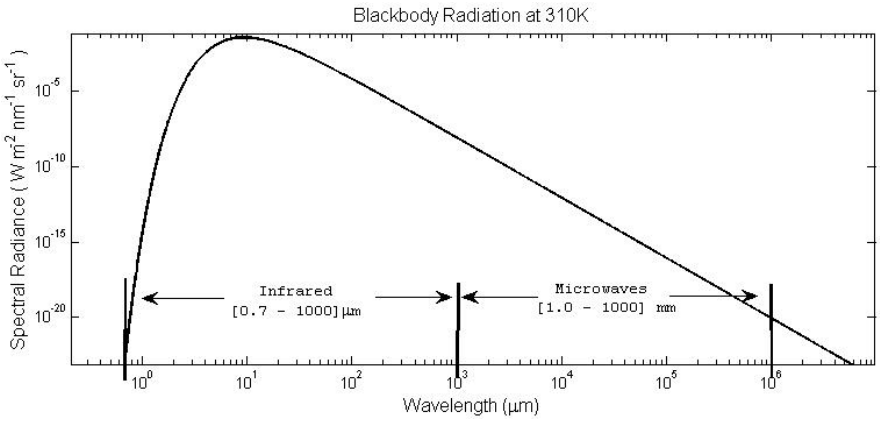

Figure 3.2: Spectral Radiance of a Blackbody at 310K

Figure 3.2 shows the spectral energy emitted by a blackbody at a temperature of 310 K, which is the approximate temperature of a human body. As can be seen, the difference in available power in the microwave region is substantially lower compared to the infrared region. This illustrates the main challenge in microwave radiometry, which is the detection of a very low noise power.

3.2 Microwave Radiometers

The general objective of microwave radiometry is to infer some information about an object or a scene through measuring the power of incident thermal radiation. In many applications, this information is translated as temperature and the radiometer is calibrated in temperature units. In fact, in detection of breast cancer, it is the temperature of the breast tissue that is of greatest interest in a diagnostic phase. Section 2.3.1 presented the theory of noise sources and the linear relation between power and temperature in the microwave spectrum. It is apparent that the source of such thermal noise and thermal radiation is the same, thus they share the same properties and the same mathematics can be applied. As a result, the antenna and the object it measures, can be modeled as equivalent noise sources (see section 2.3.1 – 2.3.5) [46].

3.2.1 Antenna and Brightness Temperature

Using (2.52) the power delivered by a blackbody at a temperature T, is simply $P = kTB$ for an arbitrary system bandwidth B. In reality, few objects are ideal and will consequently absorb and radiate less efficiently compared to a blackbody. The apparent radiometric temperature of non-ideal bodies must then be less than its actual physical temperature. Radiometric temperature T_B is often referred to as *brightness temperature*. The relation between the physical temperature of a body and T_B is expressed as [46]

$$T_B = \epsilon T, \tag{3.7}$$

where ϵ is referred to as emissivity. Emissivity is a dimensionless quantity defined as the ratio of power emitted by a non-ideal body to that of a blackbody at the same temperature. It is the brightness temperature that is measured by a radiometer antenna, and the general problem in radiometry is to find the relation between antenna temperature and T_B.

The emissivity of non-ideal objects is generally a function of several non-ideal characteristics such as inhomogeneity, surface texture (roughness) and dielectric properties. If the object or scene under observation has a non-uniform temperature distribution, an effective brightness temperature as seen by an ideal antenna can be expressed as [46],

$$T_b = \frac{\int_{\phi=0}^{2\pi}\int_{\theta=0}^{\pi} T_B\left(\theta,\phi\right) D\left(\theta,\phi\right)\sin\theta d\theta d\phi}{\int_{\phi=0}^{2\pi}\int_{\theta=0}^{\pi} D\left(\theta,\phi\right)\sin\theta d\theta d\phi}, \tag{3.8}$$

where $T_B(\theta,\phi)$ is the distribution of background temperature and $D(\theta,\phi)$ is the directivity of the antenna. Most antennas are not able to pick up all incident power due to resistive losses in the conducting metal and dielectric materials. This can be characterized by a loss factor L and an internal antenna noise temperature T_p, or equivalently by the radiation efficiency constant, η_{rad} [46];

$$\begin{aligned} T_A &= \frac{T_b}{L} + \frac{(L-1)}{L}T_p & (3.9)\\ &= \eta_{rad}T_b + (1-\eta_{rad})T_p. & (3.10) \end{aligned}$$

Here, T_A is the equivalent noise temperature of the antenna. The radiation efficiency, η_{rad}, is defined as the ratio of the desired output power (of a

transmitting antenna) to the supplied input power. This can be expressed as [46]

$$\eta_{rad} = \frac{P_{radiated}}{P_{supplied}}. \tag{3.11}$$

As antennas are reciprocal, (3.11) is valid for both receiving and transmitting antennas. Thus, if $\eta_{rad} < 1$ for a receiving antenna, it will not deliver the entire collected power to the receiver. Another factor that generally affects the radiometric temperature of the antenna is mismatching. This results in reflection of power at the antenna-receiver or equivalently, medium-antenna interface. The apparent equivalent noise temperature T_a of the antenna will then be [46]

$$T_a = (1 - |\Gamma|^2)T_A, \tag{3.12}$$

where Γ is the voltage reflection coefficient as defined in (2.4).

3.2.2 Brightness Temperature in Lossy Medium

For microwave radiometers in medical applications, the antenna is usually placed flush to a dissipative and non isothermal medium (human tissue). The measured brightness temperature in this case is expressed as a weighted volumetric average of the volume which is "seen" by the antenna near-field [29]

$$T_B = (1 - \rho)\left(\int_V W(\underline{r}, f)T(\underline{r})dV + T_{EXT}\right) + T_{sys}. \tag{3.13}$$

In (3.13), $T(\underline{r})$ is the physical temperature of an object at spatial position $\underline{r}$, W is a weighting function defined for the specific medium and antenna, ρ is the power reflection coefficient due to mismatch, T_{EXT} is the contribution to the temperature from externally picked up interference and T_{sys} is the equivalent noise temperature of the system.

The weighting function is expressed as [29]

$$W(\underline{r}) = \frac{\sigma_m \left|\underline{E}(\underline{r})\right|^2}{\int_V \sigma_m \left|\underline{E}(\underline{r})\right|^2 dV}, \tag{3.14}$$

where $\underline{E}$ is the electric field intensity of a lossy medium, σ_m is medium conductivity for a specific frequency, all terms of loss included. (3.14) can be explained as the normalized power absorption rate distribution when the antenna is operated for transmission. Due to antenna reciprocity, the expression is equivalent for a receiving antenna [29].

W is defined such that if $T(\underline{r})$ is constant, $W = 1$, and (3.13) is reduced to

$$T_B = (1 - \rho)(T(\underline{r}) + T_{EXT}) + T_{sys}. \tag{3.15}$$

3.2.3 The Total Power Radiometer

The total power radiometer is a radiometer in its most simple form. It basically consists of an antenna or probe delivering power to a superheterodyne receiver. A block diagram of a classic power radiometer receiver configuration is shown in figure 3.3. Here the original signal is amplified, usually by an LNA, before it arrives at a mixer controlled by a local oscillator. The mixer converts the RF signal to a fixed and more convenient intermediate (IF) frequency, which is further amplified. In superheteroedyne receivers, most of the gain is usually applied at this stage [46].

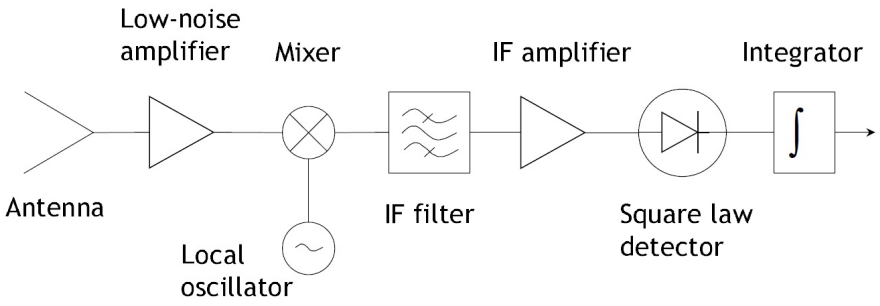

Figure 3.3: Block diagram of a total power radiometer

Following the mixer, there is an IF-filter to determine the pre-detection bandwidth B of the receiver before the signal power P is converted to a corresponding voltage V_{out}, in a linear manner by a square-law detector. Post-detection filtering is required to smooth the output voltage which because of the random, noise-like, nature of the signal will have a fluctuating high frequency component superimposed on a mean value. This is achieved by in-

tegration in the form of a low-pass filter with cut-off frequency of $1/\tau$, where τ is the integration time constant.

Considering for simplicity an ideal, lossless antenna ($\eta_{rad} = 1$) receiving incident radiation from a blackbody at temperature T_B. The power P_A delivered from antenna to receiver can then be found by using equation (2.52), resulting in $P_A = kBT_B$. The receiver itself will contribute a noise power of $P_R = kBT_R$, where T_R is the receiver equivalent noise temperature. As the noise is additive (2.3.1) the power delivered to the detector will be [46],

$$P_{out} = kBG(T_B + T_R), \tag{3.16}$$

and the resulting output voltage will be

$$V_{out} = ckBG(T_B + T_R), \tag{3.17}$$

where G is the effective gain of the receiver and c is the linear sensitivity of the square-law detector, often given as $mV/\mu W$, where V is the proportional output voltage to an input of effect given in watts.

There are principally two sources of measurement error for this type of radiometer. The first is related to the random nature of noise, which leads to a randomly varying output voltage than can be thought of as a random process. Thus, each period of integration is a sample of this random process which can be characterized by a variance and standard deviation. The standard deviation of the measured temperature is expressed as [46],

$$\Delta T_N = \frac{T_B + T_R}{\sqrt{B\tau}}, \tag{3.18}$$

where τ is the integration time. Consequently, there are three ways to reduce the measurement error caused by noise. One is to increase the system bandwidth, though this may not be a viable option in most systems. The second is to minimize the contribution of noise from the receiver itself, which can be done by using a low-noise amplifier early in the setup (see section 2.3.5). The third is to increase integration time.

The second and most dominating source of measurement error is caused by drift in the receiver gain. Amplifier gain is generally a function of temperature and other operational conditions. Temperature changes in amplifiers are most often a result of the active consumption of power over time. For small

components (IC's) with low mass, the temperature can also be altered by thermal convection if there is a varying ambient temperature. Other active devices such as the mixer also contribute to gain variations. For a system calibrated for a fixed gain G this measurement error due to gain variations is expressed as [46],

$$\Delta T_G = (T_B + T_R)\frac{\Delta G}{G}, \tag{3.19}$$

where ΔG is the RMS variation of the system gain. To illustrate the relative contribution of each measurement error, assume a system where $\mathrm{T}_R = 500$ K, $\mathrm{T}_B = 300$ K (room temperature), B = 500 MHz and $\tau = 5$ s. In this situation $\Delta \mathrm{T}_N = 0.016$ K (3.18). A reasonable assumption of $\Delta \mathrm{G/G} = 0.01$, meaning a 1% gain variation, $\Delta \mathrm{T}_G = 8$ K (3.19) [46].

The effective measurement error cause by gain variations is expressed as [46],

$$\Delta T = \sqrt{(\Delta T_N)^2 + (\Delta T_G)^2}. \tag{3.20}$$

Equation (3.20) is often referred to as the radiometer sensitivity. Radiometer sensitivity is equivalent to the temperature resolution of the instrument, that is, how small variations in brightness temperature that can be reliably detected.

3.2.4 The Dicke Radiometer

Depending on the application, demands on sensitivity usually range between 0.1K (medical applications) [29] to 1K (radio astronomy) [53]. Typically, medical radiometers are designed to achieve a sensitivity less than 0.1 K [**?**]. To achieve this, it is evident that a total power radiometer is not ideal, as gain fluctuations will cause unpredictable and possibly large measurement errors. This was addressed by R.H. Dicke in 1946. His observation was that gain variations are slow, with a time constant usually > 1 s. Thus, if one could calibrate the radiometer with a rate much higher compared to the gain dynamics, its significance to the overall measurement error can be reduced, or even eliminated completely [12].

Figure 3.4 illustrates a general implementation of a Dicke radiometer. The receiver is essentially a total power radiometer. The difference is the added switch or modulator at the input to the receiver, which has since been known

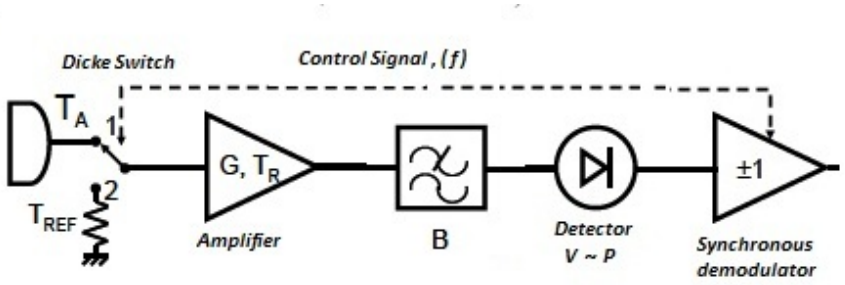

Figure 3.4: Block diagram of a Dicke radiometer

as the Dicke–switch, and a post-detection demodulator preceding the integrators. The Dicke–switch serves to change between the antenna input and a reference load which is kept at a known temperature, T_{ref}. The switch and demodulator are synchronized by a common control signal (square pulse) such that, depending on the input, the output voltage is multiplied by 1 or -1. The resulting outputs can be expressed as

$$V_{out1} = ckB(T_A + T_R), \tag{3.21}$$

for the antenna input, and

$$V_{out2} = -ckB(T_{ref} + T_R) \tag{3.22}$$

when the reference source is connected. The resulting output voltage will then be

$$V_{out} = ckB(T_A - T_{ref}). \tag{3.23}$$

Observe from (3.23) that the voltage is no longer dependent on system noise. This is an important result which can be used to make a calibration curve to determine the antenna temperature as long as the reference temperature is known. The total sensitivity of the Dicke radiometer can then be expressed as [29]

$$\Delta T_{dicke} = \left[\frac{2(T_A + T_R)^2 + 2(T_{ref} + T_R)^2}{B\tau} + \left(\frac{\Delta G}{G} \right)^2 (T_A - T_{ref})^2 \right]. \tag{3.24}$$

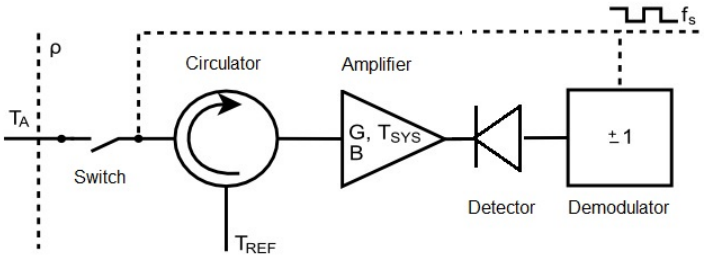

Figure 3.5: Illustration of the switch-circulator configuration

Apparently, measurement error from gain fluctuations is now reduced as it is weighted by the difference between the antenna temperature and the reference temperature. In the event that T_{ref} is equal to T_A, (3.24) is reduced to

$$\Delta T_{dicke} = \frac{2(T_A + T_R)}{\sqrt{B\tau}}. \tag{3.25}$$

In this case the Dicke radiometer is said to be balanced. The gain fluctuations are completely nullified as long as the switching rate is fast enough. Typical switching rates range from $10Hz$ to $1kHz$. A drawback of the Dicke-system is decreased sensitivity, compared to the total power configuration. This is a result of the antenna signal being observed only 50% of the time within each duty cycle.

3.2.5 The Switch-Circulator Dicke Radiometer

A general problem in radiometers is mismatch between antenna and the observed material. This implies that the input temperature of the antenna is related to a power reflection coefficient. Thus, the apparent temperature of the antenna will be as stated in (3.12). Inserting a circulator behind the switch in a Dicke-radiometer, to which the reference is coupled, can reduce the effect of mismatch on the measured temperature [34].

Figure 3.5 illustrates such a configuration. In this case, the reference temperature is coupled to the circuit at all times. When the switch is in an open position, the output voltage to the demodulator will be

$$V_1 = ckGB(T_{ref} + T_{sys}). \tag{3.26}$$

When the switch couples the antenna to the system, the power delivered by the reference source will be reflected back into the circuit at the antenna interface. The output voltage in this case will be

$$V_2 = ckGB(T_a + \rho T_{ref} + T_{sys}). \tag{3.27}$$

Inserting the expression for T_a from (3.12), V_2 becomes [34],

$$V_2 = ckGB\left[(1-\rho)T_A + \rho T_{ref} + T_{sys}\right]. \tag{3.28}$$

After demodulation the output voltage will be the difference of the two signals such that

$$V_{out} = ckGB(1-\rho)(T_A - T_{ref}) \tag{3.29}$$

Consequently, for a balanced Dicke-radiometer ($T_A = T_{ref}$) this configuration will remove both gain and mismatch dependence. For a non-balanced radiometer ($T_A \neq T_{ref}$), the effect of mismatch can be reduced if the reference source is chosen to be close to the temperatures that is expected to be measured. In this case, the radiometer can be calibrated if T_{ref} is known [34].

3.2.6 Balanced Dicke-Radiometers

It is evidently desirable for the Dicke radiometer to be balanced at all times. Typically a radiometer must be able to measure a brightness temperature across a relatively wide range of temperatures, thus if a single, fixed reference is used balance is only achieved for one specific temperature. Consequently, several schemes have been developed to configure the Dicke-radiometer for a constant balance. Some configurations are reviewed in this section.

Duty-cycle Modulation Radiometer

The duty-cycle of a Dicke-radiometer corresponds to the switching rate of the Dicke-switch. For an unbalanced Dicke-radiometer, the antenna and reference channel are coupled to the circuit in equal intervals, meaning the duty-cycle η is equal in both cases. A duty-cycle modulation radiometer applies a feedback system to dynamically adjust the duty-cycle such that

the amount of power collected during each cycle is the same, keeping the radiometer balanced. This can be expressed as [6]

$$\eta(T_A + T_{sys}) = (1 - \eta)(T_{ref} + T_{sys}). \tag{3.30}$$

For this radiometer the sensitivity can be expressed as

$$\Delta T = \sqrt{\frac{(T_A + T_{sys})^2}{B\tau\eta} + \frac{(T_{ref} + T_{sys})}{B\tau\eta}} \tag{3.31}$$

Reference-Channel Modulation

This method uses a variable noise source such that the reference temperature T_{ref} can be adjusted to mirror the measured antenna temperature. This system can be realized by an active noise source and a variable attenuator or using Peltier-elements to vary the temperature of a passive ohmic load. This method results in a sensitivity equal to that of a balanced Dicke-radiometer (3.25) [6].

Two-reference Calibration

The two-reference calibration radiometer is a variant of the switch-circulator Dicke-configuration seen in section 3.2.5. The two internal loads are kept at different temperatures, and a switch is configured to commute between the loads at 50% of the Dicke-switch frequency. A total of four different measurements are then made which can be used to remove the effect of both gain and mismatch variations [6].

Chapter 4

Design and Implementation of a Microwave Radiometer

In this chapter design considerations, component specifications and implementation of the radiometer designed for this study is explained. The radiometer is based on the switch-circulator Dicke-configuration presented in section 3.2.5 and applies a single, fixed temperature reference load. The composition of new components and a solution to a previous issue of amplifier instability has resulted in an instrument capable of measuring realistic temperatures for initial experimental verification. The total radiometric system consists of three separate parts; the front-end receiver, a logarithmic RF detector and a LF-circuit in which the basis for Dicke-operation is implemented.

All components used for the radiometer design are integrated circuits of surface mount technology. This allows the fabrication of a miniaturized instrument on a PCB[1]. Miniaturization is seen as the next logical step towards an instrument which is handy and easy to use in a clinical environment. A further argument towards miniaturization is that ICs are relatively cheap in larger quanta, facilitating the possibility of constructing a low-cost instrument using high quality on-the-shelf components.

Currently, only the radiometer front-end is designed and produced on a PCB. The detector came pre-assembled on a separate PCB and the LF-circuit is currently implemented on a Veroboard, as the design was seen to be experimental and untested.

[1]Printed Circuit Board

4.1 Design Considerations

4.1.1 Sensitivity

One of the most important characteristics of a medical microwave radiometer is its sensitivity. The sensitivity of a radiometer is a measure of its temperature resolution, and will thus be the limit for the smallest temperature gradients the radiometer is able to reliably detect. The required sensitivity is in literature accepted to be at least 0.1^oC.

To satisfy the requirement of sensitivity, it is paramount to reduce the effect of gain variations to a minimum, thus a variation of the Dicke-configuration is generally required. If gain variations can be excluded as a source for increased sensitivity, the sensitivity of the radiometer is found by (3.25). Thus, the most obvious parameters to further increase sensitivity are to adjust integration time and reduce the system noise figure. The system noise figure is basically controlled by careful design of the front-end, as it is in the front of the noise figure cascade (see section 2.3.5).

4.1.2 Gain Stability

The signal levels measured in medical applications are extremely weak. At human body temperatures (37^oC) the power available for detection is approximately -174 dBm/Hz, or equivalently on the order of 10^{-15} W. Assuming a pre-detection bandwidth of 500 MHz, this corresponds to a power level of -87 dBm incident on the front-end receiver. Power available for detection is then dependent on the total forward transmission gain of the system which must be chosen such that the input power to the detector is in the linear range. As discussed in section 2.2.3, the act of cascading amplifiers may present problems with regards to stability. To prevent stability issues to become detrimental to the measurement accuracy of the radiometer, the selected amplifiers should be chosen with stability performance in mind. In addition, circuit design should be carefully considered with regards to the placement of LNAs, especially with regards to distance, voltage supply lines and the possibility to separate the cascade by use de-coupling devices.

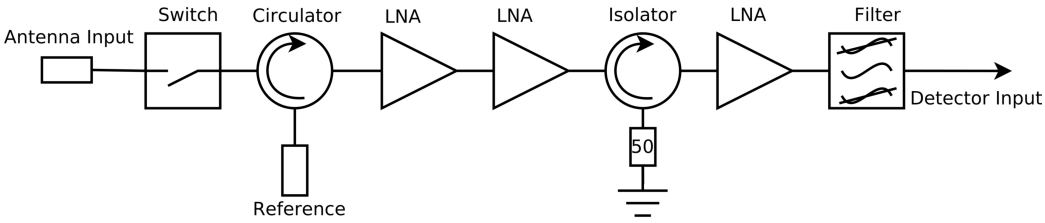

Figure 4.1: Block diagram representation of front-end receiver.

4.2 Front-End Receiver

The front-end receiver explained in this section represents a re-design of a previous implementation in which gain instability issues were detected [31]. The predominant focus has been on optimizing the configuration for a decreased noise figure and improving the issue of instability which was identified as a problem with a triple LNA cascade. Figure 4.1 presents the modified front-end in a block diagram.

4.2.1 PCB and Microstrip

The front-end circuit was fabricated on a Rogers RO4350B laminate, specifically tailored for performance sensitive RF circuits [70]. Table 4.1 gives an overview on the specific laminate dimensions and properties.

Property	Value
Dielectric Constant (ϵ_r)	3.48
Dissipation Factor ($\tan\delta$)	0.0031
Substrate Thickness	0.254 mm
Copper Thickness	35μm

Table 4.1: Front-End PCB specifications.

From the specified properties of the laminate, thickness of substrate and copper layers, a microstrip transmission line has been modeled in CST MICROWAVE STUDIO[2] (see section 5.1). Designing for a 50 Ω characteristic impedance, the transmission line width W used in this design is 0.53 mm.

[2]WWW.CST.COM

The use of miniaturized components of surface mount technology, has resulted in a receiver which is only 50×40 mm^2 in size. The final PCB layout design and the electrical schematic of the circuit are depicted in figure A.2 and figure A.1, respectively.

4.2.2 Pre-LNA components

All components preceding the LNAs will significantly contribute to the overall noise figure of the front-end. For passive devices, insertion loss (S_{21}) is equivalent to the component noise figure. Consequently, insertion loss is a primary performance characteristic when choosing these components.

Dicke-switch

The Dicke-switch represents the first component of the front-end as seen from the antenna. A SPDT RF switch of type CSWA-63DR+ (Mini-Circuits) is used as it has a noise figure of 1.2 dB at the chosen center frequency (3.5 GHz) combined with a high isolation [64]. Due to its absorptive qualities in the input-output direction, an isolation $>$ 50 dB is achieved both between input and output ports and between the input ports. A high isolation is required to reduce leakage when the switch is in an OFF position. If the signal is allowed to leak through the off-port, it could reduce the accuracy of the measured brightness temperature. The switch is matched to 50Ω within the required frequency range and runs on a single positive supply voltage (3-5 V). A single external control signal (0-5 V) can be used to drive the switch.

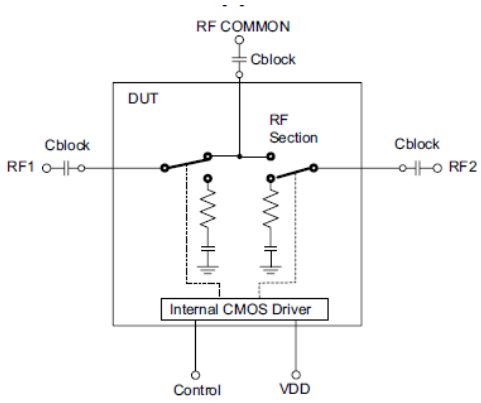

Figure 4.2: Dicke-switch electrical schematic [64].

A schematic of the switch is displayed in figure 4.2. As seen, the switch supplies two inputs with a common output. Only one input (RF1) is required in this design, as the reference load is always connected to the circuit. The RF2 port is left as an open circuit, such that in the case where RF1 is OFF it will appear as a SPST switch to the reference signal.

DC-block capcitors

DC-block capacitors are required at all signal ports of the switch to prevent switching noise to corrupt the signal. For operation between 500 to 6000 MHz, a capacitance of 47 pF is recommended by Mini-Circuits [64]. In the RF range, even small capacitors may have a considerable insertion loss, thus an effort was made to identify capacitors of high quality. In this system a capacitor of type ATC600S (American Technical Ceramics) is used [63]. This is a multilayer ceramic capacitor in NP0 dielectric with an insertion loss < 0.04 dB within the required frequency range. This is an almost negligible value, and should contribute to the effort of reducing the overall noise figure.

Circulator and Reference load

A circulator is a passive, directional, three-port device which allows RF power to be transmitted in one direction only. The directionality is due to the use of a highly magnetic material (ferrite) which presents a high ohmic resistance to any signal in the wrong direction. In the switch-circulator configuration, the circulator is used to couple the reference into the circuit at all times (section 3.2.5). The circulator used is of type 3CDMG35-4 (Dorado International) [62]. It has a bandwidth of 500 MHz (3.3 to 3.8 GHz), corresponding exactly to that of the LNA, in which the insertion loss is < 0.5 dB, VSWR < 1.3 for 50Ω and isolation > 18 dB. The circulator has a clockwise directionality.

The reference source used in this study is a broad banded SMA-type 50Ω passive resistor delivered by Huber+Suhner. For all measurements the load is kept at the ambient room temperature. Thus, as a matched resistive load will be connected to one of the circulator ports, it will effectively appear as an isolator since reflected power from the following circuit is absorbed by the load. The amount of power reflected is very low, such that any power absorbed should not cause the temperature of the load to change during measurements.

4.2.3 LNA and Detector

The low noise amplifier used in this study is of type HMC593LP3 (Hittite), and was mainly chosen for its low noise figure (1.2 dB) and comparatively high gain (19 dB at f_c) [61]. The LNA bandwidth is 500 MHz and its center frequency is 3.55 GHz. As the switch, it is driven by a single supply voltage (5 V) such that only one source is needed to power the front-end. As the LNA has such a low noise figure, the noise contribution of the following circuit elements is minimized drastically.

When the bandwidth of the LNA is used as the systems pre-detection bandwidth (500 MHz), the power incident on the front-end is computed as $P = kTB$ (2.52). Thus, if the radiometer measures an object at 310 K, the power incident on the front-end is -87 dBm. The amount of gain that is required depends on the detector and the range in which it operates in the square-law region. In this study, an active logarithmic detector of type HMC602LP4 (Hittite) is used because of its superior sensitivity [66]. However, the detector is designed such that its sensitivity becomes more linear for higher input powers. For input powers larger than -45 dB, a square-law operation can be approximated if the working point of the system does not change more than a few dB. In this case, the radiometer is intended to measure a limited range of temperatures (20 to 40 ^{o}C). Thus, the input signal will vary by less than $\pm$ 0.15 dB around the working point of the radiometer. It is therefore safe to assume that the detector response is linear within the range which is required.

Consequently, it is required to use three LNA. Dismissing mismatch, a cascade of three LNAs will deliver a gain of 57dB, this results in an input power P = -30 dBm to the detector. As the various passive components of the system will cause the total gain to decrease by several dB, this much gain is needed. Accounting for the total loss due to components and mismatch, an input detector power of approximately -40 dBm can be expected.

4.2.4 Bandpass Filter

The last component of the front-end receiver is the bandpass filter. The choice of bandpass filters is governed by the necessity to limit out-of band interference and define a passband for the system. Right below the passband for which the radiometer is designed, the microwave band is crowded by wireless communication systems ($\sim$ 2.45 GHz). Thus, it is necessary to

attenuate the stop-band to such a degree that any chance of EMI[3] to disturb the measurements is limited. It is also thought that the radiometer could possibly be implemented with wireless capabilities, such as wireless transfer of measured data by ZigBee [31]. If this is to be a possibility, shielding from EMI is paramount.

Due to the requirement of high out-of-band attenuation, a bandpass filter is designed by a cascade of two low pass filters (LFCN-3400+) and two high pass filters (HFCN-3100+), which are are delivered by Mini-Circuits. The passband defined by the filters is approximately 3.1 to 3.95 GHz [67, 65]. Consequently, the effective bandwidth of the system may become larger than the prospected 500 MHz. This however, should work to the advantage of the radiometer performance, as an increased bandwidth contributes to a better temperature resolution (see equation 3.25).

4.2.5 Designing for Gain Stability

A discussion on amplifier stability was presented in section 2.2.3. As there is a need for three amplifiers to provide the required gain, it becomes vital to evaluate the risk of instabilities of the cascade. With regular LF op-amps, the designer has the possibility to apply any of the techniques which was described to ensure the amplifiers will not oscillate. In this design however, the LNA is a pre-designed MMIC[4] for which no such techniques can be used.

To ensure the system will be stable for all frequencies, the technique of implementing an isolator for de-coupling is used. This is illustrated in figure 4.1, which shows that an isolator is used to decouple the last LNA from the preceding dual-amplifier cascade. The immediate effect of implementing an isolator, is to ensure that power is not allowed to oscillate between the first and second stage of amplification, as any power reflected due to mismatch at the input port of the last LNA will be absorbed in the isolator. A secondary effect is that the amplifiers become separated physically. By increasing the physical distance between amplifiers, any electromagnetic feedback is reduced considerably.

The third design approach used to minimize the possibility of instability was handled at the PCB design level. A screen shot of the PCB design is presented by figure A.2. Here it is seen that the voltage supply lines for the last LNA are separated from the supply line of the former LNA cascade. In

[3]Electromagnetic Interference

[4]Monolithic Microwave Integrated Circuit

addition, it was chosen to not double back the tracks to minimize the board size, but instead increase the length of the PCB. This minimizes chances of crosstalk between the devices both through voltage supply lines and through their respective electromagnetic fields.

The isolator used here is in reality the circulator introduced in section 4.2.2. A circulator can be made to function as an isolating device by terminating the middle port in a matched 50 Ω resistive load.

4.2.6 Characterizing DC-block Capacitors

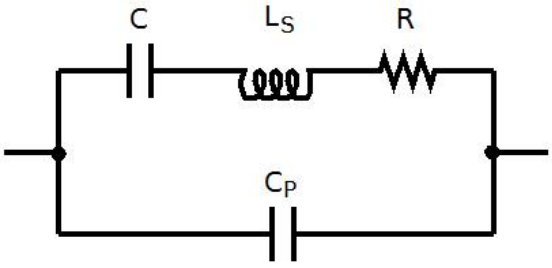

Figure 4.3: Equivalent circuit model for a microwave capacitor.

The importance of choosing the appropriate capacitor should not be underestimated. Microwave capacitors usually become less ideal for higher frequencies due to various parasitic effects. A DC-block capacitor is in microwave systems used to couple RF energy from a part of a circuit to another, while blocking low frequency noise; thus it is placed as a series element [19]. Figure 4.3 shows an equivalent circuit model of a microwave capacitor in series, taking into account the various parasitic effects.

- C – Nominal capacitance.
- C_p – Parasitic parallel capacitance.
- L_s – Equivalent (Parasitic) Series Inductance (ESL), is an inherent inductive characteristic in all capacitors.
- R_s – Equivalent series resistance (ESR), is a loss which is generated by resistance in the dielectric and the metal of the electrodes and terminations.

There are two properties that should be evaluated. The first is the capacitor series resonant frequency, F_{SR} which is expressed as

$$F_{SR} = \frac{1}{2\pi\sqrt{L_s C}}. \tag{4.1}$$

At F_{SR}, the capacitor net reactance is zero, such that the impedance equals its ESR [19]. The other property is the parallel resonant frequency, F_{PR}, at which the RF impedance of the capacitor can increase drastically. This may cause considerable loss of signal power, thus the system should not operate close to F_{PR} [19].

At frequencies lower than the F_{SR}, the capacitor is said to be capacitive and should behave as expected. Above F_{SR}, parasitic inductive effects will be the dominant factor of capacitor performance. This causes the net impedance to increase linearly with frequency [19]. With regards to DC-blocking capacitors, operation above F_{SR} can be tolerated if the net impedance is adequately low [19]. The most fundamental parameter is still the insertion loss (S_{21}) of the capacitor. By viewing S_{21} any presence of parallel resonances can be identified as significant attenuation notches [19].

4.3 LF Circuit

The microwave switch at the input of the front-end enables the radiometer to operate by the Dicke-principle. Thus, a system is needed that is able to synchronously demodulate the two different output voltages from the front-end as described in section 3.2.5. As the radiometer is designed for calibration with a single, fixed reference, a single control signal can be used to synchronously drive the microwave switch and the synchronous detector. For the purpose of this study, an analogue demodulation technique is used. The LF-circuit which implements the demodulation is designed as a separate entity. This allows more flexibility in experimental verification.

Figure 4.4 displays the schematic for the first stage of the LF-circuit. The input connector is of type SMA such that it can be connected directly to the front-end output. As the RF detector is biased, the output voltage is a composite signal of the detected voltage (signal of interest) superimposed on a DC-level. Thus, a polar electrolyte capacitor with a large value ($C_{in} = 22\ \mu$F) is placed at the input of the circuit. C_{in} acts to AC-couple the signal such that the DC-bias at the output of the detector is removed.

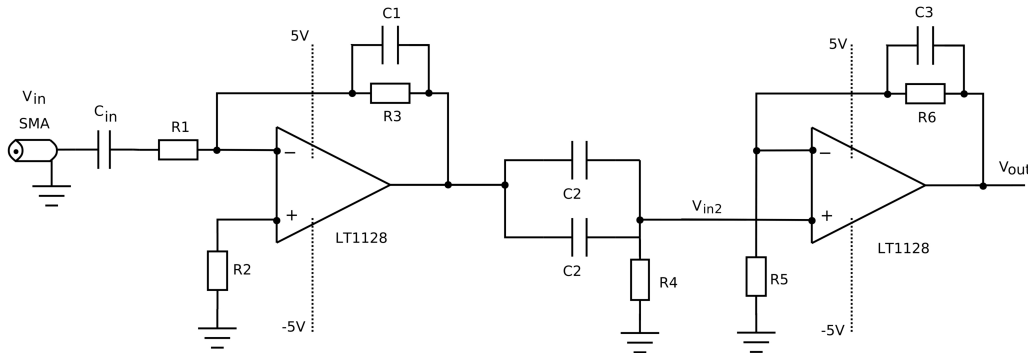

Figure 4.4: Schematic of LF input-circuit and LF-amplifiers.

The resulting signal will be on the order of mV, depending on the temperature measured by the antenna. The operational amplifier used is of the type LT1128, delivered by Linear Technology [68]. The op-amp is designed for low-noise contribution, is stable for both inverting and non-inverting configurations and has a very low CMRR[5]-value. The first stage is designed with an inverting configuration. This is necessary, since the polar capacitor (C_{in}) which is mounted such that its positive plate is faced towards the input, can only function correctly if the potential at the negative plate is low. Thus, since the negative plate is coupled to the inverting input of the op-amp, it is ensured this condition is always met.

Both amplifiers are designed with a band-limiting filter configuration by placing a capacitor in parallel with the resistor in the feedback-loop. The main purpose is to limit gain of high frequencies to ensure the amplifier cascade will be stable. Another effect of such filtering is that any information in frequencies above the filter cut-off frequency will be lost. Therefore, the cut-off frequency of the filters are in both cases chosen to be relatively high ($\sim$ kHz) such that little information is lost.

The total closed-loop gain, G, delivered by the circuit is found as

$$G_1 = -\frac{R3}{R1} \quad \text{(Inverting Amp)}, \tag{4.2}$$

$$G_2 = \left(1 + \frac{R6}{R5}\right) \quad \text{(Non-inverting Amp)}, \tag{4.3}$$

$$G = G_1 G_2 \quad \text{(Total gain)}. \tag{4.4}$$

[5]common mode rejection ratio

Thus, the gain can be tailored by choosing correct values for each resistor. The final design used in this study applied the following values; R1 = 10 kΩ, R3 = 390 kΩ, R5 = 10 kΩ and R6 = 100 kΩ, resulting in a total LF-gain of $G = 429$, or 26.3 dB. The capacitor values in the feedback circuits have values C1 = 68 pF and C2 = 150 pF. The filter cut-off frequency is found as,

$$f_c = \frac{1}{2\pi C R_C} \tag{4.5}$$

Where R_C is the frequency dependent resistance of the capacitor. The cut-off frequency is the frequency for which the signal power is reduced by 50%, this is where R_C is equal to the parallel resistor value. Thus, by equation (4.5) f_c is 6 kHz at the inverting amplifier and 10 kHz at the non-inverting stage.

4.3.1 Synchronous Detector

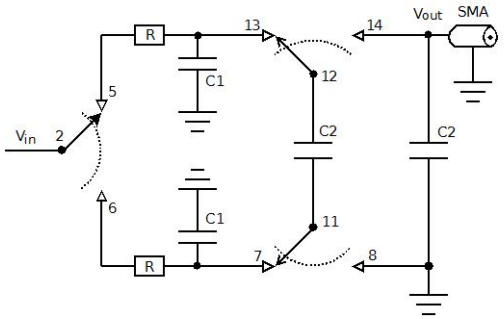

Figure 4.5: Schematic of analogue synchronous detector.

Demodulation, or synchronous detection, is the last stage of the LF-circuit. The Dicke-principle is based on sampling an output voltage which is the difference between the reference and antenna signal after integration. A common way to solve this is by using sample and hold capacitors and an A/D converter such that the voltages are compared digitally after multiplying one of the voltages by -1. For the purpose of this study, the entire LF-circuit is based on analogue techniques.

Figure 4.5 illustrates the schematic of the circuit. The first switch (2) is synchronized with the microwave switch. Thus, when the antenna is coupled to the circuit, the detected voltage is placed at the top capacitor (C_1). When the reference load is coupled to the circuit, the detected voltage is placed on the bottom capacitor (C_1) in figure 4.5. Instead of multiplying one of the

signals with -1, the charges from the top capacitor are moved to the top plate of an intermediate capacitor while the charges on the bottom capacitor are moved to its bottom plate. Thus, the intermediate capacitor effectively holds the differential voltage as expressed in equation (3.22). As a consequence, any residual bias from the preceding circuit is canceled. The differential voltage is referenced to ground by moving the charges off the intermediate capacitor to the output capacitor. At the output, a SMA connector is placed to allow easy connectivity to measuring equipment.

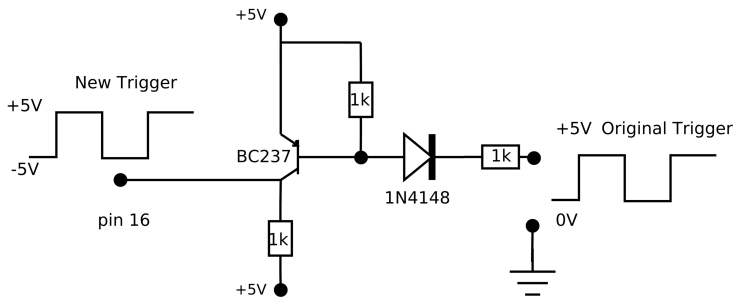

Figure 4.6: Schematic of pulsed voltage conversion circuit. Converts original 0-5V trigger pulse to -5V – +5V trigger pulse.

The switch used in this design is of type LTC1043C, delivered by Linear Technology [69]. It is a multi-switch device in which all switches are synchronously triggered by an external control signal. Only one signal is needed to trigger all switches, including the front-end microwave switch. Originally, the control signal is a square wave of 0 V and 5 V. The LTC1043C needs a control signal that is either -5 V or 5 V. This is solved by a small circuit at the input of the trigger pin (pin 16). See schematic in figure 4.6.

4.3.2 Integration and Sensitivity

The hardware integration time constant is decided by the value of the C_1 capacitors and the series impedance seen looking towards the input of the LF-circuit. The integration time is then found by the expression,

$$\tau = (R_{out} + R_{Sw1} + R)C. \tag{4.6}$$

Here R_{out} is the closed-loop output resistance of the LT1128 and R_{Sw1} is the internal resistance of the switch when ON. These are found in the data sheets of the respective devices [68, 69]. In this design, the value of R is 0 Ω. The resistance of the LTC1043 when ON is 700 Ω maximum. The closed-loop output impedance of the LT1128 is maximally 0.1 Ω at 10 kHz. The nominal capacitive value of the C_1 capacitors is 100 μF. Thus, the resulting time constant with the current values will be

$$\tau = (0.1 + 700)10^{-4} = 0.0701s. \tag{4.7}$$

Due to the short time of integration, it is expected that the sensitivity of the radiometer will not meet the requirement of 0.1 ^{o}C on a hardware level. This was chosen due to the possibility of software post-processing, which is used when handling data from the various experimental measurements. Solutions using running average filters or block averaging can be implemented in software to increase integration time and evaluate the resulting sensitivity. As seen by equation (4.6), the hardware integration time is easily changed by simply replacing the current 0 Ω resistors (R) in figure 4.5, with resistors of a higher value.

4.4 Reducing the Effect of EMI

Initial experiments on the radiometer were conducted with the entire radiometric system in free air. It was soon discovered that in this state, the entire system, especially the RF part, was extremely sensitive to external electromagnetic fields. The slightest movement would result in induced currents due to being accelerated in an electromagnetic field. In addition it was experienced that the cables used for voltage supply and control signal were not of adequate quality and could in some instances act as antennas for external signals into the system. All problems were identified as stemming from the RF-devices (front-end and detector).

It was thus decided to mount front-end and detector in a steel box. As steel is a conductive medium, it will shield the RF-devices from external EMI when the box is sealed off such that it there are no entrance points (gaps or holes) for electromagnetic radiation to enter the enclosure. It effectively works as a miniature Faraday cage. It is also important that the steel box is not lacquered, as paint will act as an insulator. This could cause the inside of the box to act as a resonance chamber as the RF front-end will itself be

a source of radiation due to the various active devices. Consequently, it was made sure the box itself and the steel lid had good electrical contact, such that the electrical (ground) potential of the box remains uniform. If it does not, the system will be prone to anything that would cause the potential to change at various areas. The ground potential should also be shared between the RF devices and the box.

In addition to mounting the RF-devices in the box, all regular cables for voltage supply and switch control signals were replaced by insulated coaxial cables. These are fed into the box through bulk-head feed-through coaxial connectors, such that the enclosure remains sealed. Since voltage supply lines may carry high frequency transients into the system several small, parallel, bypass capacitors of different values are used. Bypass capacitors provide a low-impedance path to ground for high frequencies.

Chapter 5

Numerical Simulation and Estimates

This chapter presents results of numerical simulations and estimates derived from simulated parameters. The various devices have been characterized by the manufacturer in terms of S-parameters. The main software used for simulations of components and cascade of components is the CST STUDIO SUITE^{TM}. Two modules available in the suite has been used for simulation. CST DESIGN STUDIO allows simulation of device performance and performance of cascaded devices, by means of S-parameters. S-parameters are imported to TOUCHSTONE-blocks for each device. The TOUCHSTONE-block represent each device as a linear 2-port network, completely characterized by its S-parameters. The various devices can then be coupled by using blocks representing various transmission line geometries, or by virtual (ideal) transmission lines. The other module is CST MICROWAVE STUDIO, which is an advanced electromagnetic simulation program based on the FIT[1]-method. The module provides solvers able to simulate electromagnetic problems on full scale 3-D models.

Results generated in CST are mainly exported to MatLAB for further processing and plotting. The capacitor performance was simulated by the software Tech-SELECT v5.0 which is supplied by the manufacturer (American Technical Ceramics).

[1]Finite Integration Technique

5.1 Microstrip Simulation

For smaller problems in microwave design, such as simulation of a single components behavior, or a cascade of a few components, the effect of the transmission line can be neglected if it is not of considerable length. Especially if it is not of an unusual geometry, such as a straight line. At radio frequencies, however, the geometry of the transmission line may become important, as reflections and other phenomena such as capacitive and inductive effects can cause loss of signal power. Thus, a geometry other than a straight line may alter the transmission characteristics to such an extent that its transmission properties could become vital.

The use of circulators, which have pins that are at an angle, resulted in the need for some transmission line segments to be curved. As curved lines are a slightly unusual geometry, it was decided to model the microstrip in CST MICROWAVE STUDIO. Two geometries have been modeled, one for a curved line and one for a straight line. The results of each model are used to store S-parameters as TOUCHSTONE-files. This allows the possibility to model the effect of each section of microstrip what connects the devices on the PCB and should consequently result in a more complete simulation.

5.1.1 Modeling the Microstrip

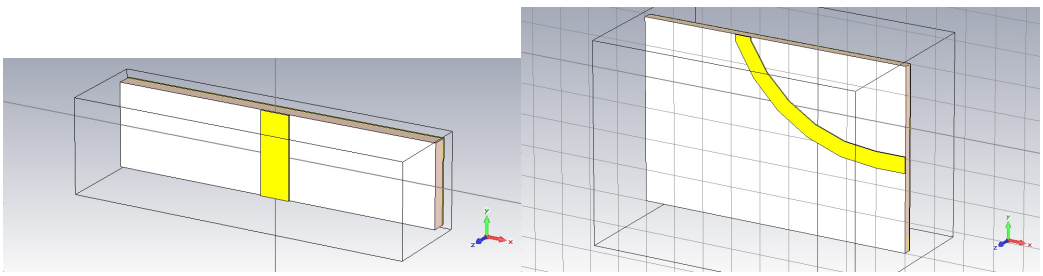

(a) 3-D model of straight microstrip line. (b) 3-D model of curved microstrip line.

Figure 5.1: 3-D models of microstrip transmission lines created in CST MICROWAVE STUDIO.

The microstrip transmission lines are modeled as complete 3-D structures. The structure consists of three components which are defined by parameters as close to the real materials as possible.

1. (Top) Transmission line
2. (Middle) Rogers RO4350(B) Dielectric
3. (Bottom) Ground plane

Material properties of the RO435B substrate are found in the CST MS library of materials. There are only two different materials as the transmission line and the ground plane both consists of the same copper type. The most critical properties used are:

- Copper (Lossy Metal):
  - Electrical Conductivity (σ) = $5.8{\cdot}10^7$ [S/m].
  - Permeability (μ) = 1.
  - Density (ρ) = 8930 [kg/m^3].
  - Thermal Conductivity = 401 [W/K/m].
- RO4350(b) dielectric:
  - Permittivity (ϵ) = 3.66.
  - Permeability (μ) = 1.
  - Dissipation factor ($\tan\delta$) = 0.004.
  - Thermal Conductivity = 0.62 [W/K/m].
  - Density (ρ) = 1.86 [gm/m^3].

5.1.2 Microstrip Simulation Results

To calculate the S-parameters of the transmission lines, the transient solver available in CST MICROWAVE STUDIO is used. The transient solver is a multipurpose solver for a wide range of electromagnetic problems and is suited for problems such as transmission line behavior in a broad frequency range. Figures 5.2a and 5.2b displays the simulated S-parameters for a straight line, while figures 5.3a and 5.3b displays the S-parameters of the curved line.

The transmission line width used in the simulation was W = 0.53 mm. For a the straight line model, this resulted in a characteristic impedance Z_0 of 50.1 Ω and an insertion loss of 0.002dB. For the curved line, the same width resulted in a characteristic impedance of 51.7 Ω and an insertion loss of

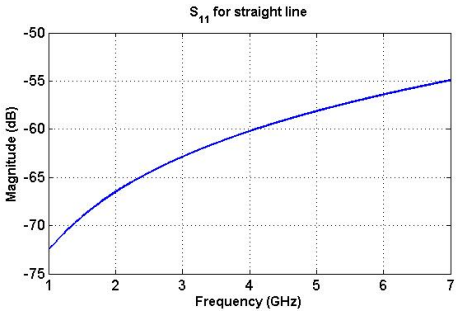

(a) S_{11} for straight microstrip line

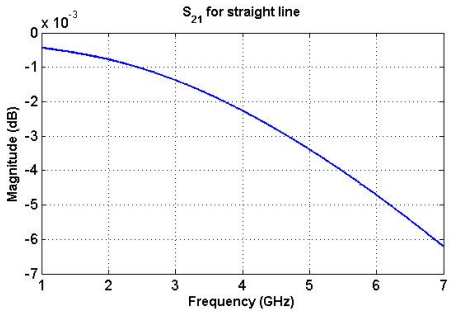

(b) S_{21} for straight microstrip line

Figure 5.2: Simulated S-parameters for straight microstrip line.

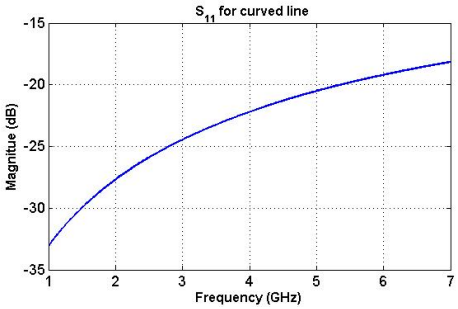

(a) S_{11} for curved microstrip line

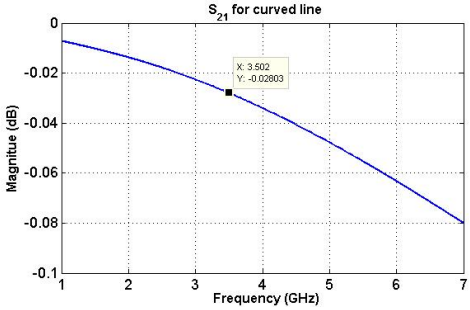

(b) S_{21} for curved microstrip line

Figure 5.3: Simulated S-parameters for curved microstrip line.

0.028 dB. Consequently, the microstrip width used in the actual design was chosen to 0.53 mm. It is also observed that the curved line displays an increase in insertion loss, which is probably due to reflections.

5.2 Switch

The switch is characterized by its S-parameters, from which insertion loss, isolation and return loss can be evaluated. Figure 5.4 displays the return loss of the output port (S_{11}) and of the input ports when ON (S_{22}). The switch is well matched within the bandwidth of the system with S_{11} = -16.9 dB and S_{22} = -17.1 dB at 3.5 GHz.

Figure 5.5a displays the isolation between the input ports when one is open and the other is closed (blue line) and isolation between the input port and

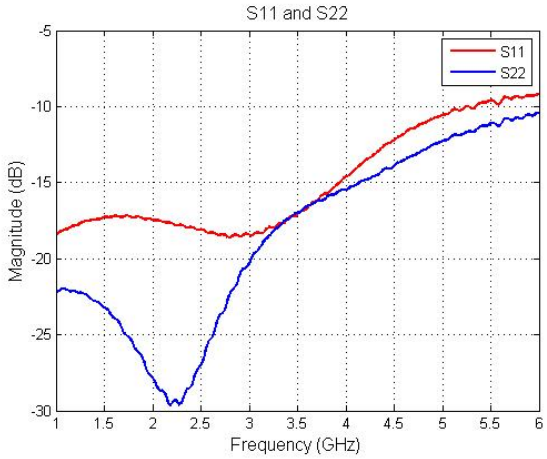

Figure 5.4: Input and output return loss of switch.

the port which at any time is closed (red line). The first case related to the attenuation between input port and in the latter to attenuation from the input to output. At 3.5 GHz it is observed that isolation is -57.4 dB and -49.6 dB respectively.

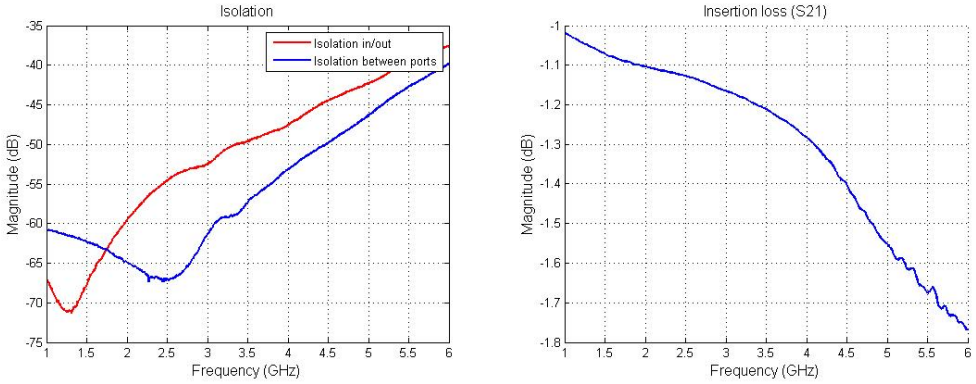

(a) Switch isolation.

(b) Switch insertion loss (S_{21}).

Figure 5.5: Insertion loss (S_{21}) and isolation of RF Switch

The insertion loss, S_{21}, is displayed in figure 5.5b. Insertion loss degrades less than 0.1 dB within the passband and is 1.2 dB at 3.5 GHz. This corresponds to an equivalent noise temperature of 93.2 K.

5.3 DC-Block Capacitor

The transmission characteristics of the DC-block capacitors are important in two aspects. First, as it is placed very early in the circuit, its contribution to the overall noise figure of the front-end could be significant if it has a large insertion loss value. Secondly, it is important to identify F_{SR} and F_{PR}, where transmission characteristics can be significantly altered (see section 4.2.6).

The capacitor behavior was simulated using Tech-SELECT (v5.0), which is a program delivered by the manufacturer, ATC [63].

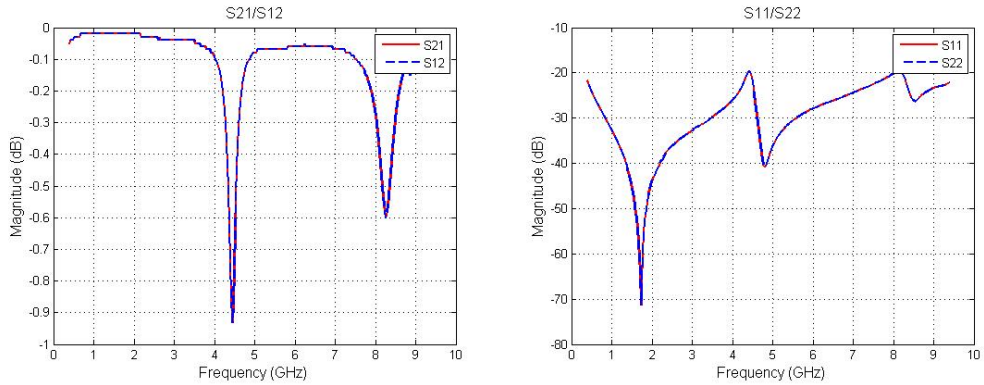

(a) S21 and S12 (b) S11 and S22

Figure 5.6: S-parameters of DC-block capacitor (Vertically mounted).

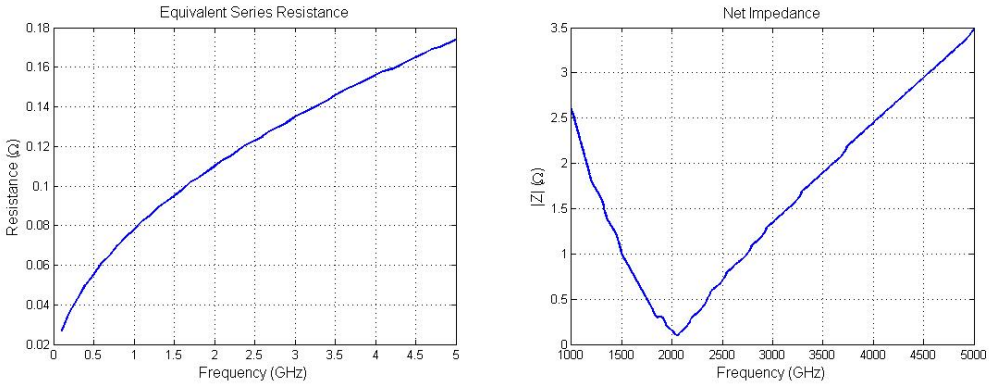

(a) ESR (b) Impedance $|Z|$

Figure 5.7: ESR and Impedance (magnitude) of DC-block capacitor.

Figure 5.6 displays the S-parameters of the capacitor as a function of fre-

quency, where S_{21} and S_{11} represents insertion loss and return loss in dB respectively. At 3.5 GHz, $S_{21} = 0.04$ dB, which corresponds to an equivalent noise temperature of only $T_e = 2.7$ K. Thus, the capacitor influence on the total noise figure should be almost negligible. The first parallel resonant frequency is identified by the obvious "notch" in S_{21} that occurs at 4.45 GHz, this is well outside the passband of the system and should not be an issue.

It is important to note that this result if for a vertically mounted capacitor. For a horizontally mounted capacitor, the first parallel resonant frequency occurs at 2.6 GHz [63]. Insertion loss is not altered by mounting direction. Figure 5.7 displays ESR (5.7a) and impedance, $|Z|$ (5.7b). The series resonance frequency, F_{SR}, is the frequency where $|Z|$ is at a minimum, which is where net reactance is zero. For this capacitor $F_{SR} = 2040.9$ MHz. This indicates that the capacitor is inductive within the passband of our system. Evaluation of $|Z|$ shows that the impedance increases linearly from 1.7 to 2.2 Ω between 3.3 and 3.8 GHz, which is acceptably low.

5.4 Circulator

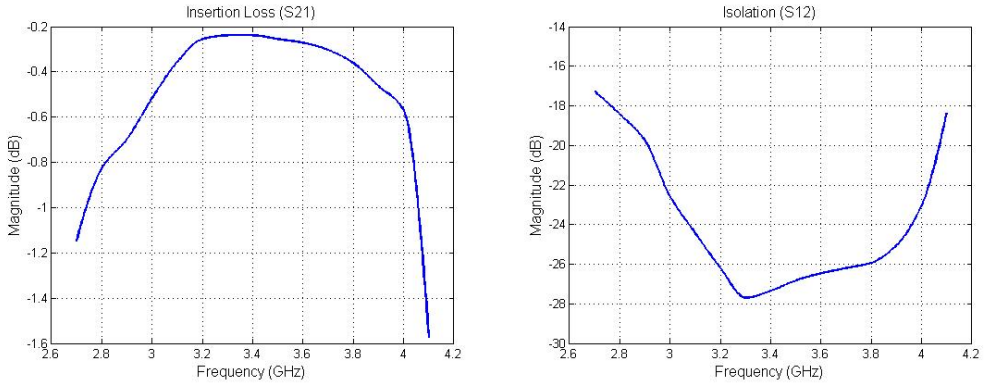

(a) Insertion loss (S_{21}) in dB (b) Isolation (S_{12}) in dB

Figure 5.8: Typical values of S_{21} and S_{12} for circulator.

S-parameters for the circulator could not be obtained from the manufacturer. Thus, the data presented here is estimated by extracting the typical values from a diagram in the data sheet. Interpolation was used to obtain sufficient data points. The S-parameters available is for the relation between two ports only, thus it is assumed that the relation between any two ports are comparable. The lack of data for a wide range of frequencies will necessarily impede any further simulations, with regards to the frequency range available for evaluation, where the circulator is a component.

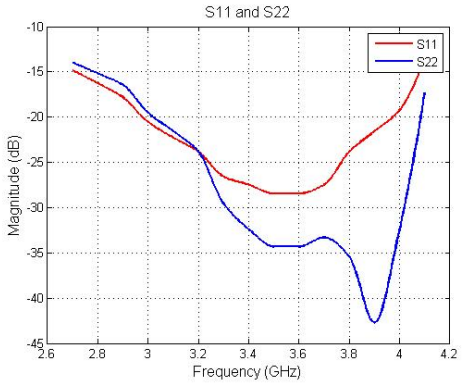

Figure 5.9: Typical values of S_{11} and S_{22} for circulator.

Figure 5.8 shows the typical insertion loss (a) and isolation (b) of the circulator. Within the range 3.2 to 3.8 GHz, insertion loss ranges from a minimum

of 0.24 dB at 3.2 GHz to 0.36 dB at 3.8 GHz. At the center frequency of 3.5 GHz, IL = 0.26 dB. This corresponds to an equivalent noise temperature of $T_e = 17.9$ K. Isolation in the reverse direction amounts to more than 20 dB. S_{11} and S_{22} indicates a good match to 50 Ω.

5.5 Low-noise Amplifier

This section presents simulated results related to the low-noise amplifier, HMC593LP3. The amplifier is in many ways the most critical component of the front-end as it plays the role of supplying signal gain as well as decreasing the noise figure of the system. As a cascade of three LNAs is needed for sufficient gain, simulations and numerical analysis of stability is also considered.

5.5.1 Single LNA

Figure 5.10 shows the S-parameters of the device, when run on a +5 V supply voltage.

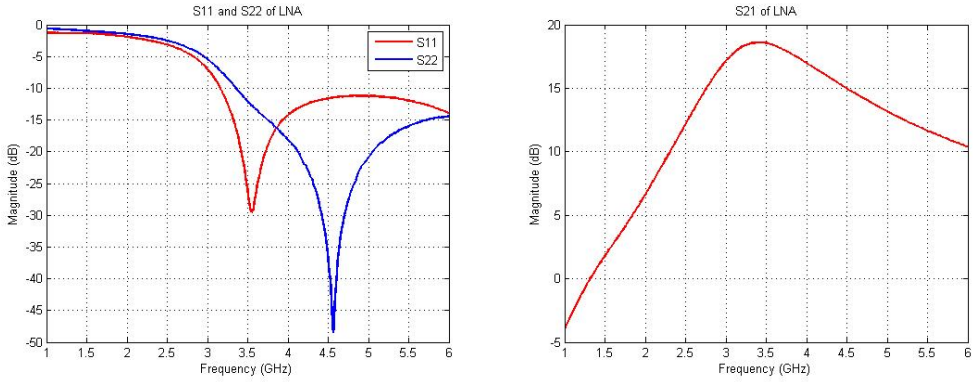

(a) S_{11} and S_{22} (dB)

(b) S_{21} (dB)

Figure 5.10: S-parameters of LNA

Maximum gain is found at 3.45 GHz. Within the specified bandwidth of 3.3 to 3.8 GHz, S_{21} range from 18.5 to 17.7 dB. Here S_{11} and S_{22} range from -14.1 to -17.6 dB and -9.2 to -15.5 dB, respectively. Apparently, the output port is not as well matched as the input port. If the bandwidth is defined as where gain drops by 1 dB at either side of 3.5 GHz, the bandwidth seems to be as wide as 797 MHz, ranging from 3.07 to 3.84 GHz.

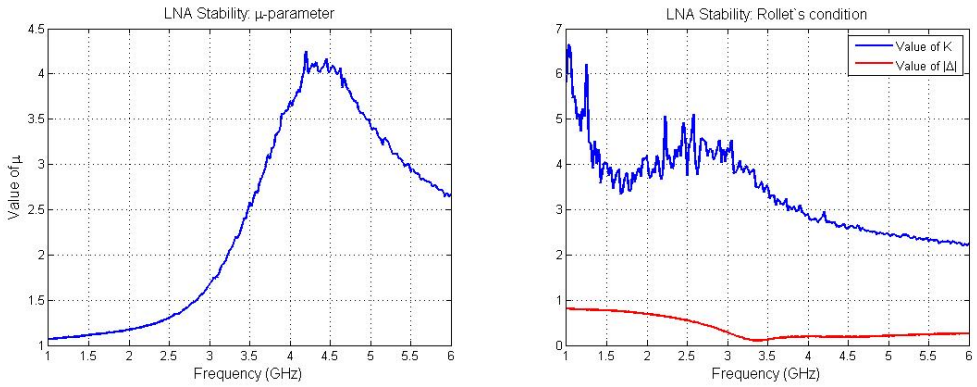

(a) Values of μ (b) Values of K and $|\Delta|$

Figure 5.11: LNA Stability parameters

Amplifier stability is evaluated by computing Rollet's condition (2.46) and the μ-parameter (2.48). The results are displayed in figure 5.11, from which it is seen that the LNA meets the criterion for unconditional stability for both conditions.

5.5.2 Evaluation of Cascade Stability

It has previously been established that the use of three low-noise amplifiers in a cascade results in an unstable system, causing it to oscillate within the passband. In addition, it has been found that for a cascade of two LNAs, stability is preserved [31]. Unfortunately, simulations of cascaded amplifiers using S-parameters does not allow adequate estimations of the stability of the cascade. The reason is simple. The LNA's are active devices and will have operation dependent variables, which may change with temperature. Thus, at the intermediate stages of the cascade a simple S-parameter simulation cannot infer information about the local, or intermediate, stability. For the same reason, calculating the stability from simulated results of a cascade is of little value as the intermediate stages cannot be evaluated. Evaluation of stability in amplifier cascades is in general a complex problem.

In this design, an isolator is placed between the second and third stage of the cascade. The isolator has a de-coupling effect. Any power reflected at the input of the last LNA, will be coupled to, and absorbed, in a 50 Ω load. Thus, in one sense it becomes the output matching circuit of the middle LNA. In the other case, it becomes the input matching circuit of the last LNA.

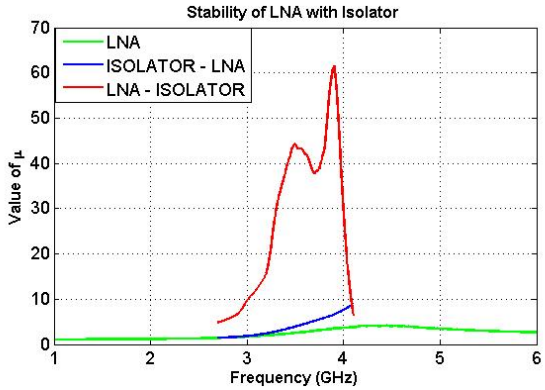

Figure 5.12: Comparing stability parameters of LNA and combinations with Isolator.

As the isolator is a passive device, it can be included in the stability analysis as it will appear as a part of the matching circuit. Two simulations are done. One for the case where the isolator will be a part of the input matching network of the last LNA, the other when the isolator is part the output matching network of the middle LNA of the cascade. In both cases, this will give a good indication of the effect the isolator will have with respect to the stability of each LNA.

Figure 5.12 displays the simulated μ-parameter for the LNA itself, the LNA with the isolator at the input and the LNA with the isolator at the output. It is observed that the greatest effect is seen when the isolator provides matching at the output. Perhaps not entirely surprising if the S-parameters of the devices are compared (figure 5.10a and 5.9). The isolator provides a much better match at the output port within the bandwidth. It is seen that in both cases, the stability within the frequency range is increased. The μ-parameter (2.48) gives a direct indication of the relative stabilities, so it can be concluded that by implementing the isolator, the margin of stability is increased drastically.

Thus, factoring in the total effect the implementation of an isolator provides with regards to stability (see section 4.2.5), it should be safe to conclude that de-coupling of the LNA cascade, by means of an isolator, will result in a stable system able to provide sufficient gain for measurements on sources with realistic temperatures ($\sim$310 K).

5.6 Bandpass Filters

As it is necessary to use a cascade of two low pass filter and two high pass filters, the combination should be simulated to evaluate the performance of what will effectively be a bandpass filter. As the bandpass filter is the last component of the front-end, its output return loss (S_{22}) will decide the output matching of the receiver. Figures 5.13a and 5.13b display the simulated S-parameters of the filter cascade.

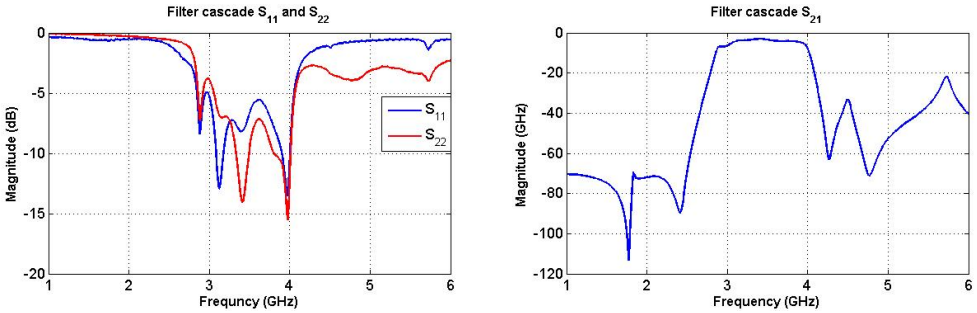

(a) S_{11} and S_{22} of filter cascade. (b) S_{21} and S_{21} of filter cascade.

Figure 5.13: Simulated S-parameters of filter cascade.

As can be seen by the S_{11} and S_{22} parameters, the effect of combining four filters is not ideal. Within the passband the values are fairly acceptable, but do display some unwanted peaks causing the matching to be less than ideal. In this case, the cascade is configure by two LP-filters followed by two HP-filter. It is possible to use other configurations, but simulation conducted elsewhere shows there is not much to gain [31].

The average return loss values can be accepted as it is crucial that the out-of band signal is attenuated to a large degree. S_{21} displays the forward transmission gain (or insertion loss), and shows good flatness within the passband and a sharp attenuation outside it. This will be sufficient to ensure the effect of external EMI is limited. The attenuation within the passband varies between -3 and -4 dB, which is an acceptable loss as the LNA cascade provide more than sufficient gain.

5.7 Complete Front-End Simulation

For a best possible estimate of the expected input detector power, the entire front-end is simulated, including the models for transmission lines. Figure 5.14b displays the simulated forward transmission gain. The maximum gain is approximately 47.9 dB at 3.4 GHz, and overall the gain is relatively flat within the passband. The 3 dB-bandwidth is found to be 719 MHz.

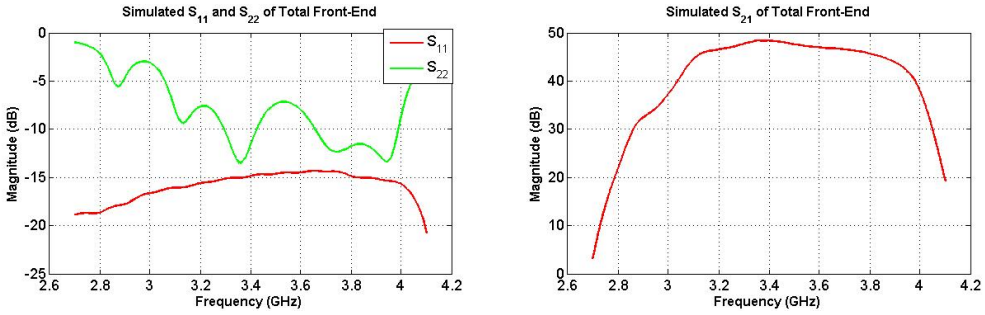

(a) S_{11} and S_{22} of total front-end. (b) S_{21} and S_{21} of total front-end.

Figure 5.14: Simulated S-parameters of total front-end, including transmission lines.

Figure 5.14a displays the simulated S_{11} and S_{22} parameters. The matching at the input port is seen to be good within the passband, the output port seems to have a less optimal match, which is due to the filter cascade.

The total simulation includes the circulator and isolator which only have data specified for a limited range, consequently, the system can only be simulated for the range in which they are defined. Nonetheless, the resulting parameters are sufficient for further evaluations. As the attenuation is sharp outside the passband, the power that would be included if a larger frequency range was available is negligible.

5.8 Estimates of Output Power

The forward transmission gain G ($|S_{21}|^2$) as simulated for the total front-end can be used to calculate the expected input power to the detector. S_{21} is originally given in dB, but G can be found as follows;

$$S_{21dB} = 10 \log_{10} |S_{21}|^2, \tag{5.1}$$

so,

$$G = |S_{21}|^2 = 10^{(S_{21dB}/10)}. \tag{5.2}$$

The power spectrum is then found through the equation $P = kTG$, and the total estimated effect at the output of the front-end is found by integration over all frequencies. For a perspective on the minute powers measured by a medical microwave radiometer, power is calculated for a source at room temperature (290 K) and for the approximated temperature of a human body (310 K). In the first case this results in an output power of -35.9 dBm (0.26 μW) and in the latter case -35.6 dBm (0.28 μW). Thus, it is seen that the difference in power for an increase of 20 ^oC is approximately 0.3 dB.

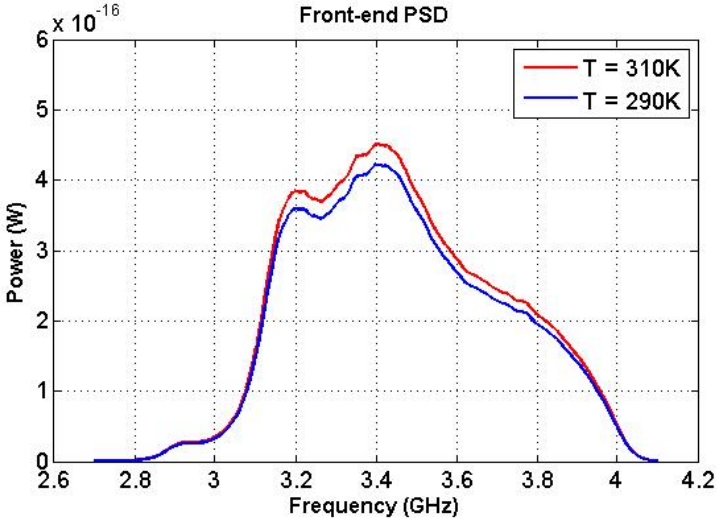

Figure 5.15: Simulated power spectrum density of front-end.

The simulation should be taken as an optimistic approximate as not all conditions on the front-end can be accounted for. Mismatch between component pads and transmission line, and mismatch between pads and component pins, is an effect that is difficult to estimate. The transmission lines themselves do not represent a large loss, and the width of the lines are designed for the best possible match (see section 5.1.2). The real performance of the various devices should be expected to deviate from the simulated case, as the measured S-parameters are always acquired during optimal conditions.

5.9 Noise Figure Calculations

Using equations (2.75) and (2.76) the noise generated internally on the front-end can be calculated. As the microstrip lines are seen to have a very small influence on the noise figure, their contribution is only included for the stages up until the first LNA. Component noise characteristic can be temperature dependent, and will likely vary over time. Thus, two calculations are made, one for typical values of noise figure and gain, and one for maximum noise figure and gain, as listed in data sheets. Contribution from microstrip lines are disregarded in both cases.

Component	NF (dB)	T_e (K)	(G)
Capacitor	0.04	2.7	0.991
Switch	1.20	92.3	0.758
LNA	1.20	92.3	79.4
LP-filter	1.03	77.6	0.789
HP-filter	0.94	70.0	0.805
Circulator	0.26	17.9	0.942
System	1.89	256.7	

Table 5.1: Estimated noise figure and equivalent noise temperature (Typical Case)

Component	NF (dB)	T_e (K)	G
Capacitor	0.04	2.7	0.991
Switch	1.50	119.6	0.708
LNA	1.60	129.2	39.8
LP-filter	1.03	77.6	0.789
HP-filter	0.94	70.0	0.805
Circulator	0.5	35.4	0.891
System	2.35	392.1	

Table 5.2: Estimated noise figure and equivalent noise temperature (Worst Case)

Not all components are listed with more than one value for noise figure or gain. Table 5.1 displays the typical values for components and table 5.2 display maximum values for those where this could be obtained. For the typical case a noise temperature of 256.8 K with a corresponding noise figure of 1.89 dB is estimated. In the worst case, estimated values are 392.1 K and 2.35 dB.

5.10 Estimated Radiometric Sensitivity

An estimate of the radiometric sensitivity can be found by using the values of bandwidth and noise figure as found by simulation. Using the equation,

$$\Delta T = 2\frac{(T_A + T_{sys})}{\sqrt{B\tau}}, \tag{5.3}$$

where the bandwidth B has been found as 719 MHz and the integration time constant was calculated as $\tau = 0.0701$ s (4.7). Thus, by using the values for equivalent noise figure as found in tables 5.1 and 5.2, and assuming an antenna temperature of 310 K, the radiometer sensitivity is estimated as,

$$\Delta T_{best} = 0.16^oC, \tag{5.4}$$
$$\Delta T_{worst} = 0.2^oC. \tag{5.5}$$

As seen, the requirement of a sensitivity less than 0.1 ^{o}C is not met at hardware level of the radiometer. It is however possible to post-process the measured data at software level to achieve longer integration times and consequently increased sensitivity. For example, increasing the acquisition time to a more relevant value ($\tau = 2$ s) yields a radiometric temperature resolution of

$$\Delta T_{best} = 0.029^oC, \tag{5.6}$$
$$\Delta T_{worst} = 0.037^oC. \tag{5.7}$$

Chapter 6

Experimental Methodology

The chapter outlines the various experimental methods used to verify the performance of the radiometric system.

6.1 Test equipment

- Spectrum Analyzer – Anritsu MS2721B.
- Multimeter – Agilent 34401A.
- Signal Generator – HP 83752B.
- Network Analyzer – HP 8719D.
- Power Generator – Powerbox 3000 A.

6.2 Front-End

This section summarizes the various measurement techniques used to specifically characterize and verify the performance of the front-end receiver. The two most critical characteristics of the receiver is its noise figure, and verification that it is indeed stable.

6.2.1 S-parameters

- Network Analyzer – HP 8719D.
- Power Generator – Powerbox 3000 A.

The concept of S-parameters was described in section 2.1.3. Measurement of the front-end S-parameters gives a correct evaluation of the actual gain of the system (S_{21}), how well matched the input (S_{11}) and output (S_{22}) ports are, and the isolation (S_{12}). The most crucial parameter is the gain, from which the expected input power to the detector can be derived. System stability can be evaluated by measurements of the S-parameters as measured values can be used to compute the stability parameters.

Measurement Setup

The measurement setup involves the DUT[1], here the radiometer front-end, and the network analyzer. Port 1 of the analyzer is connected to the antenna input of the front-end, and port 2 to the output. The Dicke-switch is fixed with a constant control signal such that the antenna input is allowed to be transmitted through the entire system.

Before connecting the DUT, the network analyzer must be configured. The following settings are used:

- Center frequency = 3.5 GHz.
- Frequency span = 1 – 6 GHz.
- Port 1 power = - 45dBm.
- Port 2 power = - 25dBm.
- Measurement points = 401.
- IF bandwidth = 30 Hz.

The IF bandwidth sets the size of an internal noise filter in the network analyzer. A smaller integration bandwidth results in lowering the noise floor of the instrument. The power levels are chosen such that any internal noise of the front-end and from the reference source will be negligible. Port 2 delivers a higher power level because of the high isolation in the reverse direction, this prevents S_{12} from being obscured by internal noise (lost in the noise floor).

[1]Device Under Test

Error-Correction

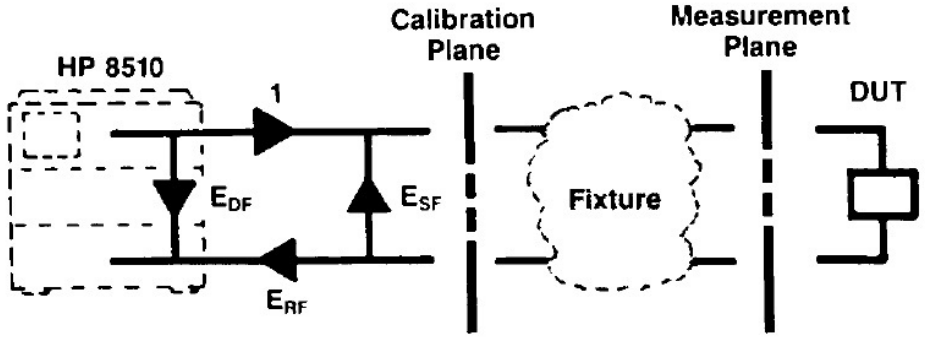

Figure 6.1: Illustration of complete measurement setup. The network pre calibration plane represents the connecting cables. The fixture represents any external components between the cables and the DUT pre error-correction. [16]

An important aspect of S-parameter measurements with network analyzers, is calibration to ensure that the S-parameters have the right plane of reference. Ideally, the S-parameters should be referenced to the input and output ports of the device under test (DUT), in which case it is said to be de-embedded. Normally, the network analyzer will be calibrated at the data collection plane, which is at the ports of the analyzer. Here the use of coax cables and transition fixtures is necessary to connect the front-end. To ensure that measurement errors are minimized, a full 2-port calibration (open-short-load-thru method) is conducted. This calibration compensates for all types of avoidable measurement errors. The error-correction procedure will also ensure that the end of the cable, including added fixtures, effectively becomes the data collection plane [16], such that the DUT is de-embedded.

The calibration must be conducted using the entire setup that will be used to connect the DUT, and with a standardized calibration kit. The network analyzer was calibrated with a HP 850520 3.5mm Economy Calibration Kit.

6.2.2 Assessing Stability

From design considerations and simulated results both, it is expected that instability of the amplifier cascade is not an issue. To assess the stability of the front-end, the measured S-parameters are used to compute the μ-factor

(2.48). If $\mu > 1$ for all measured frequencies, and the magnitude of S_{11} and $S_{22} < 1$, front-end stability has been established.

6.2.3 Noise Factor and Equivalent Noise Temperature

- Spectrum Analyzer – Anritsu MS2721B
- Variable Attenuator – HP 8494A

The noise generated by the front-end of the radiometer is a key factor in determining system performance. From equation (3.24) it is observed that system noise, T_{sys}, adds to the measured signal which the radiometer wants to detect and degrades the radiometric sensitivity. The magnitude of internally generated noise can be measured using the Y-factor method as described in section 2.3.7.

To create a cold and hot noise source, a temperature controlled chamber which can keep a stable temperature between -55 to 200^{o}C, is used. A broad banded 50Ω termination (resistive load) can then be used as a noise source. In this study, a termination of type 6506.19A delivered by Huber+Suhner is used. From the numerical analysis, an equivalent noise temperature between 256K and 389K is expected. Thus, for optimal noise figure measurements, the termination is heated to a temperature of 380K to act as a hot source, and cooled to 235K to act as a cold source.

The measured difference between the hot and cold source is expected to be very small. To ensure that error due to transmission loss between source, front-end and spectrum analyzer is minimized, high quality coax cables are be used to connect the devices. These cables have insertion loss of approximately 0.2 dB across a broad range of frequencies.

Measurement Settings

Spectrum analyzer settings:

- RBW = 1Hz.
- VBW = 1Hz.
- Center Frequency = 3.5 GHz.
- Span = 300 Hz.

- Averaging = 120 traces.

With RBW at 1 Hz, output power is given as dBm/Hz units and the noise floor of the device is lowered to a minimum. VBW is the video bandwidth which acts to filter fluctuation of the trace itself. 1 Hz is the smallest filter setting possible such that fluctuations due to noise is minimized. As very low power noise sources are used, the internal variation of the spectrum analyzer will exceed the difference in values that are expected between the hot and cold source. Using the internal averaging option will reduce these fluctuation and enable the difference to be detected.

6.3 Full System

This section explains the various measurements conducted to characterize the complete radiometer system. The radiometric system as a whole is mainly characterize by the linearity of its response to input power, temperature resolution and temperature stability, or drift. During these measurements the RF-related devices, front-end receiver and detector, are mounted in a steel box (as explained in section 4.4) to minimize interference. The LF/Dicke-circuit is not as sensitive to interference and is left outside for more convenient probing and accessibility.

For all following measurements, the output voltage of the radiometer is read by a digital multimeter (Agilent 34401A). The multimeter communicates with a computer through a GPIB to USB-bus. LabVIEW is then configured to sample data at a rate such that aliasing is avoided. The required sampling rate is decided by the hardware integration bandwidth which was found in section 4.3.2 to be 14.3Hz. Thus, by the Nyquist sampling theorem, if the output voltage is sampled with a frequency of at least 30 Hz, aliasing is avoided and the original signal can be recreated. The sampled data is stored in a text-file which is subsequently exported to MatLab for further processing.

6.3.1 Radiometer Temperature Response

The linearity of the radiometer temperature response can be found by measuring the output voltage when a source of a known temperature is used as an input. This will produce an output curve which relates the output voltage of the radiometer to a known temperature. Consequently, these measurement

can be used to obtain a calibration equation to transform measured voltages into absolute brightness temperature for later experiments.

A setup which should be easy to reproduce is constructed. The termination which was earlier used for noise measurements is here used to act as a noise source by submerging it into a thermostatic water bath. The water bath provides an easy way to set and measure the temperature of the noise source. Since the termination is a resistive load, it effectively allows the radiometer to measure the physical temperature of the water. Equivalently, it emulates an ideal antenna with perfect coupling to the medium under observation.

A medical microwave radiometer can be expected to measure temperatures in a range of approximately 20 ^oC to 40 ^oC. Thus, the measurements are conducted as follows. The thermostatic water bath is used to set the temperature to 20 ^oC, and 1000 samples of the output voltage is read. This procedure is repeated in 1 ^oC increments, up to 40 ^oC. All samples are averaged for each temperature to give a single data point which is then plotted such that a slope with a gradient in units of mV/^oC is generated. The gradient of the slope will then give an estimate of the radiometers sensitivity in terms of output millivolts versus input in temperature.

6.3.2 Identifying the Dicke Balance Point

In theory, the measured output voltage should be 0 for a balanced Dicke-radiometer. For an ideal radiometer, this would be when $\mathrm{T}_{ref} = \mathrm{T}_{antenna}$ (see section 3.2.5). In practice, due to an inevitable difference in the signal path gain this balance point will be offset. In this system, the antenna signal is attenuated more than the reference source. Thus, the apparent temperature of the antenna will be less than its physical temperature. The temperature the antenna physically must hold for the output voltage to be zero can be found by extrapolation of the measured linear temperature response.

6.3.3 Step Response and Integration Constant

The radiometer hardware is designed with a low integration time constant. (In section 4.3.2 the time constant was found to be 0.0701s.) An experimental verification of the time constant can be conducted by configuring LabVIEW to sample the output voltage at a high rate. A step response is emulated by initially leaving the antenna port open and during the measurement, rapidly connecting the matched termination.

The time constant of a system is defined as the time the systems step response takes to reach 63.2% of its asymptotic value. Thus, it is found by evaluating the difference between the voltage amplitudes before and after the step reponse and identifying the 63.2% amplitude. If V_1 is defined as the pre-step voltage and V_2 is defined as the asymptotic value of the step response, the voltage V at which the step response has reached 63.2% is then found as

$$V = V_1 + 0.632(V_2 - V_1). \tag{6.1}$$

If the time at which the step response begins is defined as t_1 and the time at which the step has reached V is defined as t_2, the time constant $\tau = t_2$ - t_1.

6.3.4 System drift

It is expected that variations in ambient temperature and self-heating of the instrument will cause variations of the measured output due to drift. By applying Dicke-switching the drift is supposed to be minimized. In the case of a fixed reference temperature, the contributions of drift are minimized when there is a balance between reference temperature and measured antenna temperature such that the output voltage is 0. Drift measurements are therefore conducted using the matched resistive load as before, which is submerged in water kept at the temperature estimated as explained in section 6.3.2.

Before measurements are initiated, the radiometer is allowed to be powered up for a while to reach a stable working temperature. The output voltage is then sampled continuously for approximately one hour. This should provide a good estimate as to how much drift will contribute to error in the measured brightness temperature.

6.4 Antenna on a Hot Object Embedded in a Lossy Medium

The radiometer designed in this study is first and foremost intended for detection of breast cancer, but could be used in other medical applications where temperatures of subcutaneous tissue are of an interest. Therefore, an experimental setup is generated to verify the radiometers ability to detect

thermal gradients generated by a hot object embedded in a lossy medium. The lossy medium in this case is regular, ionized, tap-water.

The hot object is made out of a balloon filled with water (~ 80 cc). The form and size of the hot object approximates the ellipsoidal shape of an infants urine bladder, which is an area of application in which microwave radiometry for non-invasive thermometry is currently being investigated [1]. The water circulates to the balloon through a silicon tube which is connected to a peristaltic pump. The silicon tube is at one end connected to a hollow copper spiral, which is submerged in a second thermostatic water bath. This creates a mechanism to control the temperature of the hot object. An illustration of the experimental setup is displayed in figure 6.2.

A microwave printed circuit board, single-arm, ground-plane backed Archimedian spiral antenna is used, as it has a highly directional power pattern function and good matching properties. Microwave spiral antennas are a common antenna type in microwave thermography applications [30, 2]. The size of the object in this study is such that it will cover the entire main lobe of the antenna power pattern. For all measurements, the phantom medium (water) is kept at a constant temperature of 41.4^oC, such as to ensure that errors due to drift and antenna mismatch are minimized.

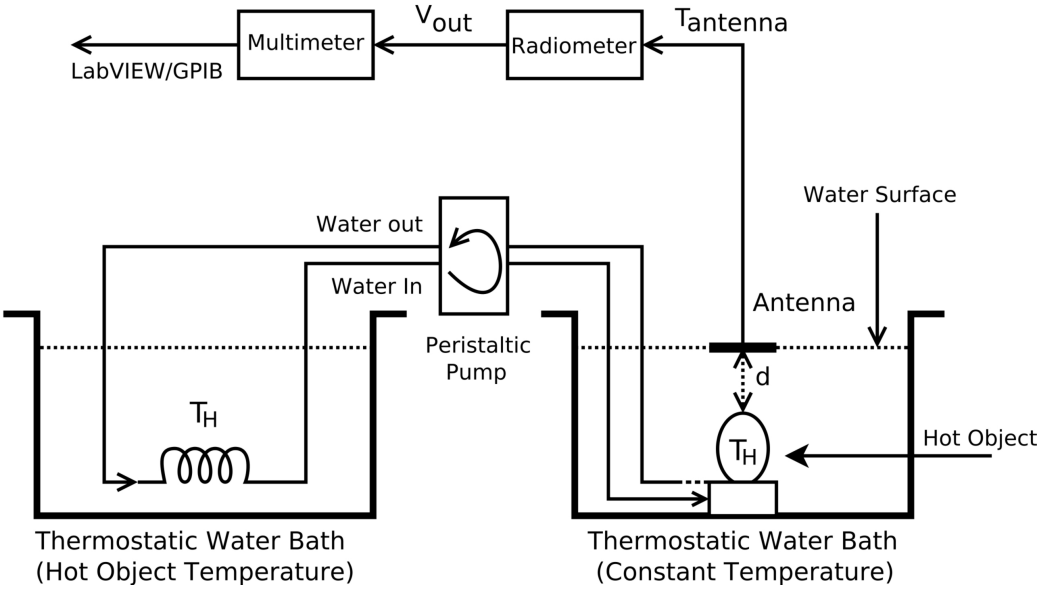

Figure 6.2: Illustration of experimental setup for measurements on a hot object in a lossy medium.

6.4.1 Measurements at 4 mm Depth

An initial measurement is conducted where the temperature of the object is varied over a large range. At t = 0, the object has a temperature of 21.1 ^{o}C. At t = 180 s and t = 240 s, the temperature is increased to 30 and 40 ^oC, respectively. As heating is not instantaneous, the measured output voltage is expected to gradually increase as temperature increases, before settling at a mean value between each temperature increase. For the initial measurement the object is placed at a distance of 4 mm below the surface of the water. The output voltage is sampled continuously such that the radiometer response can be seen over time. Using equation 7.1, measured output voltage is converted to a corresponding brightness temperature. Evaluating the increase ΔT_B in brightness temperature for the known increase in physical temperature a measure of the thermal response can be found.

A second measurement is conducted in which the temperature of the object is increased in 1 ^oC increments. The purpose is to see if the radiometer is able to differentiate such small temperature variations. In addition it should result in a comparable thermal response, if the same procedure of converting output voltage to brightness temperature is used. The output voltage is sampled 10000 times, such that ample data is available for post-processing. Each data point is generated by calculating the mean value of the measured brightness temperature and the temperature resolution is calculated for a time constant of 2 s by applying a running average filter on the raw data, and illustrated by error bars for each data point.

6.4.2 Measurements at Increased Depth

When the object is placed deeper below the surface of the water, the measured thermal response of the brightness temperature is expected to decrease, due increased attenuation of the microwave thermal radiation. Two experiments are conducted, first with the object placed at a depth of 8 mm then by increasing the depth to 10 mm. At 8 mm, three measurements are made where the temperature is increased in increments of 5 ^oC, beginning at 41.4 ^oC. The same procedure as described in the previous section is used to generate a plot of the measured brightness temperature.

At 10 mm, the same increments in temperature are used but a total of 7 measurements are conducted where the temperature of the hot object is increased, lowered and increased. Thus, a better picture of the repeatability and linearity of the radiometer can be obtained.

Chapter 7

Experimental Results

7.1 Front-End

7.1.1 S-Parameters

S-parameters of the front-end were measured as described in section 6.2.1. The results are presented in figures 7.1 and 7.2. It is seen that the maximum gain is measured to 43.5 dB. The 3 dB-bandwidth is defined from 3.13 GHz to 3.73 GHz, resulting in a measured bandwidth of 660 MHz.

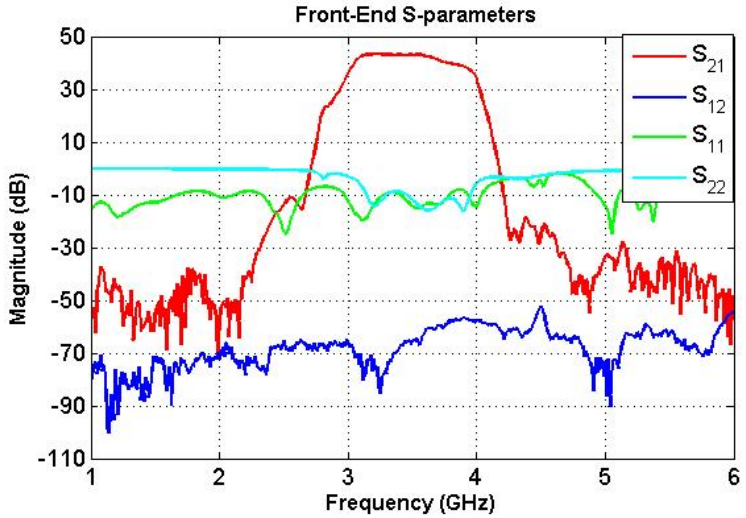

Figure 7.1: Measured S-parameters of the Front-End receiver.

Figure 7.2 gives a better view of the input and output matching properties of the system. It is seen that within the passband, return loss values are at an acceptable level. Outside the passband, especially S_{22} is seen to degrade sharply.

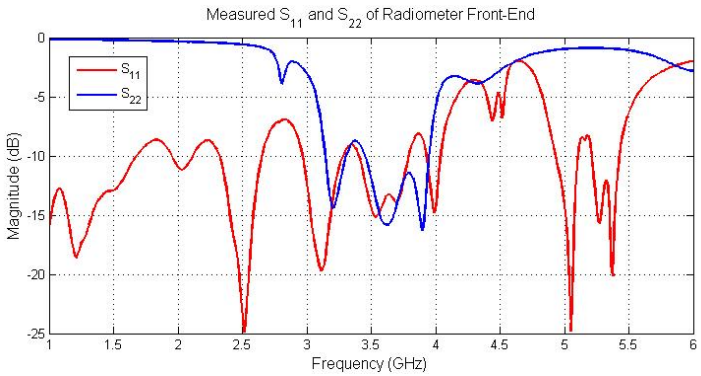

Figure 7.2: Measured S_{11} and S_{22} parameters of the Frond-End receiver.

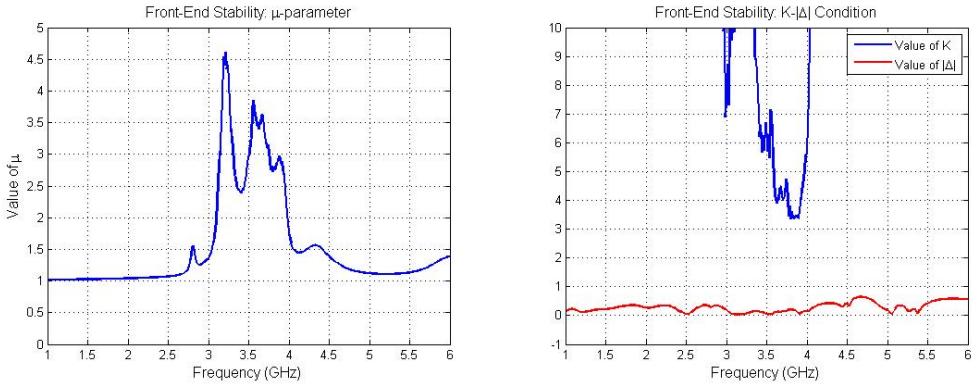

(a) μ-parameter as function of frequency (b) Rollet's condition as function of frequency

Figure 7.3: Stability calculations of radiometer front-end from measured S-parameters.

7.1.2 Stability

From figure 7.2 it is seen that S_{11} and S_{22} display acceptable values within the passband. Low values outside the passband could be a concern, especially with regards to S_{22}. Too high values could possibly indicate an issue of gain instability. To assess the stability of the front-end, the μ-parameter from

(2.48) is computed. For comparison, Rollet's K–$|\Delta|$ condition (2.46 and 2.47) is also calculated. The results are presented in figure 7.3a and 7.3b.

As both $|S_{11}| < 1$ and $|S_{22}| < 1$, both Rollets condition and the μ-test are seen to meet the specified demands for an unconditionally stable situation.

7.1.3 Noise Factor and Equivalent Noise Temperature

Table 7.1 displays the measured values of power and resulting estimates of noise temperature. All measured values are observed to lie within the range that is expected from numerical calculations; see section 5.9. The average value of system noise temperature is 301.7 K with a standard deviation of 22.4 K.

No.	P_{hot} (dBm)	P_{cold} (dBm)	Y	T_e (K)	F (dB)
1	-130.0304	-131.1149	1.2836	276.20	2.91
2	-130.1181	-131.1105	1.2567	329.79	3.30
3	-130.0970	-131.1394	1.2713	299.49	3.08
4	-130.0754	-131.0863	1.2621	318.24	3.22
5	-130.0592	-131.1277	1.2790	284.79	2.97

Table 7.1: Measured Noise Values of Front-End

7.2 Full Radiometric System

7.2.1 Step Response and Integration Constant

The time constant of the system can be found experimentally by the method described in section 6.3.3. Figure 7.4 displays the measured step response versus time.

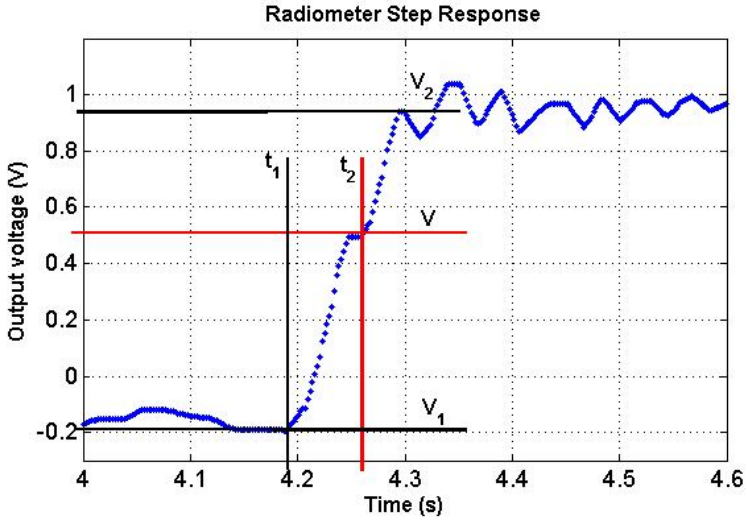

Figure 7.4: Measured step response of the radiometric system

By evaluation of the samples in figure 7.4, the voltage at which the step begins is defined as V_1 = -0.19 V at t_1 = 4.196 s, V_2 = 0.94 V. Thus V = 0.52 V, which is found at t_2 = 4.226 s. The time constant τ is then estimated to be $\approx$ 0.07 s, which is identical to the theoretical value calculated in (4.7). The hardware integration bandwidth $(1/\tau)$ is then 14 Hz. Thus, from the Nyquist sampling theorem, it is necessary to sample the radiometer output voltage at a rate of at least 28 Hz.

7.2.2 Temperature Response

This section introduces the results generated by the radiometer temperature response measurements as explained in section 6.3.1. In figure 7.5 the response is displayed in output voltage as a function of temperature. It is observed that the output displays a strictly linear trend within the measured

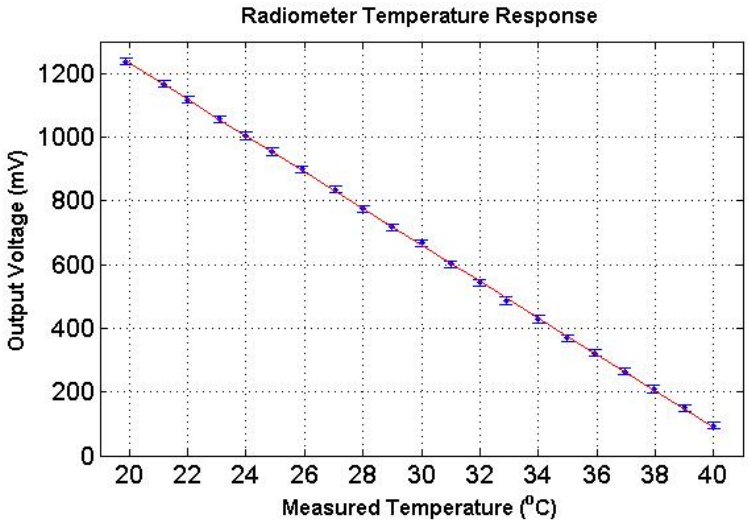

Figure 7.5: Radiometer temperature response (with error bars).

range of temperatures. The radiometer response is as expected, with decreasing output as the antenna temperature increases, which is due to the inverted linear response of the detector for increasing input powers. The sensitivity, α, is found as the gradient of a first-order polynomial trend line computed from the data points. Here, α = -57.2$mV/^oC$.

7.2.3 Radiometer Calibration

The temperature response data in figure 7.5 can be used for calibration of further measurements to obtain the absolute brightness temperature. The equation used for calibration used is

$$T_B = \frac{V_0 - V}{\alpha}, \tag{7.1}$$

where V_0 is the reference voltage in mV at T = 0 ^oC, V is the measured output voltage in mV and α is the sensitivity in mV/^oC. V_0 is found as 2377.3 mV by extrapolation of the polynomial trend curve (red line in figure 7.5).

7.2.4 Temperature Resolution

As a perfectly matched termination is used for calibration measurements, the measured temperature resolution of the radiometer can be found by calculating the standard deviation of the measured samples. The standard deviation is calculated for each measured temperature. This is presented as a histogram as seen in figure 7.6. The average temperature resolution is found to be ΔT = 0.192 ^oC for a time constant of 0.07 s. Comparatively, the estimated resolution from simulated results was between 0.16 ^oC and 0.2 ^oC.

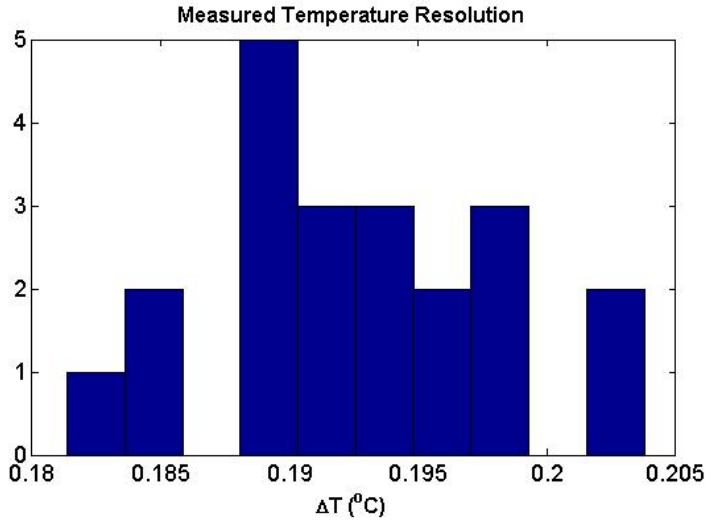

Figure 7.6: Distribution of measured radiometric sensitivity.

7.2.5 Radiometer Balance Point

The temperature at which the radiometer is balanced is found by the method described in section 6.3.2. Extrapolation of the polynomial trend line in figure 7.5 results in an estimate of T = 41.4 ^{o}C. Thus, when the antenna has a physical temperature of 41.4 ^{o}C, the Dicke-radiometer is balanced and the dependence of mismatch at the antenna interface and of gain variations are minimized (3.24).

7.2.6 System Drift

This section presents the results of the drift measurements as explained in section 6.3.4. In figure 7.7 the measured data is presented in terms of tem-

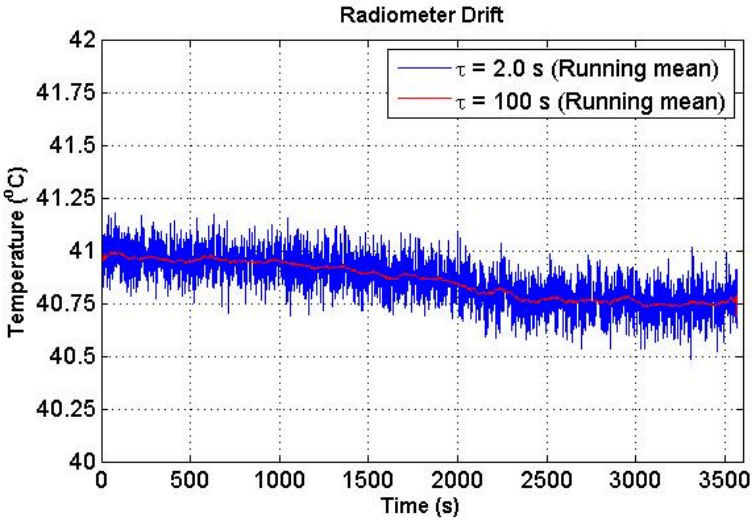

Figure 7.7: Radiometer drift measured in a 1 hour interval.

perature, which is obtained by using the calibration equation (7.1) found in section 7.2.3. The sampled data has been averaged by a running mean filter to smooth the largest variation. The blue line represents an integration time constant of 2 s. To visualize any trends, the superimposed red line has been averaged such that the integration time constant is 100 s.

The measurement was conducted using the matched termination submerged in water at a temperature of 41.4 ^{o}C, which is the estimated temperature the antenna must have for the radiometer to be balanced. A drift of only 0.2 ^{o}C is observed, indicating that the Dicke-implementation is well functioning. The minuscule temperature drift could well be caused by variations of the water temperature, as the accuracy of the thermostatic water bath is accurate to approximately one tenth of a degree centigrade.

7.3 Antenna on a Hot Object Embedded in a Lossy Medium

7.3.1 Initial Measurement

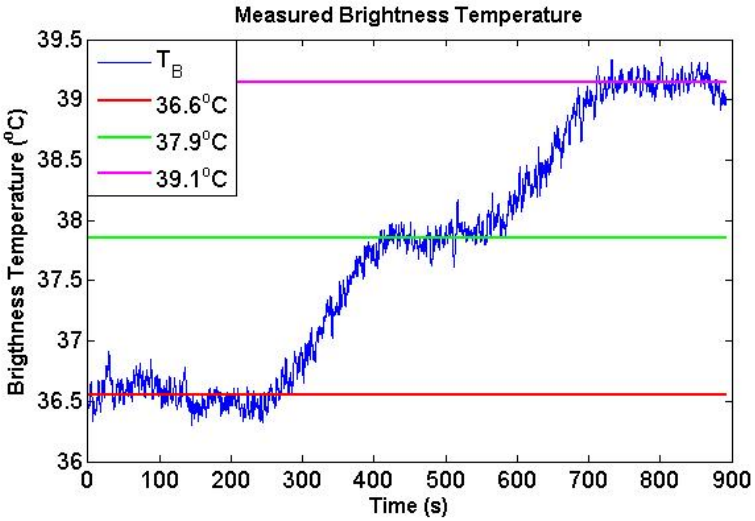

Figure 7.8: Measured brightness temperature with hot object positioned 4 mm below water surface. First 10 ^oC increment at t = 240 s, second 10 ^oC increment at t = 540 s. Medium temperature is 41.4 ^oC.

Figure 7.8 shows the measured and calibrated data of the first antenna measurement on a hot object. The data was sampled continuously such that the response to temperature over time could be evaluated. The measurements began with the hot object at a temperature of 21.1 ^{o}C, it was then increased abruptly up to 30 ^oC and finally to 40 ^oC. The object is submerged to a depth of 4mm below the surface of the water which is kept at a constant temperature of 41.4 ^oC

The horizontal lines in figure 7.8 display the computed average of the measured temperature within a time interval at which the temperature of the object has reached a stable value.

At a depth of 4 mm it is seen that an increase of 10 ^oC in the object, corresponds to a difference in measured brightness temperature of ≈ 0.13 ^oC per 1 ^{o}C. This relation ($\Delta T_B/\Delta T$) is hence termed *thermal response*, where ΔT here denotes the relative increase in temperature of the hot object.

7.3.2 Measurements at 4 mm Depth

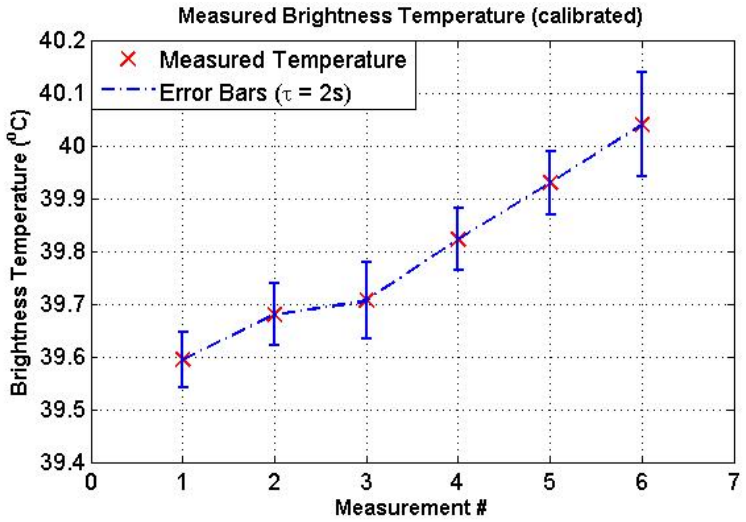

Figure 7.9: Measured brightness temperature with hot object positioned 4 mm below water surface. Object temperature at measurement no. : $1 = 41.4\ ^oC$, $2 = 42.4\ ^oC$, $3 = 43.4\ ^oC$, $4 = 44.4\ ^oC$, $5 = 45.4\ ^oC$, $6 = 46.4\ ^oC$. Medium temperature is $41.4\ ^oC$.

A repeated measurement on the hot object at a depth of 4 mm was conducted. Here, the temperature is increased in increments of $1\ ^oC$, beginning at $41.4\ ^oC$. From figure 7.9, it is observed that the absolute temperatures are not entirely linear. This could be caused by variations in the water bath temperature or spurious interference picked up by the antenna. Using the last 4 measurements, it is found that the measured thermal response is $\Delta T_B/\Delta T \approx 0.1\ ^oC/^oC$, which corresponds well with the estimation from the previous measurement. The error bars represents ΔT for $\tau = 2$ s.

7.3.3 Measurements at 8 mm Depth

Increasing the depth of the hot object should result in less sensitivity to the thermal gradient caused by the hot object, and consequently a smaller thermal response for the brightness temperature. The results depicted in figure 7.10 display the measured brightness temperature since the distance between the object and water surface is increased to 8mm.

The results show that the thermal response for the brightness temperature is now $\Delta T_B/\Delta T \approx 0.079\ ^oC/^oC$. The error bars represents ΔT for $\tau = 2$ s. As

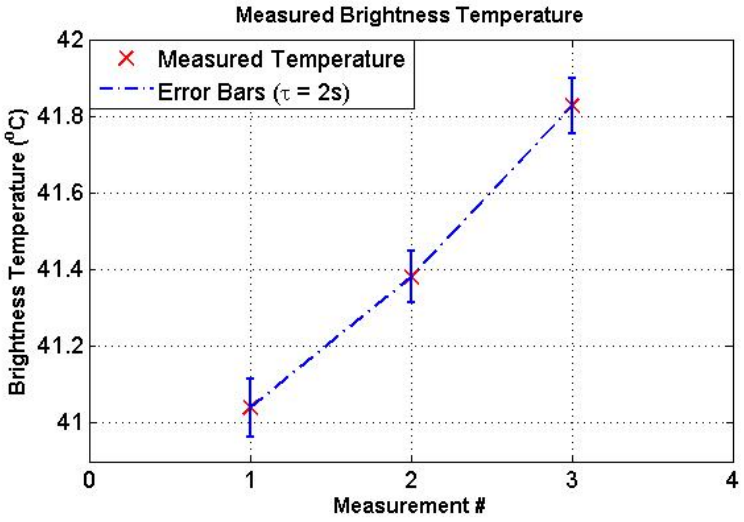

Figure 7.10: Measured brightness temperature with hot object positioned 8 mm below water surface. Object temperature for measurement: $1 = 41.4\ ^oC$, $2 = 46.4\ ^oC$, $3 = 51.4\ ^oC$. Medium temperature is $41.4\ ^oC$.

the thermal response has decreased, the results display an expected behavior.

7.3.4 Measurements at 10 mm Depth

A last test is conducted where the hot object is placed at a depth of 10 mm. Here, several measurements were made for comparison of repeatability and linearity of the instrument.

It is observed that the measured brightness temperature has increased with approximately $1\ ^oC$ as compared to the results of the previous section. Interference picked up by the antenna could be at fault. However, there is a good accordance with regards to the observed thermal response which has declined to $\Delta T_B/\Delta T \approx 0.072\ ^oC/^oC$. Figure 7.11 gives an adequate representation of the linearity of the measurement response and repeatability.

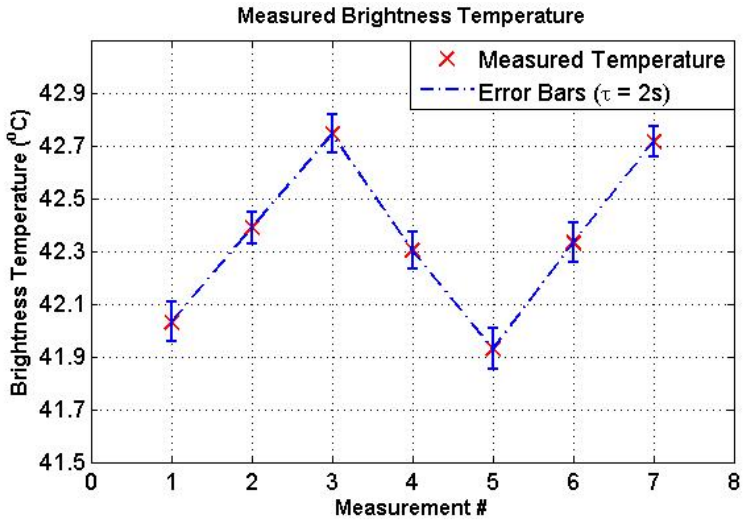

Figure 7.11: Measured brightness temperature with hot object positioned 10 mm below water surface. Object temperature for measurement: $1 = 41.4\,^oC$, $2 = 46.4\,^oC$, $3 = 51.4\,^oC$, $4 = 46.4\,^oC$, $5 = 41.4\,^oC$, $6 = 46.4\,^oC$, $7 = 51.4\,^oC$

Chapter 8

Discussion

A new miniaturized microwave radiometer for medical applications has been designed, implemented and experimentally verified through this study. The motivation for the work was to improve several aspects of an earlier implementation, in which issues with gain instability and an unacceptable noise figure, limited the applicability of the front-end [31]. As well as identifying and solving the core issues of the front-end, a new solution based on the switch-circulator Dicke-configuration was chosen, which further required the design of compatible post-detection (LF) hardware. This has been implemented as a separate device as it is deemed appropriate to keep RF and LF related components separated.

A range of tests conducted on, and with, the radiometer as a system and the receiver as an isolated device, have demonstrated a functioning radiometric system. The receiver provides stable and high amplification combined with a very low noise figure. Furthermore, linear response with regards to incident effect is found and good sensitivity is also obtained. The radiometer's ability to measure (brightness) temperature gradients on the order of 0.1 ^oC has been established through measurements on a hot object embedded in a lossy medium.

This discussion summarizes and comments on the various design approaches and choices which have resulted in a functioning system. Its performance is further discussed and compared against results of similar systems found in the literature. Lastly, some recommendations with regards to further development of the system are proposed.

8.1 Radiometric System

Front-End

The most important contributor towards the positive characteristics of the system is a functioning front-end receiver.

The front-end has been re-designed with focus on stability and reduced noise figure. In the previous realization of the front-end, oscillations where identified in the passband of the system. This was caused by instabilities in the amplifier cascade [31]. Through measurements of S-parameters and evaluation of the receiver stability, it has been demonstrated that the implementation of an isolator to de-couple the LNA cascade had the intended effect. Further measurements confirmed that the resulting receiver is able to provide sufficient gain such that the noise produced by sources of realistic temperatures ($\sim$300 K) can be reliably measured.

The implementation of an isolator represents a simple, yet clever, solution to the stability issue which allows the device to remain compact while at the same time preserving a low receiver noise figure, due to its high-quality transmission characteristics (insertion loss$<$ 0.5 dB).

Preserving a low noise figure is critical as it has a direct influence on the radiometric temperature resolution (3.25). Another factor which contributed towards conserving a low noise figure was the identification of a new DC-block capacitor with ultra low insertion loss ($<$ 0.04dB). Results from both simulation and noise figure measurements verify that the noise figure of the system is at an acceptable level. From numerical estimates the equivalent noise temperature of the front-end was expected to be in the range of 256 ^oC to 392 ^oC. This agrees well with the actual measured values which were found to be in the range of 276 ^oC to 329 ^oC.

Detector

In conjunction with a functioning front-end, a new active logarithmic detector is used. The detector's sensitivity is approximately 250 mV/μW, and thus provides superior sensitivity compared to regular passive square-law detectors which typically has a sensitivity of $\sim$0.5 mV/μW [60]. Measurements conducted on the full system demonstrates that despite using a logarithmic detector, the response of the radiometer is linear. This is possible as the

radiometer is only operated within a limited range of temperatures. A variation of 20 ^oC corresponds to less than 0.3 dB change with regards to the working point of the detector. Thus, as the detector is operated inside a very limited range as compared to its large dynamic range ($\sim$72 dB), its response is approximately following a square-law relation to the input power.

LF-circuit

The combination of a highly sensitive detector and a receiver with high gain puts less demands on the post-detection LF circuit which implements the Dicke-demodulation, such that design solutions are in some ways made simpler. This allows a relatively unorthodox but well functioning analogue solution for demodulation. The detector performance provides the possibility to use a simple solution to handle the bias in its output, using a polar electrolytic capacitor, which is important to achieve a symmetric signal (amplitude) swing across the amplifiers. The continuous amplification is also simplified with regards to controlling the stability of the operational amplifiers, since a low gain is needed.

A last important point to make about the LF-circuit is that it has been designed such that the signal paths are equal for both positions of the switch. Thus, any bias and error introduced by the operational amplifiers or the signal path in general, is handled at the demodulation stage, since there will be a symmetry with regards to added noise and bias. Consequently, the differential voltage at the output is as close to the real difference as possible with minimal error introduced.

Measurements of the step-response of the system confirms the performance of the LF-circuit with regards to integration. A time constant of 0.07 s was estimated and evaluation of the step-response provided confirmation as it was experimentally found to agree with the theoretical value. Using a short time constant at hardware level provides a simpler way to sample the output voltage. If the integration at hardware level is large, it will eventually result in filtering of the square wave which the output is generated. This results in problems when sampling, as one must know exactly when to trigger the samples such as to measure the correct voltage.

The short integration time results in a relatively poor sensitivity ($\approx 0.2\ ^oC$) compared to what is generally required for medical microwave radiometers. This is however not a concern, as it is readily handled at software level, as long as the output voltage is sampled at a sufficient rate. When an appro-

priate time constant is found, this is easily implemented in the hardware by replacing the series resistors in the demodulation circuit which currently have a resistive value of 0 Ω.

The purpose of implementing a Dicke-system is to minimize measurement error as a result of the temperature reliant gain variations of the receiver. Measurements conducted for a time span of an hour showed a maximum drift in absolute brightness temperature of approximately 0.2 ^oC, when the antenna input is kept at a temperature (41.4 ^oC) such that a balanced output ($V_{out} \approx 0$ V) is achieved. This represents a variation of only 0.48%. Which demonstrates a functioning Dicke implementation.

It should be mentioned that the measured drift may be a result of variations in the temperature of the thermostatic water bath. Since the water is kept at a relatively high temperature it will lose energy to the surroundings, such that the temperature might lower before the thermostat is able to control the temperature to its set value. There will also be some variations in the distribution of temperature in the water, which cannot be assumed to stay uniform at all times. A better estimation of the drift could have been made if a source of higher accuracy had been used.

It is important to note, however, that since a configuration with a single reference temperature is used, it must be assumed that if the antenna temperature deviates strongly from the point at which balance is achieved, error due to gain variations might become more significant. The use of a single reference temperature is a simple way to implement a Dicke-system, and one which will result in less accuracy than more advanced systems which implements null-balancing in some form.

8.2 Comparing Performance

It is natural to compare the improvement of the new front-end to that of the first prototype of which it is based. In the old design, a front-end sensitivity (including detector) of 745.9 mV/μW was achieved [31]. This result is of course with a reduced gain, as only two LNA where active on the front-end.

The front-end sensitivity for the radiometer developed in this study is found with a basis in the data presented in figure 7.5. The radiometer has a linear response of 57.2 mV/^oC. This is converted to mV/μW by equation (2.52), which gives that $1^oC \approx 9.1^{-9}\mu$W, for a pre-detection bandwidth of 660 MHz (see section 7.1.1). The radiometer sensitivity, including the LF-circuit, is

then $6.28{\cdot}10^9$ mV/μW. As the LF circuit provides a gain of 429, the sensitivity of the front-end can be estimated by normalizing with the LF-gain, which gives the result $1.49{\cdot}10^7$ mV/μW. This result demonstrates an improvement which is as large as 200000.

The most important performance parameter of the radiometer is the temperature resolution, which basically decides the minimum temperature gradients that can be reliably detected by the radiometer. Estimated temperature resolution for the hardware alone ($\tau = 0.07$ s) is approximately 0.2 ^oC. This is, however, not a very relevant acquisition time as most medical radiometers operates with a time constant in the range of 1 to 10 s. Thus, estimating for a time constant of 2 s, a temperature resolution of ≈ 0.04 ^oC is found.

Comparably, measurements conducted with the Archimedean spiral antenna results in a temperature resolution of ≈ 0.07 ^oC for $\tau = 2$s. As measurements with antennas will inevitably introduce some noise due to EMI, there is a good correspondence between the estimated and real value. It is also seen that the bandwidth estimated from simulations is larger then what is found from the measured S-parameters.

The temperature resolution is lower than the required 0.1 ^oC and is comparable with the standards of other medical microwave radiometers as reported in literature [29, 2]. If a longer acquisition time can be tolerated, it is possible to further increase the radiometric resolution. It can also be increased as discussed in section 8.4.

8.3 Hot Object Measurements

From the experiments with a hot object in a lossy medium, the radiometer's repeatability and performance as a sensor of subcutaneous temperatures was demonstrated. Using tap water as the phantom medium is a simplification of the real world challenge, as tissue is a heterogeneous medium. In another way, it also presents a good challenge as water is more lossy than fat, which is the primary tissue in breasts. The results are promising in that a strong correlation was seen between the temperature of the hot object and the measured brightness temperature.

The initial measurement demonstrated a linear and good thermal response when the object temperature was increased in increments of 10 ^oC. It was found that $\Delta T_B/\Delta T = 1.3$ $^oC/^oC$. This relation was confirmed by the second measurement. As the object temperature was increased by 1 ^oC increments,

a thermal response of $\Delta T_B/\Delta T \approx 0.1\ ^oC/^oC$ was found. It is also seen that for a time constant of 2 s, the sensitivity (width of error bars) is less than the relative increase in brightness temperature.

The last measurements demonstrated repeatability and coherent results, as well as the ability of the radiometer to detect smaller temperature gradients. As the object was submerged to a depth of 8 mm, the thermal response decreased to $\Delta T_B/\Delta T \approx 0.079\ ^oC/^oC$, and correspondingly for 10 mm it decreased to $\Delta T_B/\Delta T \approx 0.072\ ^oC/^oC$. In addition, for the last experiment several measurements for each temperature were conducted, demonstrating the radiometer's ability to accurately reproduce measurements over time.

It can be seen that for the last experiment (10 mm), the brightness temperature has increased by approximately 1^oC as compared to the experiment with the object at 8 mm. This could possibly be due to EMI picked up by the antenna, which will cause the measured brightness temperature to increase (3.13). Other reasons for the sudden increase could be that the antenna position is not exactly the same such that the antenna weighting function has been altered. Relatively, however, the measurement displays the same trends as before, with decreasing thermal response.

The experiments with a hot object is to some degree a simplification of the real problem. Mainly as the phantom (water) used is homogeneous, and no membrane is used to simulate skin effects. In addition, a highly directive antenna is used on a object which is relatively large. This simplifies matters as the antenna main lobe is so narrow that it will only "see" the object. Thus, if assuming a uniform temperature distribution in the hot object, a 1-D model can be approximated where the only variable is depth. The decreasing thermal response of the brightness temperature is therefore as expected, and the measurements show good concordance. For a more in depth explanation, it is referred to the mathematical model for thermal response which is derived in [29].

8.4 Proposals for Future Work

The system as it is today, demonstrates a functioning front-end receiver with a noise figure which is adequately low. The detector works as expected, resulting in a highly sensitive front-end, and errors due to drift and mismatch seem to be minimized through Dicke-switching. Further, the measurements on a hot object demonstrates that the radiometer has the ability to detect

temperature gradients as small as 0.1 ^oC.

Thus, on a hardware level, most of the remaining work should be focused on developing the LF-circuit. As of today, the LF-system is only implemented on a Veroboard. When a final design is worked out, it should be designed and implemented on a PCB. This will represent the last step towards a fully integrated radiometer, where all circuit boards are stacked and mounted in a compact steel enclosure for EMI shielding.

There are three main areas which could be enhanced in the circuit. Firstly, since a relatively low gain is needed, it is possible to use a single operational amplifier. This will lower the number of components in the circuit and consequently decrease its size. It is proposed to utilize a chopper-stabilized op amp for this purpose. Such a solution will minimize errors due to DC-offset, input current offset and temperature stability. Chopper-stabilized op-amps also minimize error due to flicker noise. In addition, such a solution provides a high impedance input, which is necessary to fully utilize the detector, and reduces the need of a buffer op-amp.

It should also be considered to implement a microcontroller as a part of the LF-system. The microcontroller can act as a "brain" for the radiometer, by generating and synchronizing all switch signals. In addition, it can be used as an A/D converter to sample the output voltage and implement signal processing such as averaging to obtain the necessary integration time constant. Implementing a microcontroller represents the last step towards a fully integrated system.

A/D converters usually have a dynamic range of 0 to 5 V. The current design is not optimized with regards to dynamic range, something which should be further looked into. Optimizing the system such that the full dynamic range is utilized will increase the temperature resolution of the system. The microcontroller can be placed as the last component of the LF-circuit, replacing the intermediate and output capacitor such that it read the voltage directly from the sample-and-hold capacitors.

Lastly, the circuit should be designed to be compatible with a higher Dicke-switcing rate. Currently, the system uses relatively large capacitors both in size and nominal value limiting the switching rate to 70 Hz. If the switching rate is increased, lower capacitor values can be used and consequently the size of these components can be reduced down to typical SMD size.

If the system is found to have acceptable performance characteristics, it could be interesting to look at the wireless solution for transfer of data which was explored in [31].

Chapter 9

Conclusion

This study has presented the design and implementation of a new, miniaturized microwave radiometer for medical applications. A previous version of the radiometer front-end has been successfully improved with regards to stability and noise figure, a more sensitive detector has been implemented and a new circuit for (Dicke) synchronous detection has been developed.

The radiometer has been verified to display good linearity, high sensitivity and negligible drift. Through experiments on a hot object embedded in a lossy medium, the radiometer's performance in detecting subcutaneous temperatures has been demonstrated. It was found that for a time constant of 2 s, a temperature resolution ΔT of 0.07^oC is achieved. Lastly, temperature gradients as small as 0.1 ^oC can be reliably and repeatedly detected.

Bibliography

[1] K. Arunachalam *et al.* Modeling the Detectability of Vesicoureteral Reflux Using Microwave Radiometry. *Physics in Medicine and Biology*, 55, 2010.

[2] K. Arunachalam *et al.* Characterization of a Digital Microwave Radiometry System for Noninvasive Thermometry using Temperature Controlled Homogeneous Test Load. *Physics in Medicine and Biology*, 53(14), 2008.

[3] A.H. Barrett, P.C. Myers, and N.L. Sadowsky. Microwave Thermography in the Detection of Breast Cancer. *American Journal of Roentgenology*, 134:365–368, February 1979.

[4] B. Bocquet *et al.* Microwave Radiometric Imaging at 3 GHz for the Exploration of Breast Tumors. *IEEE Transactions on Microwave Theory and Techniques*, 38(6), 1990.

[5] A.K. Buck, H. Schirrmeister, T. Mattfeldt, and S.N. Reske. Biological Characterization of Breast Cancer by Means of PET. *European Journal of Nuclear Medicine and Molecular Imaging*, 31, 2004.

[6] A. Camps and J.M. Tarongi. Microwave Radiometer Resolution Optimization Using Variable Observation Times. *Remote Sensing*, 2010.

[7] American Cancer Society Inc. How is Breast Cancer Staged. `http://www.cancer.org/Cancer/BreastCancer/DetailedGuide/breast-cancer-staging`, 2009.

[8] K.L. Carr. Microwave Radiometry: Its Importance to the Detection of Cancer. *IEEE Transactions on Microwave Theory and Techniques*, 37(12):1862–1868, 1989.

[9] K.L. Carr. Radiometric Sensing. *IEEE Potentials*, 16:21–25, Apr/May 1997.

[10] K.L. Carr *et al.* Radiometric Sensing: An Adjuvant to Mammography to Determine Breast Biopsy. *IEEE MTT-S Digest*, 2000.

[11] R.J. Collier and A.D. Skinner. *Microwave Measurements*. The Institution of Engineering and Technology, 3 edition, 2007.

[12] R.H. Dicke. The Measurement of Thermal Radiation at Microwave Frequencies. *Review of Scientific Instruments*, 17:268–275, 1946.

[13] L. Dubois *et al.* Temperature Control and Thermal Dosimetry by Microwave Radiometer in Hyperthermia. *IEEE Transactions on Microwave Theory and Techniques*, 44(10), 1996.

[14] L. Dubois *et al.* Temperature Measurement by Microwave Radiometry. *IEEE International Instrumentation and Measurement Technology Conference*, 2008.

[15] M.L. Edwards and J.H. Sinsky. A New Criterion for Linear 2-Port Stability Using a Single Geometrically Derived Parameter. *IEEE Transaction on Microwave Theory and Techniques*, 40(12), December 1992.

[16] G. Elmore. *De-Embedded Measurements Using The HP 8510 Microwave Network Analyzer*, 1985.

[17] J.G. Elmore *et al.* Ten-Year Risk of False Positive Screening Mammograms and Clinical Breast Examinations. *The New England Journal of Medicine*, 1998.

[18] B. Enander and G. Larson. Microwave Radiometric Measurements of the Temperature Inside a Body. *Electronic Letters*, 10(15):317–318, 1974.

[19] R. Fiore. Circuit Designer's Notebook: Capacitors in Coupling and DC Blocking Applications. `http://www.atceramics.com/pdf/technotes/capacitors_in_coupling.pdf`. Excerpt from complete Circuit Designers' Notebook.

[20] H.T. Friis. Noise Figures of Radio Receivers. *Proceedings of the IRE*, pages 419–422, July 1944.

[21] R. Gilmore and L. Besser. *Practical RF Circuit Design for Modern Wireless Systems, vol 2.* 2003.

[22] I. Gouzouasis *et al.* A Contactless Multi Frequency Brain Radiometric Imaging and Hyperthermia Treatment Aparatur the use of Dielectric Matching Materials in Phantom Experiments. *IEEE International Workshop on Imaging Systems and Techniques*, 2008.

[23] P.M. Gullino. Natural History of Breast Cancer – Progression From Hyperplasia to Neoplasia by Angiogenesis. *Cancer (Philadelphia)*, 39:2697–2703, 1977.

[24] D. Gur and L.P. Wallace *et al.* Trends in Recall, Biopsy, and Positive Biopsy Rates for Screening Mammography in an Academic Practice. *Radiology*, 235:396–401, 2005.

[25] A. Guyton and J. Hall. *Textbook of Medical Physiology.* W.B Saunders Company, 10 edition, 2000.

[26] World Health Organization Website. `http://www.who.int/cancer/detection/breastcancer/en/index1.html`.

[27] P.P. Hsu and D.M Sabatini. Cancer Cell Metabolism: Warburg and Beyond. *Cell*, 134:703–707, September 2008.

[28] Phan T. Huynh, Amanda M. Jarolimek, and Susanne Daye. The False-negative Mammogram. *RadioGraphics, The Journal of Continual Education in Radiology*, 1998.

[29] S. Jacobsen and Ø. Klemetsen. Improved Detectability in Medical Microwave Radio-Thermometers as Obtained by Active Antennas. *IEEE Transactions on Biomedical Engineering*, 55, 2005.

[30] S. Jacobsen, P.R. Stauffer, and H.O. Rolfsnes. Characteristics of Microstrip Muscle-Loaded Single-Arm Archimedean Spiral Antennas as Investigated by FDTD Numerical Computations. *IEEE Transactions On Biomedical Engineering*, 52, February 2005.

[31] Amund K. Johansen. Design, implementering og evaluering av et trådløst medisinsk radiometer basert på IEEE 802.15.4–standarden og Zigbee. Master's thesis, University of Tromsø, 2009.

[32] J. B. Johnson. Thermal Agitation of Electricity in Conductors. *The Physical Review*, 32:97–109, 1928.

[33] T. Kempka *et al.* Microwaves in Fire Detection. *Fire Safety Journal*, 41:419–422, April 2006.

[34] D.V. Land. An Efficient, Accurate and Robust Radiometer Configuration. *The Journal of Microwave Power and Electromagnetic Energy*, 36(3):139–144, 2001.

[35] D.V. Land. A Clinical Thermography System. *IEE Proceedings*, 134:193–200, February 1987.

[36] D.V. Land. Medical Microwave Radiometry and its Clinical Applications. *IEE Coloquium on Applications of Microwaves in Medicine*, 1995.

[37] D.V. Land *et al.* Microwave Thermography as a Noninvasive Assessment of Disease Activity in Inflammatory Arthritis. *Clinical Rheumatology*, 13:589–592, 1994.

[38] J. Lesurf. Sources of Noise: Johnson & Shot Noise. `http://www.st-andrews.ac.uk/~www_pa/Scots_Guide/iandm/part3/page1.html`.

[39] E. Lillesøl, O. Hunderi, and J.R. Lien. *Generell Fysikk for universiteter og høgskoler*, volume 2.

[40] K. Maruyama *et al.* Feasibility of Noninvasive Measurement of Deep Brain Temperature in Newborn Infants by Multifrequency Microwave Radiometry. *IEEE Transactions on Microwave Theory and Techniques*, 48(11), 2000.

[41] R. McCluney. *Introduction to Radiometry and Photometry.* Artech House Inc, 1994.

[42] S.K. Moore. Better Breast Cancer Detection. *IEEE Spectrum*, 2001.

[43] U.S. National Cancer Institute. `http://www.cancer.gov`.

[44] H. Nyquist. Thermal Agitation of Electric Charge in Conductors. *The Physical Review*, 32:110–113, 1928.

[45] Committee on Technologies for the Early Detection of Breast Cancer. Mammography and Beyond: Developing Technologies for the Early Detection of Breast Cancer, 2001.

[46] David M. Pozar. *Microwave Engineering 3. Edition.* John Wiley & Sons, Inc., Hoboken, NJ, 2005.

[47] U.S. Preventive Task Force. Screening for Breast Cancer: U.S. Preventive Services Task Force Recommendation Statement. *Ann Intern Med.*, 151:716–726, 2009.

[48] Website: Radiological Society of North America Inc. `http://www.radiologyinfo.org/`, 2010.

[49] Cancer Registry of Norway. Cancer in Norway 2008: Cancer Incidence, Mortality, Survival and Prevalence in Norway. `http://www.kreftregisteret.no/Global/Publikasjoner%20og%20rapporter/CiN2008part1_web.pdf`, 2010.

[50] P. Robbins. Using Noise For RF Receiver Built-In Test Applications. *Microwave Journal*, 2004.

[51] A. Sarvazyan and C.S. Kaufman *et al.* Cost-Effective Screening for Breast Cancer Worldwide: Current State and Future Directions. *Breast Cancer: Basic and Clinical Research*, pages 91–99, 2008.

[52] M.D. Schnall. Application of Magnetic Resonance Imaging to Early Detection of Breast Cancer. *Breast Cancer Res*, 3:17–21, 2001.

[53] A. Eugene Sharkov. *Passive Microwave Remote Sensing of The Earth.* Praxis Publishing Ltd, 2003.

[54] Agilent Technologies. Agilent EEsof EDA, Two-stage LNA for 5–6 GHz Applications using SiGe BFP640 Transistor. `http://ep.literature.agilent.com/litweb/pdf/5989-9308EN.pdf`.

[55] Agilent Technologies. Fundamentals of RF and Microwave Noise Figure Measurements. Application Note 57-1.

[56] Johnson *et al.* Through-Wall Sensor With Multi–Frequency Microwave Radiometry: A Proof-of-Concept Demonstration. *IEEE Transactions on Geo–Science and Remote Sensing*, 47, May 2009.

[57] V. Thomy *et al.* Radiometric Sensor for Temperature Control of Food Processing. *IEEE Sensors Journal*, 4, December 2004.

[58] S.G. Vesnin *et al.* Role of Microwave Radiometry in Mammology. 2000. http://www.resltd.ru/eng/literature/.

[59] W. Zhang *et al.* A 1–4 GHz LNA for Convenient Cascade Application. *IEEE Xplore*, April 2007.

[60] Webpage: Microwaves 101. `http://www.microwaves101.com/`, 2010.

[61] DATASHEET HMC593LP3. `http://www.hittite.com/content/documents/data_sheet/hmc593lp3.pdf`.

[62] DATASHEET 3CDMG35-4. `http://dorado-intl.com/CatalogImages/File/Feature_Products/Dorado_SMTDatasheetR3.pdf`.

[63] DATASHEET ATC600S. `http://www.atceramics.com/pdf/600s(1).pdf`.

[64] DATASHEET CSWA2-DR+. `https://www.minicircuits.com/pdfs/CSWA2-63DR+.pdf`.

[65] DATASHEET HFCN-3400+.
http://www.minicircuits.com/pdfs/HFCN-3100+.pdf.

[66] DATASHEET HMC602LP4.
http://www.hittite.com/content/documents/data_sheet/hmc602lp4.pdf.

[67] DATASHEET LFCN-3400+.
http://www.minicircuits.com/pdfs/LFCN-3400+.pdf.

[68] DATASHEET LT1128.
http://cds.linear.com/docs/Datasheet/1028fa.pdf.

[69] DATASHEET LTC1043.
http://cds.linear.com/docs/Datasheet/1043fa.pdf.

[70] DATASHEET RO4350B.
http://www.rogerscorp.com/documents/726/acm/RO4000-Laminates---data-sheet-and-fabrication-guidelines-RO4003C-RO4350B.aspx.

Appendix A

Schematic And Board Design

A.1 Front-End

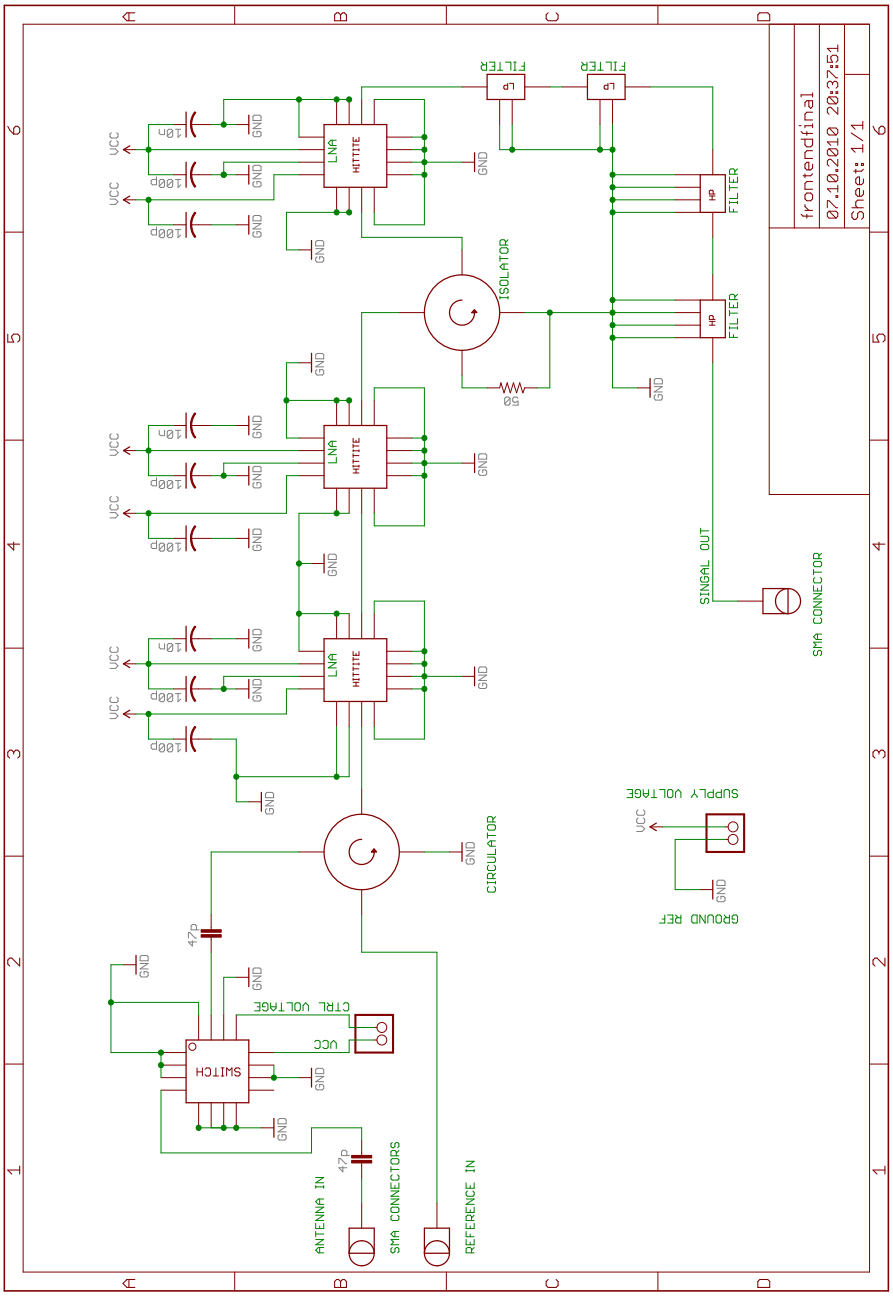

Figure A.1: Electrical Schematic for Radiometer Front-End

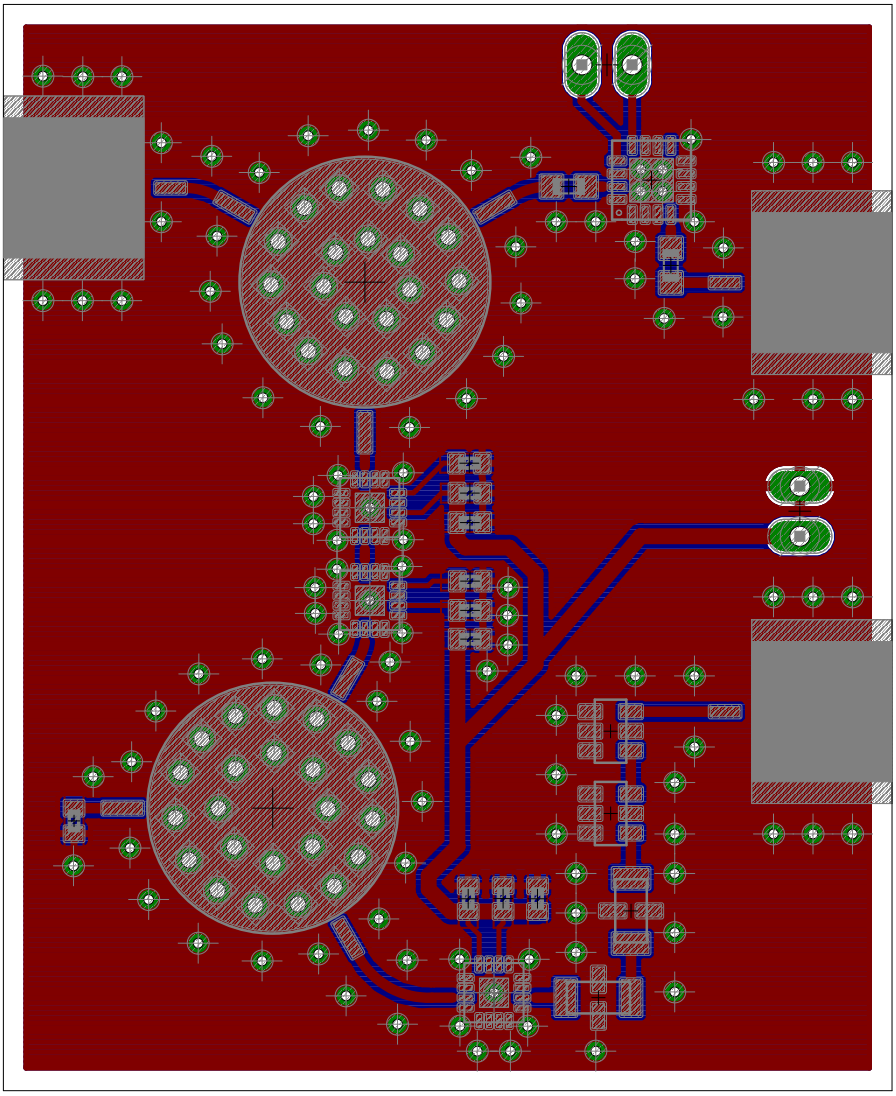

Figure A.2: Radiometer printed circuit board layout

Appendix B

List of Figures

List of Figures

Appendix C

List of Tables

List of Tables